# An Investigation of Cermet and Composite HVOF Thermal Spray Coatings for Internal Surfaces

Jamie Pulsford

Thesis submitted to the University of Nottingham

for the degree of Doctor of Engineering (EngD)

March 2020

# Abstract

High velocity oxy-fuel (HVOF) thermal spraying is a surface engineering technique which can be used to deposit coatings to provide protection from wear or corrosion. Powder particles are accelerated using a spray torch and are fired towards the required surface. WC-Co-Cr is a commonly used material that is deposited using this technique to act as a wear resistant barrier. The use of composite WC-Co/NiCrFeSiB coatings has also been a topic of interest for applications that require resistance to wear at high temperatures.

In recent years, manufacturers have sought to develop thermal spray processes for internal surfaces, and this was followed by the development of internal diameter (ID) HVOF thermal spray torches that have smaller dimensions than the previously commercially used spray systems. This allowed the deposition of HVOF thermal spray coatings onto surfaces which were previously considered impossible to coat in this manner. Little is currently known regarding the effects of spraying in these conditions due to the recent development of the new ID spray systems.

In this EngD thesis, three types of WC-Co-Cr powder feedstock differing in WC grain size and overall particle size were sprayed with an ID-HVOF thermal spray torch. Detailed microstructural characterisation of the sprayed coatings followed by the measurement of coating mechanical properties and dry sliding wear testing at three loads was performed. It was determined that using a powder feedstock that is smaller in size

produced coatings with a high microhardness but led to greater decarburisation of the WC phase reducing the fracture toughness. This was because the smaller particles require less energy for heating and acceleration, leading to higher in-flight temperatures and velocities. The coatings sprayed using the smaller particle feedstock however performed to a good relative standard in the dry sliding wear testing, leading to it being selected for internal spray experiments.

The selected WC-Co-Cr powder was then sprayed onto discs mounted on the inside of three cylindrical tubes with different internal diameters of 70mm, 90mm and 110mm. Spraying within the smallest diameter tube produced coatings with the lowest microhardness and highest porosity. This was likely due to particles being unable to accelerate sufficiently when spraying within the smallest tube due to the reduced stand-off distance. Brittle η-phase carbides were found within all three internally sprayed coatings possibly formed by substrate overheating due to the increased challenges of substrate cooling processes in ID-HVOF thermal spraying.

To investigate the effects of spraying a composite powder feedstock, a WC-Co/NiCrFeSiB feedstock was sprayed using the ID-HVOF torch using two different spray parameter sets. Detailed microstructural characterisation and measurement of mechanical properties revealed that increasing the overall gas flowrate produced coatings with a higher microhardness which also exhibited better sliding wear resistance. This is due to greater in-flight velocities observed with the increase in flowrate.

# Publications

- J. Pulsford, S. Kamnis, J. Murray, M. Bai, T. Hussain, *Effect of particle and carbide grain sizes on a HVOAF WC-Co-Cr coating for the future application on internal surfaces: microstructure and wear*. Journal of Thermal Spray Technology, 27 (2018), 207-219
- J. Pulsford, F. Venturi, Z. Pala, S. Kamnis, T. Hussain, *Application of HVOF WC-Co-Cr coatings on the internal surface of small cylinders: Effect of internal diameter on the wear resistance*, Wear. 432–433 (2019) 202965.
- J. Pulsford, F. Venturi, S. Kamnis, T. Hussain, *Sliding wear behaviour of WC-Co reinforced NiCrFeSiB HVOAF thermal spray coatings against WC-Co and $Al_2O_3$ counterbodies*. Surface and Coatings Technology. 386 (2020) 125468

## Conferences

- J. Pulsford, M.Bai, T. Hussain, *Suspension High velocity oxy-fuel (SHVOF) thermal spraying of $Cr_2O_3$ and $Cr_2O_3$ with graphene platelets for dry sliding wear protection***.** Conference paper: International Thermal Spray Conference 2018 (Orlando, FL, USA)
- J. Pulsford, S. Kamnis, J. Murray, M. Bai, T. Hussain, *Effect of particle and carbide grain sizes on a HVOAF WC-Co-Cr coating for the future application on internal surfaces: microstructure and wear*. Conference paper: International Thermal Spray Conference 2017 (Dusseldorf, Germany) – **Best paper award winner ITSC 2017**

# Acknowledgements

I would like to express my gratitude towards my supervisors Dr. Tanvir Hussain, Dr. Federico Venturi and Dr Mingwen Bai for their guidance, support and patience throughout the course of this project. I would also like to thank my industrial supervisor Dr Spyros Kamnis for providing me help and knowledge direct from the thermal spray industry.

Furthermore, I'd like to give thanks to all my family and friends, who offered support and encouragement throughout the entire length of this project. It would not have been possible without all your support.

This project was sponsored by Castolin-Eutectic Monitor Coatings Ltd, North Shields, UK and I would like to thank them for making this project a reality.

# Table of Contents

# Chapter 1. Introduction

High velocity oxy-fuel (HVOF) thermal spraying is a widely used method to apply wear resistant coatings on parts used in a variety of industries, such as the aerospace, steel, energy, and chemical/process industries. HVOF thermal spraying involves the spraying of particles typically in the size range of 5 – 45μm, by feeding them into a spray torch alongside a fuel and oxidiser source, which are then ignited with the heated powders being expelled from the torch carried by gases now moving at supersonic speeds.

There has been a growing interest in the application of HVOF thermal spray coatings for surfaces such as the inside of parts such as cylindrical pipes, billet moulds and ball valves, known as internal diameter (ID-HVOF) thermal spray. Potential applications include the deposition of wear resistant coatings such as WC-Co-Cr for the protection of the internal surface of billet moulds used in the steel industry to prolong their service life, or WC-Co/NiCrFeSiB composite coatings to provide high temperature corrosion and wear resistance for the internal surfaces of process piping.

However, the application of coatings on the internal surfaces of such parts has many associated challenges. HVOF thermal spraying is a line of sight process with the spray torch physically needing to be pointing at the target substrate to apply a coating, meaning the variety of applications of this technique is limited by the physical dimensions of the torch itself. To apply a coating on the inner surface of a part such as the housing of a ball valve or a cylindrical pipe of hydraulic cylinders and landing gears, known as an

internal surface, the torch would need to fit inside the part to be sprayed to coat the surfaces inside. Furthermore, a certain distance is required between the HVOF torch nozzle exit and the part to be coated to allow time for the particles to accelerate to the required high velocities, known as the stand-off distance. When applying coatings on parts with smaller internal diameters, this stand-off distance could be as low as 30mm compared to the typical stand-off distances of around 300mm needed in traditional HVOF thermal spray processes, meaning there is a shorter distance available for particles to accelerate to the high velocities required to produce good coatings.

To meet the demands of ID-HVOF thermal spray, manufacturers have begun to develop a variety of thermal spray systems that possess much smaller dimensions and can spray coatings at shorter stand-off distances than the older, previously used thermal spray torches. These smaller torches can more readily fit inside a greater range of parts to apply coatings and can spray coatings at shorter stand-off distances in comparison to their predecessors. As the in-flight particle and therefore coating properties are a function of the gun design and spray parameters used, it is currently unclear on how coatings sprayed by these new smaller HVOF thermal spray torches compare to those sprayed by the older, larger spray systems.

ID-HVOF is still an emerging field for research and industrial interest, meaning there has been little work published regarding the spraying and characterisation of HVOF coatings sprayed on internal surfaces [1]. Little is

currently known regarding spraying onto internal surfaces and with the differences in stand-off distance and increased difficulties with substrate cooling, it is likely coatings may differ when sprayed internally.

WC based cermets such as WC-Co and WC-Co-Cr are commonly used wear resistant materials that can be sprayed by HVOF thermal spraying to produce coatings with high hardness, providing a good wear resistant barrier. To compensate for the shorter stand-off distance and reduced dimensions of ID-HVOF spray torches, it has been theorised that finer particle feedstocks should be used as smaller, lighter particles require less energy for melting and acceleration. Furthermore when spraying a WC cermet powder, reducing the WC grain size of the powder is another possible route to improve coating properties to compensate for the challenges of ID-HVOF thermal spray, as these powder feedstocks have been said to produce harder coatings compared to those sprayed with larger WC grained powders [2]. It is currently unclear how these changes will affect the coating microstructure, mechanical properties and sliding wear resistance of the coatings when spraying using an ID-HVOF thermal spray system.

NiCrFeSiB self-fluxing alloys are emerging as another potentially useful coating material for internal surfaces, due to the material's high resistance to corrosion and wear at elevated temperatures. To compensate for the low hardness of the material, it is often mixed with a reinforcing hard phase material, such as WC-Co. Spraying a composite powder feedstock creates

new challenges, with different materials likely having separate properties in-flight due to different material properties and particle morphologies. As a result, optimisation of the spray process may be more challenging, and these issues may be amplified at the shorter stand-off distances used in potential ID-HVOF applications.

## 1.1 Aims and Objectives

The main aim of this work is to assess the viability of future ID-HVOF processes for the application of cermet coatings for sliding wear resistance applications. The literature review uncovered gaps in the current knowledge in several key areas regarding ID thermal spray processes in general. To address these gaps in the literature, the following work should be carried out.

- WC-Co-Cr powder feedstocks with different particle size ranges and WC grain sizes should be sprayed using an ID-HVOF thermal spray torch to assess which type of powder feedstock provides the best performing coatings for a potential ID-HVOF application. This would be achieved by detailed characterisation of the coatings, followed by the measurement of mechanical properties, and sliding wear rates at different loads.
- To address the lack of knowledge regarding ID-HVOF thermal spray coatings, the best performing powder feedstock from the previous study should be applied on the internal surface of cylindrical parts with differing internal diameters. These coatings should then be

characterised in a similar manner as above, with sliding wear testing used as a performance tool. This would provide insight into the effect of spraying internal coatings, alongside giving knowledge into the effect of stand-off distance and part size when spraying in these conditions.

- Coatings of WC-Co/NiCrFeSiB should be sprayed using an ID-HVOF spray torch either onto samples mounted internally, or at a short stand-off distance to simulate internal spray. A detailed microstructural characterisation, alongside the measurement of mechanical properties and sliding wear testing should be performed. To investigate the effects of spray parameters on the coating microstructure, porosity and sliding wear resistance, the composite powder feedstock should be sprayed using different parameter sets.

## 1.2 Scope of the thesis

This thesis contains 7 chapters, and a brief overview of each chapter is presented below:

Chapter 2 presents a literature review divided into 6 main sections. The first section presents an overview of wear mechanisms likely observed when studying the wear of thermal spray coatings. This is followed by an overview of surface engineering and thermal spraying in general. HVOF thermal spraying is covered in the third section, with the work carried out in aspects of the topic relevant to ID-HVOF thermal spraying covered, including effects of stand-off distance, oxidation and microstructure. A

review of the current state of knowledge of ID-HVOF thermal spraying is presented next. Finally, sections summarising the current knowledge regarding HVOF coatings of WC-Co-Cr and WC-Co/NiCrFeSiB are provided.

Chapter 3 describes the experimental methods used throughout this thesis with some overview on the methodology used.

Chapter 4 presents a study on WC-Co-Cr powder selection for ID-HVOF thermal spraying. WC-Co-Cr powders differing in particle size range and WC grain size were sprayed using an ID-HVOF thermal spray torch. The powder feedstocks and coatings were characterised, followed by the measurement of the coating's mechanical properties and resistance to sliding wear at three separate loads.

Chapter 5 presents a study in which the WC-Co-Cr powder feedstock selected from the previous chapter was sprayed onto substrates mounted internally within cylindrical tubes with three different internal diameters using the same ID-HVOF thermal spray torch. The effect of the change of internal diameter on the coating microstructure, mechanical properties and resistance to sliding wear was investigated.

Chapter 6 presents an experimental study in which WC-Co/NiCrFeSiB composite coatings were sprayed using two different sets of spray parameters with the ID-HVOF thermal spray torch. The effect on the change of parameters on the coating microstructure, mechanical properties and wear resistance was studied.

Finally, the overall conclusions of this work, alongside recommendations for future work are outlined in Chapter 7.

# Chapter 2. Literature review

## 2.1 Wear

Wear can be described as the progressive loss of material from the surface of a body brought about by mechanical action. Wear is not a material property, but instead is a system response, with operating conditions affecting the wear process. Wear is often seen as being a primary culprit in the failure of many engineering components, leading to them needing to be replaced. In these instances, the particular product is likely to degrade slowly, rather than suffer a traumatic breakage [3]. Different types of wear mechanisms are described in Table 2-1. In general, two thirds of all wear processes found in industrial situations can fit into the category of adhesive (sliding) or abrasive wear [4] .

| Mechanism | Definition | Characteristic |
|---|---|---|
| Adhesion | Wear due to the transfer of material from one surface to another by shearing of solid welded junctions of asperities | Adhesive bonding, shearing and material transfer |
| Abrasion | Wear due to hard particles sliding through a softer surface | Plowing, wedging and cutting |
| Delamination | Wear by delamination of thin material sheets beneath the interface in the substrate | Plastic deformation, crack nucleation and propagation |
| Erosion | Wear due to mechanical interaction between a solid surface and a fluid, or impinging liquid or solid particles | Large-scale sub surface deformation, crack initiation and propagation |
| Fretting | Wear due to small amplitude oscillatory tangential movement between two surfaces | Relative displacement amplitude and entrapment of wear particles |
| Fatigue | Wear when the exposure to cyclic loading produces progressive or localised damage, resulting in the generation of cracks which can lead to the breaking off and therefore wear of the material | Cyclic loading and fatigue crack propagation |
| Corrosive | Wear when sliding occurs in a corrosive/oxidative environment | Formation of weak mechanically incompatible corrosive/oxide layer |

**Table 2-1 - Different types of wear mechanisms [4]**

### 2.1.1 Adhesive (sliding) wear

Adhesive i.e. sliding wear is defined as the material loss that is the result of two solid surfaces in contact with one another sliding over each other, with one or both surfaces suffering wear. When two surfaces are brought together, asperities on the two surfaces come into contact and support the applied load. When there is relative motion between the two surfaces, the asperities are sheared with the net result being that the softer material is transferred to the harder surface, with either the softer material adhering to the hard surface or breaking to form loose debris [5].

There are a number of factors that have been found to influence the sliding wear of materials, these include the nature of the materials in contact, namely the chemical composition and surface finish alongside the sliding conditions; a schematic is shown in Figure 2-1.

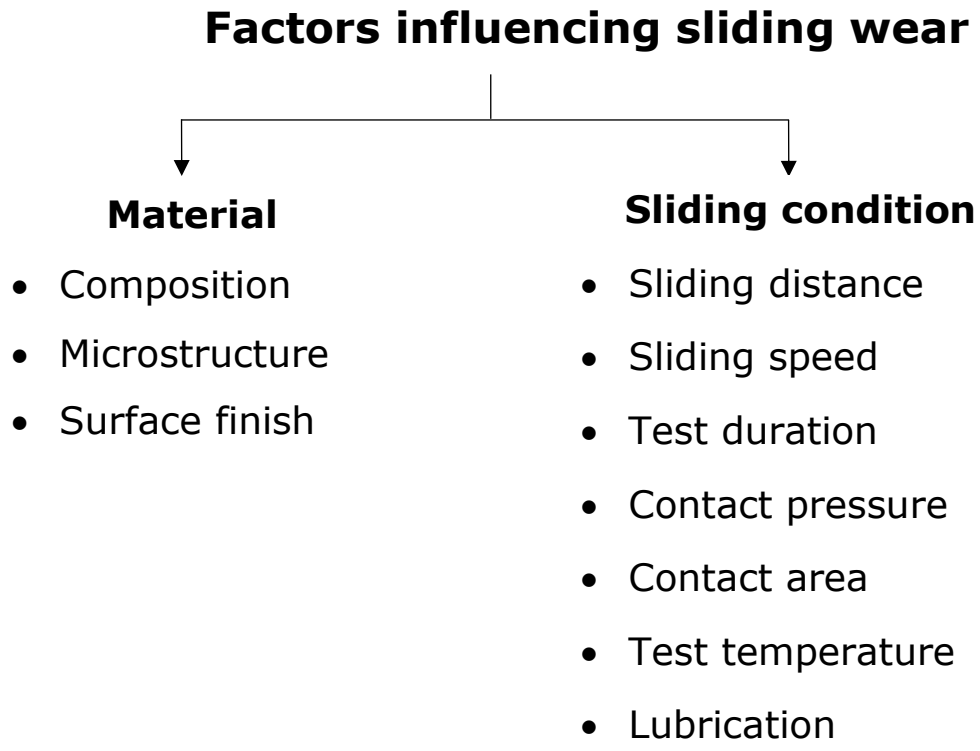


**Figure 2-1: Factors influencing sliding wear**

Archard derived a theoretical expression describing the rate of adhesive wear, suggesting that wear volume is proportional to the load, inversely proportional to the hardness of the softer material and proportional to the sliding distance. [6]:

$$Q = \frac{KW}{H}$$

Where *Q* is overall wear rate (volume per unit sliding distance), K is the dimensionless wear coefficient, W is the normal load and H is the hardness of the softer material.

For many systems undergoing sliding wear, increasing the load can lead to a sudden increase in specific wear rate; this is illustrated by an example of the sliding wear of a α/β brass pin against a hard Stellite ring in Figure 2-2, in which a sharp increase in wear rate is observed when the normal load is increased above 1kgf.

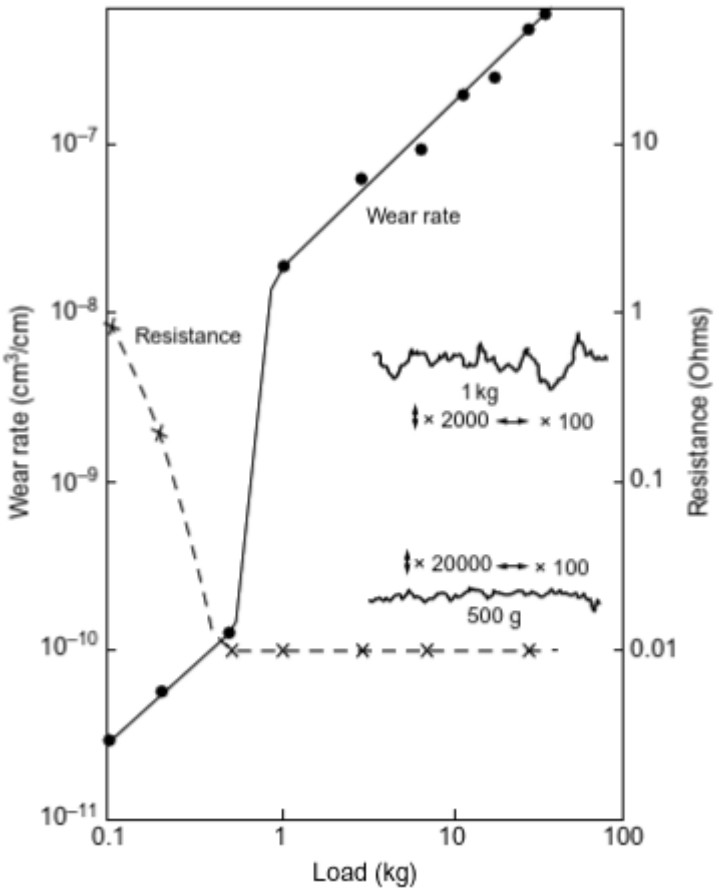


**Figure 2-2 - Sliding wear of an α/β brass pin against a hard Stellite ring [5,7]**

### 2.1.2 Abrasive Wear

In abrasive wear material is removed from the surface by the means of hard particles penetrating a softer surface and displacing material in these areas, resulting in a rough surface. Wear is often seen as a major contributor in the failure of engineering products. The damage can be described as scratching, scoring or gouging depending on the extent of the wear [8]. It can be split into two types of abrasive wear, two-body abrasive wear in which hard particles on the counterbody slide across the surface of the specimen and three-body abrasion where hard particles are trapped between two sliding surfaces, causing wear to one or both surfaces. These two types of abrasive wear are illustrated in Figure 2-3.

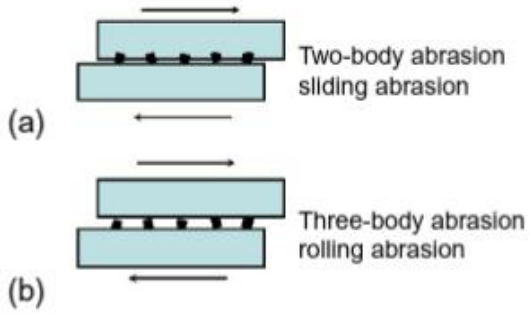


**Figure 2-3 - Mechanisms of abrasive wear. (a) Two body abrasion. (b) Three body abrasion [5]**

## 2.2 Surface Engineering

Surface engineering is defined by the ASM handbook as "treatment of the surface and near-surface regions of a material to allow the surface to perform functions that are distinct from the bulk functions of the material" [9]. This may include improving corrosion and/or wear resistance, electrical

properties, thermal insulation and reducing frictional energy losses amongst others. This can be achieved by either modifying the surface itself by using metallurgical, mechanical or chemical methods or by adding an extra layer on the surface using a form of coating process, known as a thin film or coating. Thermal spraying is one of such coating processes and is commonly used to apply protective or functional coatings onto the surface of engineering components.

### 2.2.1 Thermal spraying

Thermal spraying is a technique that involves depositing metallic or non-metallic materials in a molten or semi-molten state to form a coating, in order to improve the properties of a surface. The sprayed material may be in the form of a powder, ceramic rod, wire or molten materials. These processes involve the molten or semi-molten coating material being propelled towards the substrate by a stream of gas at high velocity and temperature [10]. On impact with the substrate, the particles plastically deform to form a lamellar structure consisting of layers of flattened, disk-like splats [11]; an illustration of the typical microstructure with common features is presented in Figure 2-4. Thermal spraying is a line of sight process, meaning the end of the nozzle must be able to "see" the substrate to deposit a coating.

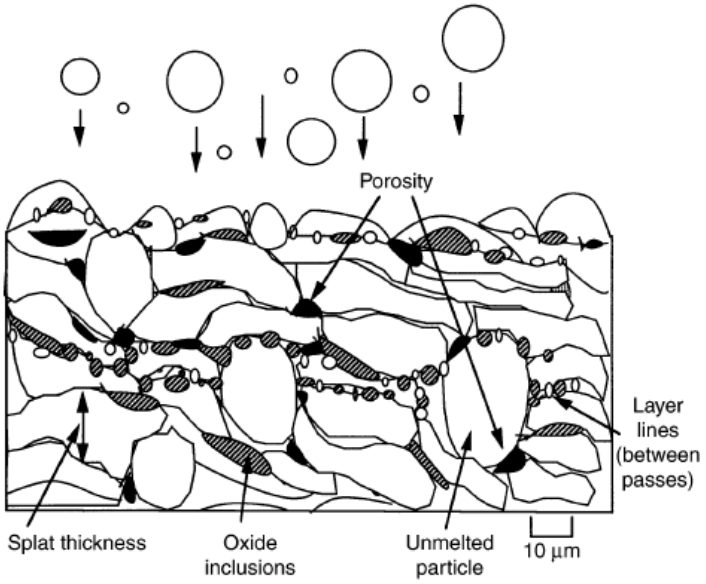


**Figure 2-4 - The microstructure of a typical thermal spray coating [11]**

Thermal spray methods have a few distinct advantages when compared to other coating methods. If a material can melt without decomposing, it can be deposited on a surface by thermal spraying. Furthermore, coatings can be applied without significantly heating the substrate material, meaning materials with very high melting points can be sprayed onto heat treated parts without changing its properties. Any thermal distortion of the part will also be prevented. Thermal spray processes also have a much higher coating rate in comparison to other methods such as electroplating, chemical vapour deposition (CVD) and physical vapour deposition (PVD). The main downside of thermal spray processes is that unlike the above mentioned methods, it is a line of sight process meaning that the spray stream must be in-line with the substrate in order to deposit a coating [11,12].

Thermal spray processes in general can be divided into two main categories; those that use combustion to provide the heat to melt the coating material and those that use electric discharge. A summary of the different types of thermal spray processes and the range of typical particle velocity and flame temperature for different spray processes are displayed in Figure 2-5 and Figure 2-6.

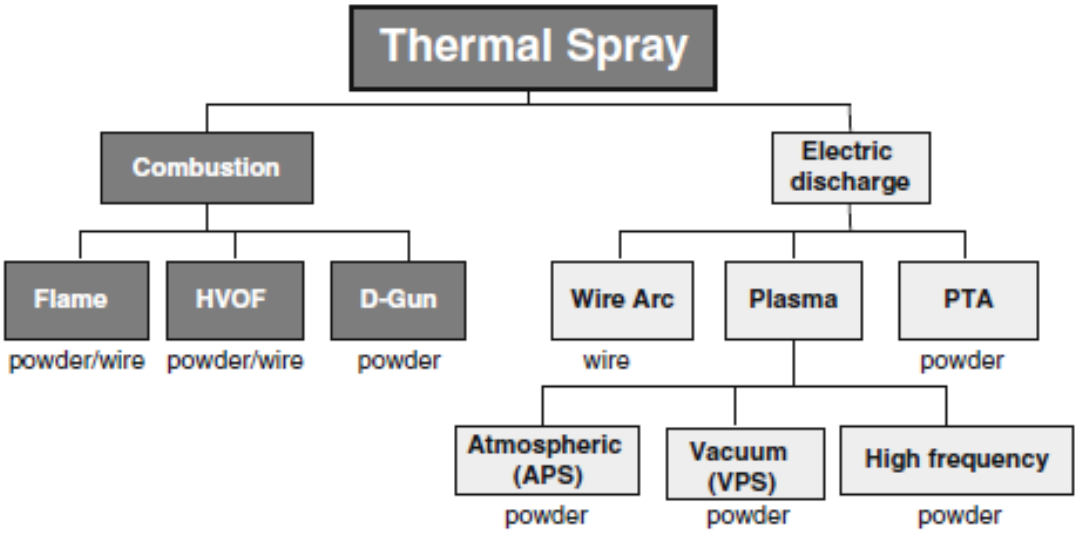


**Figure 2-5 - Summary of thermal spray processes [13]**

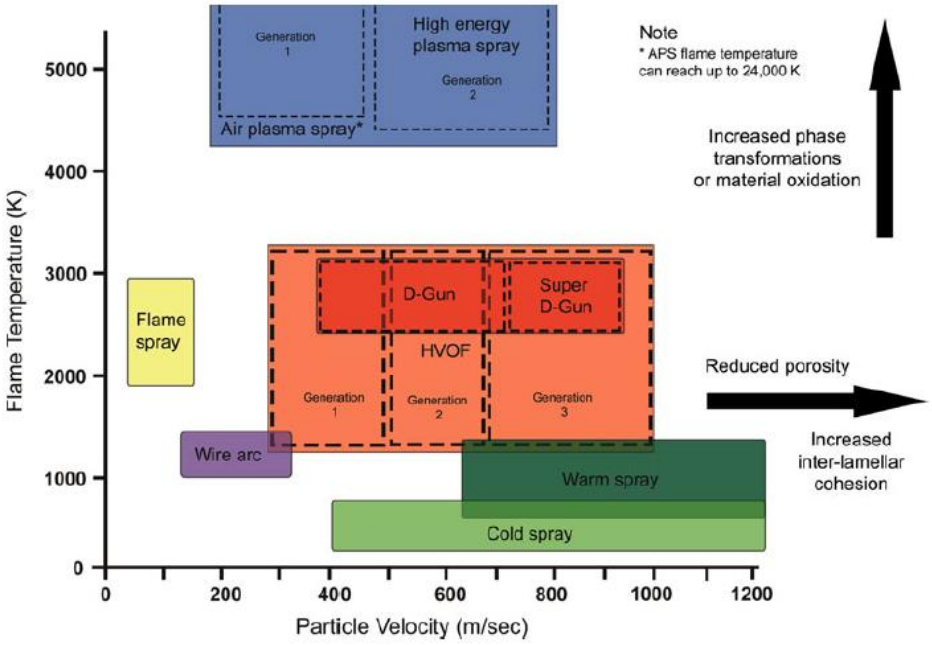


**Figure 2-6 - Classification of thermal spray processes according to flame temperature and particle velocity [14]**

Wire arc thermal spraying requires a wire feedstock and involves passing an electric arc between two electrodes made of the coating material. These two wires are continuously melted, fragmented into droplets and propelled towards the substrate by jets of air [13]. The coating materials used in this process are limited to conductive materials that can be formed into wires [11].

Plasma can also be used as the means to melt the powder feedstock, with electricity being used as the energy source. Atmospheric plasma spraying (APS) is a technique which involves using a jet of plasma to melt and accelerate the coating particles. This plasma jet is created by ionising an inert gas such as argon or helium using an electric arc between a tungsten cathode and a copper nozzle anode in a plasma torch [15]. Vacuum plasma

spraying (VPS) is a similar technique but is carried out in a specialised low pressure chamber in order to reduce the extent of oxidation [16].

The range of thermal spraying techniques that exist in the combustion category shown in Figure 2-5 use the heat generated from the exothermic combustion reaction to melt the powder feedstock. Flame spray is among the simplest and oldest of all thermal spray processes. Powder is fed into an oxy-fuel flame in order to melt the particles, then a flow of compressed air atomises the molten particles and propels them towards the substrate [16]. Detonation gun, or D-Gun thermal spraying, involves an explosive mixture of fuel, oxygen and powder being ignited by a spark plug repeatedly to produce a sequence of detonations. These series of explosions produce detonation-pressure waves that accelerate the molten particles down a water-cooled barrel towards the substrate. Coatings applied using this technique are amongst the densest and hardest of all thermally sprayed materials, due to the extremely high particle velocities observed during processing, which can exceed 500m/s [11].

## 2.3 High Velocity oxy-fuel (HVOF) thermal spraying

High velocity oxy-fuel thermal spraying is a technique that uses the energy produced from combusting fuel under pressure, in a water or air cooled combustion chamber, to melt and accelerate the coating material towards the substrate [11]. Supersonic gas velocities can be generated and the applied coatings have been proven to have low porosity (<1%), low oxide content (<1%) and to be highly adherent to the substrate [17].

The advantages of HVOF thermal spraying over the other thermal spray techniques are as follows. Higher particle velocities can be achieved with HVOF thermal spraying relative to flame spray and wire arc thermal spraying. As a result, the final coatings are often denser with a lower porosity. Furthermore, due to the lower flame temperatures than that observed in the different plasma spraying methods, phase changes of the in-flight particles is less of an issue with HVOF thermal spray [11,14].

In the HVOF thermal spray process gas or liquid fuels can be used; gas fuelled systems generally use fuels such as hydrogen, propylene, propane or acetylene and liquid fuelled systems mostly use kerosene. The advantage of using the liquid fuelled systems is that greater pressures in the combustion chamber can be achieved, resulting in an increased gas velocity compared to gas fuelled systems. This leads to a lower residence time for the particles in the flame for liquid fuelled systems and as a result, the powder feedstock suffers a lesser amount of oxidation or decomposition in comparison to gas fuelled systems [18,19]. However this increased performance comes at a price, as the liquid fuelled systems have been shown to consume about ten times as much fuel by mass as the gas fuelled systems [11].

### 2.3.1 Coating microstructure

The microstructure and performance of an applied coating will not only be influenced by the powder used, but also by the parameters used in the spray process. This is because the properties of in-flight particles, such as

temperature and velocity are affected by the spray parameters chosen. A schematic detailing how certain processing parameters affect the process dynamics and then the final coating is shown in Figure 2-7.

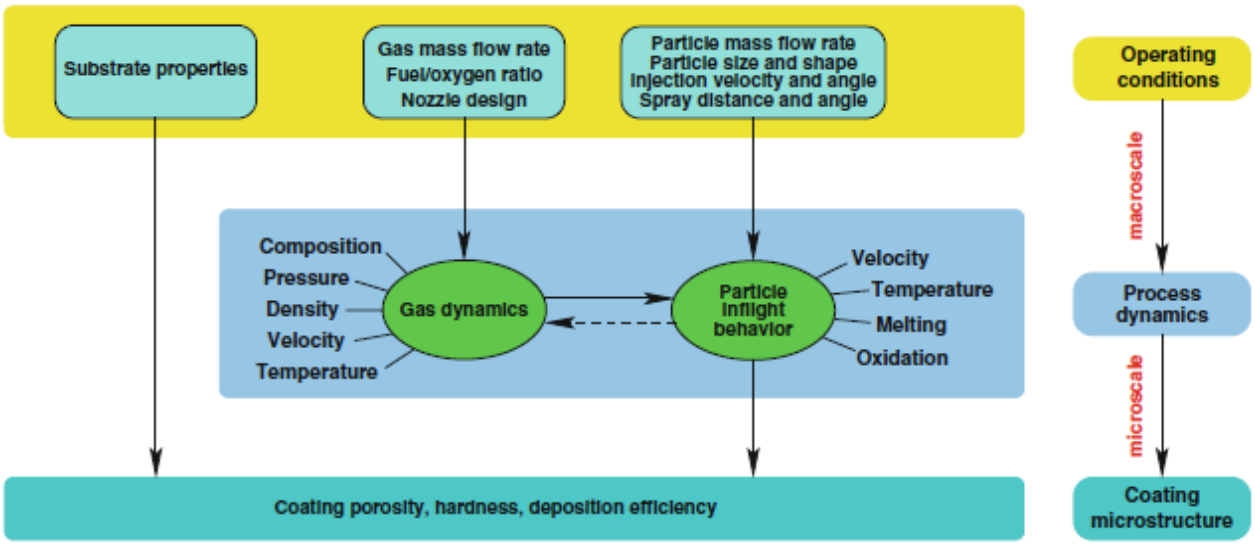


**Figure 2-7 - Multiscale character of the HVOF thermal spray process [20]**

The microstructure of the sprayed coating is affected by the deformation, solidification and sintering of the coating particles when they are deposited on the substrate, as well as the physical and chemical state of the particles at the point of impact. This includes the particle temperature, velocity, melting ratio, and oxidant content. The in-flight particle behaviour is related to the gas dynamics in the process; these are dependent on the spray parameters used, such as fuel type, gas flowrate, oxygen/fuel ratio or stand-off distance [21]. The coating microstructure will also be affected by the in-flight particle behaviour and therefore as a result of this, it is important to ensure that the spray process is carefully controlled and optimised [22].

Two of the most important operating variables to consider are the particle velocity and temperature [23]. This is due to the presence of features such as porosity, unmelted particles and oxides being related to these parameters. Particle velocity has been found to be strongly dependant on the pressure in the combustion chamber, while particle temperature is related to the residence time of the particle in the nozzle of the spray torch [24].

### 2.3.2 Oxidation in HVOF thermal spray coatings

Oxide phases within thermally sprayed coatings have been shown to lower the corrosion resistance and mechanical properties of the coating, and therefore must be kept to a minimum. The powder feedstock can be oxidised in 3 stages of the spray process; the first of these is inside the nozzle itself as the particles will be in contact with the combustion products at high temperatures [25]. Oxidation here can be controlled to a certain degree by changing the oxygen/fuel ratio, but it cannot be fully avoided due to the flame containing oxidising combustion products [26]. The second oxidation region refers to the time when the particles are in the centre of the flame until they impact with the substrate surface; this region can contain up to approximately 20% oxygen and this combined with high temperatures can lead to oxidation.

The oxidation of particles has been modelled with the effect of particle size and powder injection location studied to assess oxidation behaviour of the particles within the nozzle and in-flight. It was determined that smaller

particles oxidised more readily than larger ones because the authors state that the amount of oxidation is directly affected by temperature change and available oxygen, with the quantity of oxygen entrained in the flame for HVOF thermal spray systems being strongly influenced by the jet velocity [27]. As smaller particles will reach higher temperatures during spraying than larger ones, more oxidation will take place when spraying with smaller particles. The effect of introducing the powder feedstock into the combustion chamber was compared with powder injection at the end of the supersonic region of the flame with the model, and it was found that much higher levels of oxidation are predicted for the former. This is due to particles reaching a much higher temperature when injected directly into the combustion chamber, as well as a larger amount of oxygen being available for combustion due to the pressured air directly entering the chamber [28].

The final region where oxidation takes place is in the period between when a particle has collided with the substrate and when the next layer covers it up. In the above scenario, particles are still exposed to oxidising products in the flame and the high temperatures, although these are lower than in the other regions [25]. This process again is influenced by higher particle temperatures, but also can be affected by the shape of the splat; splats with a higher flattening ratio have an increased surface area to volume ratio, and as a result will react more rapidly [29].

### 2.3.3 Porosity in HVOF thermal spray coatings

Porosity in a coating is an important characteristic and can strongly influence its properties. Coatings with high levels for porosity for example may provide reduced protection from corrosion, as interconnected pores can provide a channel for corrosive species to diffuse down through the coating to the coating/substrate interface. For wear resistant coatings, porosity may lower the coating's performance because the presence of voids may lower the coating hardness and surface finish; furthermore, many wear resistant coatings also require corrosion resistance too, greatly increasing the need to reduce porosity. The formation of pores in the coating microstructure can be attributed to the presence of unmelted particles, therefore careful process optimisation can ensure porosity is minimised. Unmelted particles may not deform sufficiently on impact with the substrate due to them being less soft, leading to a less homogenous lamellar coating structure. This can produce gaps in the structure that can be seen in the form of porosity. Other sources from which porosity can originate include, splat shrinkage during solidification on impact with the substrate [30,31], poor intersplat cohesion, leading to splats breaking apart, porosity inherent to the powder feedstock and spraying at high deposition angles, which leads to shadowing (Figure 2-8) [11].

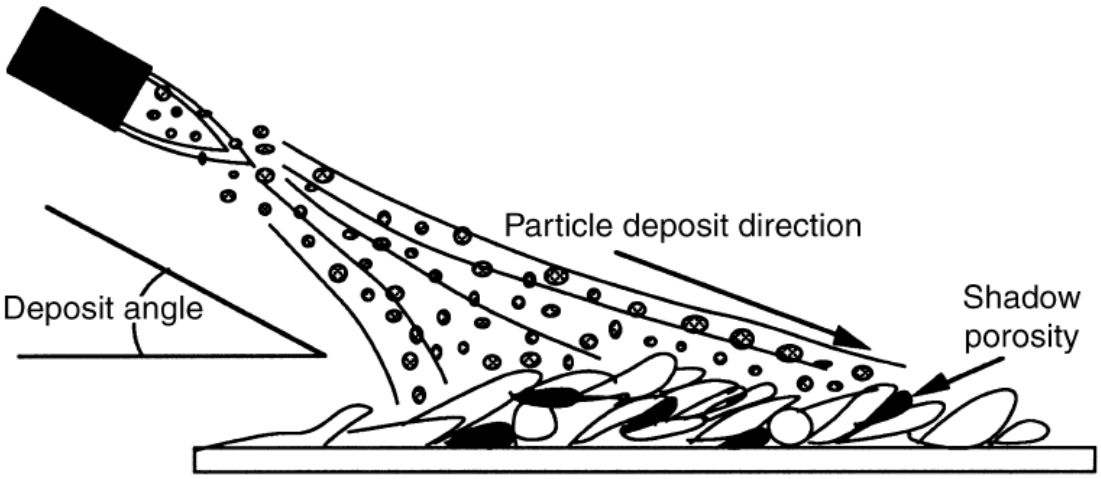


**Figure 2-8 - Porosity formation from spraying at high deposition angles [11]**

### 2.3.4 Effect of stand-off distance in HVOF thermal spraying

Stand-off distance, also known as the torch-to-substrate distance, is the distance from the end of spray torch to the substrate. This parameter must be kept constant during the spray operation in order to keep an unchanging coating thickness [11]. When considering ID-HVOF thermal spraying, particularly when applying a coating in a small, confined space, the stand-off distance may be a limiting factor. This is because the distance may not be large enough to produce a quality coating. The effects of applying coatings using different stand-off distances was investigated by Lih et al. [32] with their results shown in Figure 2-9. They sprayed chromium carbide/nickel chrome coatings by HVOF thermal spraying and measured the in-flight particle temperature and velocity using the DPV-2000 (Tecnar, Canada), which employs a two colour pyrometer and a digital scope board.

The velocity of the particles is measured by the time taken for the particle to pass by two slits separated by a known distance. Temperature is calculated from the Planck law of thermal radiation from the intensity of two spectra of the pyrometer at wavelengths of 787±25nm and 995±25nm.

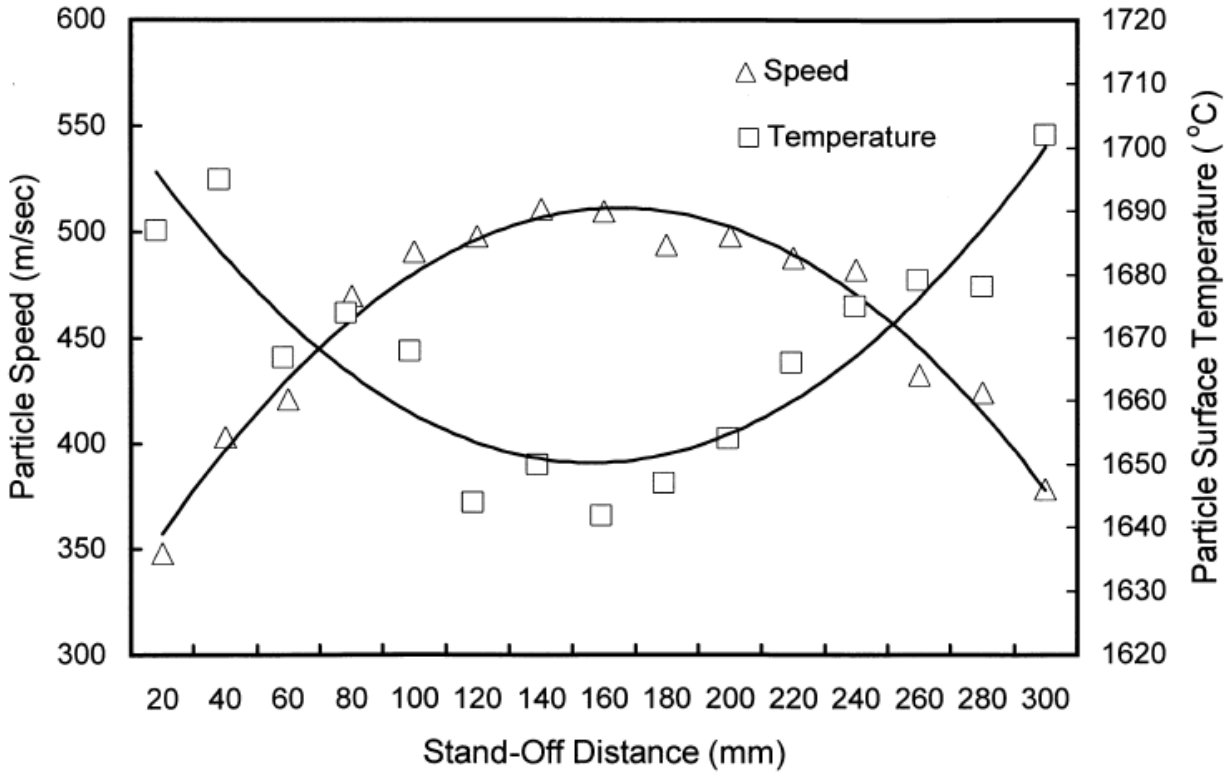


**Figure 2-9 - In-flight particle speed and temperature vs. stand-off distance when spraying a CrC/NiCr powder with HVOF thermal spraying [32]**

At the lowest stand-off distance of 20mm, the particle velocity is at its lowest point of 350m/s, whilst the particle surface temperature was measured at its second highest peak of approximately 1700°C. As the spray distance was increased, the particle velocity was seen to rise, up to its highest point of 500m/s at a stand-off distance of about 140-160mm. Raising the stand-off distance any further leads to reduced particle velocity.

The effect of stand-off distance on the particle surface temperature however appears to be the reverse; higher particle surface temperatures were measured at the smaller spray distances, with the temperature reducing as distance is increased. The smallest surface temperature appears to also be at a spray distance of about 140-160mm, which coincides with the highest particle velocity. These results can be explained by the fact the distance of 140-160mm measures to be approximately the length of the visible jet core. Within this region, the particles are continuously accelerated, due to the kinetic energy contained in the flame overcoming the retarding force from the entrainment atmosphere. However once outside the jet core, the retarding force overcomes the accelerating force from the flame, leading to the drop in velocity [32]. This result was also observed in another study [33]. The cooling of the particle's surface temperature is due to the mixing with the entrainment air, especially near the end of the visible plume [34]. However, oxidation reactions occurring with the atmosphere could increase the surface temperature. Due to the exothermic nature of oxidation, this could explain the temperature rise.

Due to the much lower particle velocity and high temperatures measured at short standoff distances it is clear that spraying coatings under these conditions, using the spray system used by Lih et al. may not produce optimal quality coatings. This study did not contain any microstructural characterisation of coatings sprayed at the short stand-off distances and therefore the coating microstructure is unknown.

## 2.4 Internal diameter (ID) thermal spraying

Internal diameter (ID) thermal spraying is a thermal spay application that refers to coating the inner surfaces of objects such as cylindrical parts with small diameters. As a line of sight process, thermal spraying has limitations linked to the geometry of the part to be sprayed.

For cylindrically symmetrical parts with a small depth, off angle spraying can be used in which the spray torch is positioned at an angle in order to point into the part to allow line of sight between the end of the nozzle and the substrate surface, as displayed in Figure 2-10. This leads to the elongation of splats, the formation of porosity as shown in Figure 2-8 and less homogeneity in the distribution of phases throughout the coating microstructure. The deposition efficiency is also greatly affected by the spraying angle, with a greater number of passes required to produce the same coating thickness when spraying off angle, meaning the process is less economical [35].

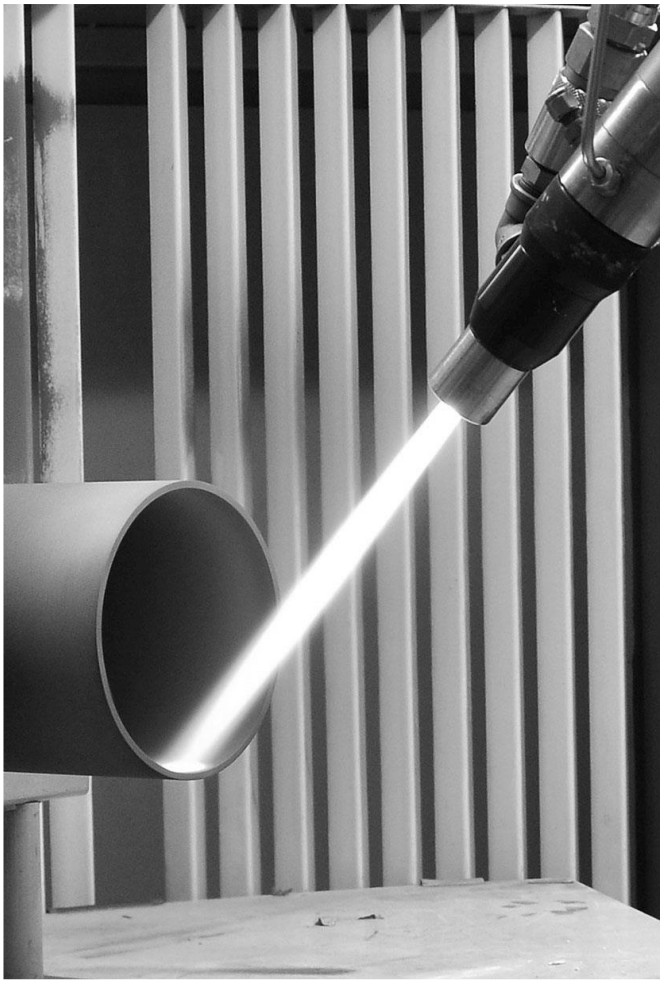

**Figure 2-10 - Image of "off angle" thermal spraying of a tube with a 160 mm internal diameter [36]**

It has been previously shown that off-angle sprayed coatings exhibit a lower hardness and lower compressive residual stress than coatings sprayed at 90° meaning spraying at an angle leads to a reduction in wear resistance [37–39] ; the microhardness of a WC-Co-Cr coating as a function of spray angle is displayed in Figure 2-11.

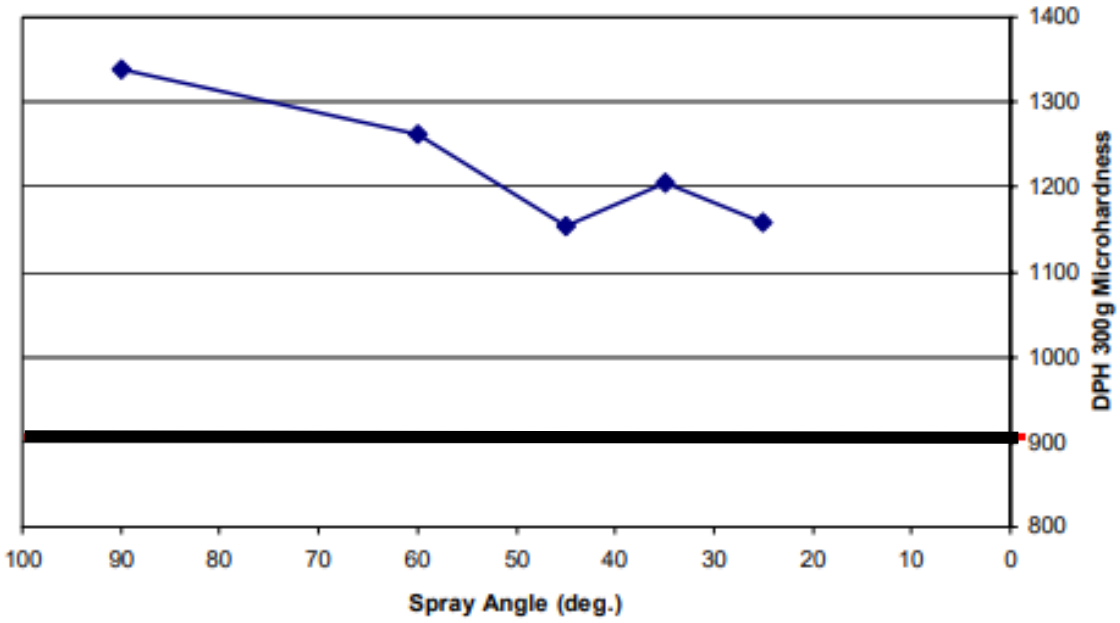


**Figure 2-11 - Effect of spraying angle on the microhardness of a WC-Co-Cr coating [38]**

In order to apply coatings on parts with a greater depth using the method shown in Figure 2-10, the spray angle would have to be reduced to a level in which the quality of the coating would greater suffer, meaning it is not feasible. Therefore in order to coat these parts, a new generation of spray torches have been developed that have a much shorter barrel length meaning they can fit inside the part to be sprayed and apply a coating with a consistent spray angle (for a cylindrically symmetrical part) [40–42]. An example of such a spray torch is displayed in Figure 2-12.

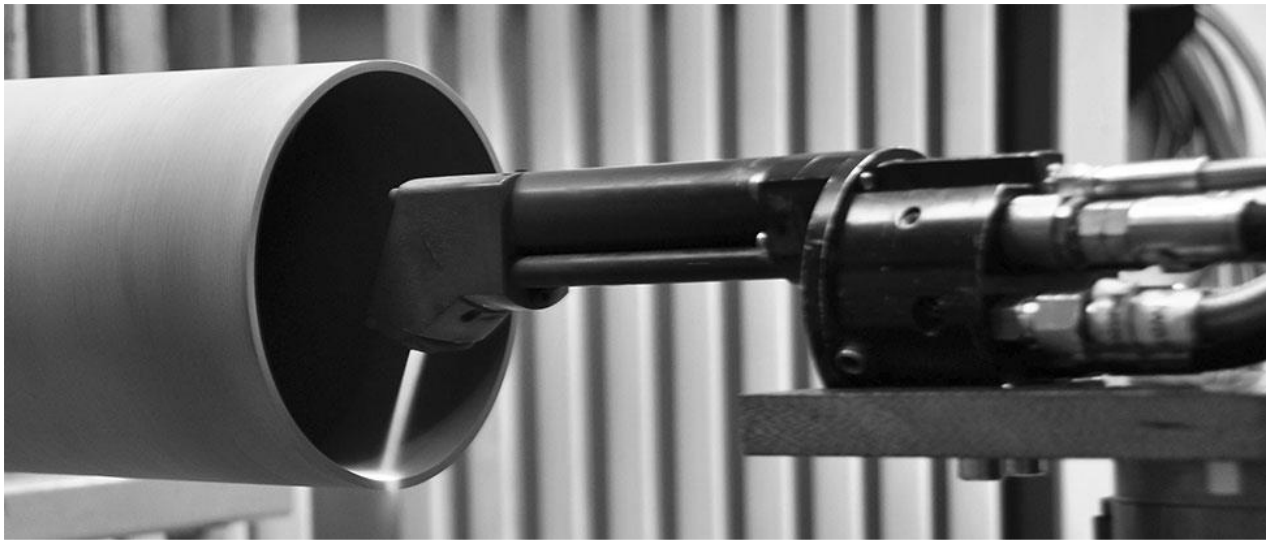

**Figure 2-12 - Example of an ID thermal spray being used to coat the inner diameter of a cylindrical part of diameter 160 mm (IDCoolFlow Mono, Thermico GmbH, Germany) [36]**

In order to apply coatings in small internal diameters, not only does the size of the torch have to be smaller than conventional spray systems designed to coat external surfaces, but also the torches need to be able to operate with much shorter stand-off distances. As previously established and displayed in Figure 2-9 in-flight particles are often still undergoing acceleration at short stand-off distances, with the end result being poor coatings due insufficient velocity on impact with the substrate [32]. To solve this issue feedstock spray powders with particle sizes less than 20μm are often employed [43], as particles with a lower mass will achieve a greater in-flight velocity than heavier particles when sprayed under the same conditions. However due to the increased in-flight temperature, more in flight oxidation of the particles may occur when spraying a finer particle feedstock due to the higher surface area to volume ratio than larger particles of the same material [44]. It has been previously shown that finer particle feedstocks tend to follow the gas flow trajectories more strongly

than larger particles and due to the gas flow near the substrate diverging from the substrate surface, smaller particles may follow this and not be deposited onto the substrate [45].

Another challenging aspect of applying coatings on internal surfaces is related to the temperature control of the substrate material. As described in Section 2.3.2, oxidation of the coating material can occur following the impact of particles on the substrate and higher substrate temperatures are linked to increased oxidation of the deposited splats due to the slower quenching of the splats as a result of the reduced temperature difference between splat and substrate [46]. When spraying external surfaces, the use of air or even water cooling of the substrate material is well established [47], however this is more challenging when it comes to the cooling of internal surfaces. Special cooling methods such as tube/bore cooling or small air-jet systems are required for substrate temperature control [36]; however currently there is no information available providing in depth knowledge of substrate cooling processes for ID thermal spray.

Currently there are not many published studies in which coatings have been applied on internal surfaces using thermal spraying. Lyphout and Bjorklund used an ID-HVAF (High Velocity Air Fuel) system developed by UniqueCoat Technologies (Virginia, USA) to spray coatings of WC-Co-Cr and $Cr_3C_2$-25NiCr onto the internal surface of cylinders with an internal diameter of 200mm. An external air unit was used during the operation to ensure the removal of residual particles and to help control the part temperature. High

deposition efficiencies with low coating porosity were achieved with both powders; however a few cracks were found in the centre of the WC-Co-Cr coatings, which the authors hypothesised were due to tensile residual stresses within the coating originating from overcooling on the outer diameter of the substrate. Reducing the temperature of the substrate part by increasing the cylinder length was discussed, though this was found to increase the amount of residual dust within the system. As a result it was recommended that if possible the temperature of the part, including the external surface, should be monitored throughout the spray process in order to help prevent crack formation in the coating [1].

Tillmann et al. used an ID-HVOF system developed by Thermico GmbH to spray a bond coat and an APS-ID thermal spray torch (SM-F100 Connex, Oerlikon Metco) to spray a ceramic top coat of CoNiCrAlY. Samples were sprayed onto flat substrates however, not onto an internal surface as was done in the previously mentioned study. To simulate an ID application the stand-off distance used in the ID-APS spraying was 70mm. To investigate the effect of stand-off distance when spraying the bond coat, the in-flight particle temperature and velocity were measured using an in-flight particle measurement tool at a range of stand-off distances from 10mm to 110mm. It was determined that the best coatings sprayed by ID-HVOF were achieved at a spray distance of 53mm, meaning that taking into account the dimensions of the spray torch, the minimum diameter of a part than could be sprayed with this spray torch is 133mm. These coatings were found to have a porosity between 3 – 4%. It was determined that the in-

flight particle velocity could be increased by the addition of adding $N_2$ into the combustion chamber, with the inflight particle velocity increasing from under 1100m/s up to 1200m/s when $N_2$ input flowrate was raised from 70L/min to 130L/min [36].

## 2.5 WC-Co-Cr HVOF thermal spray coatings for wear resistance applications

WC-based cermets are commonly used materials for use in coatings designed to protect surfaces from wear, due to their high hardness and resistance to sliding wear. The idea is to combine the hard nature of the ceramic WC with the toughness of a metallic binder phase. An ideal metallic binder would prove good wettability with respect to the ceramic and is selected based on its melting point, alongside the strength and toughness it provides.

WC-Co-Cr cermet thermal spray coatings have been increasingly used in a number of industrial sectors, for example in the oil and gas, aerospace and automotive industries, due to their well proven high wear and corrosion resistance [48,49]. The material was developed for use in applications where corrosion can take part in wear degradation processes [50]. In comparison to WC-Co, it has been shown that WC-Co-Cr provides better erosion-corrosion performance, due to the addition of Cr into the Co matrix changing the main corrosion mechanism. Alongside improved corrosion protection compared to WC-Co, WC-Co-Cr coatings have been shown to offer a comparable hardness and wear resistance [19]. The addition of

chromium to the binder phase has also been shown to inhibit to a certain extent the decarburisation of WC-Co, which may lead to better coatings when spraying material with nano sized WC grains compared to WC-Co [51].

### 2.5.1 Decarburisation processes in WC-Co-Cr thermal spray coatings

One challenge that must be overcome when applying coatings of WC-Co or WC-Co-Cr is that of decarburisation. The WC phase reacts due to the high temperatures and presence of atmospheric gases during thermal spraying to form unwanted phases such as $W_2C$ or W [52], which are said to lower the coating's fracture toughness and resistance to sliding wear [53].

One chemical route of the decarburisation of the WC phase in APS thermal spraying was proposed by Vinayo et al., as follows [54]:

$$2WC \rightarrow W_2C + C$$

$$W_2C + ½\ O_2 \rightarrow W_2\,(C,O)$$

$$W_2\,(C, O) \rightarrow 2W + CO$$

Although decarburisation is expected to be more severe in APS thermal spray processes in comparison to HVOF thermal spray, due to the higher temperatures reached by the in-flight particles, the presence of $W_2C$ and even W has been widely detected in WC based HVOF thermal spray coatings [19,55,56].

Kear et al. described how the decarburisation process occurs during thermal spraying. The mechanism for the formation of the $W_2C$ phase is believed to be as follows: the cobalt binder phase will melt before the WC phase, due to its lower melting point. At this point, WC will begin to dissolve into the molten binder phase; after which carbon will begin to be removed from the solution by reacting with oxygen at the liquid/gas interface, to produce carbon monoxide. On impact the system is rapidly quenched and the Co liquid mixture becomes supersaturated, resulting in the formation of $W_2C$ phases. If excessive carbon loss has occurred, pure tungsten may also form [57,58]. A schematic of the decarburisation mechanism proposed by Kear et al. is presented in Figure 2-13.

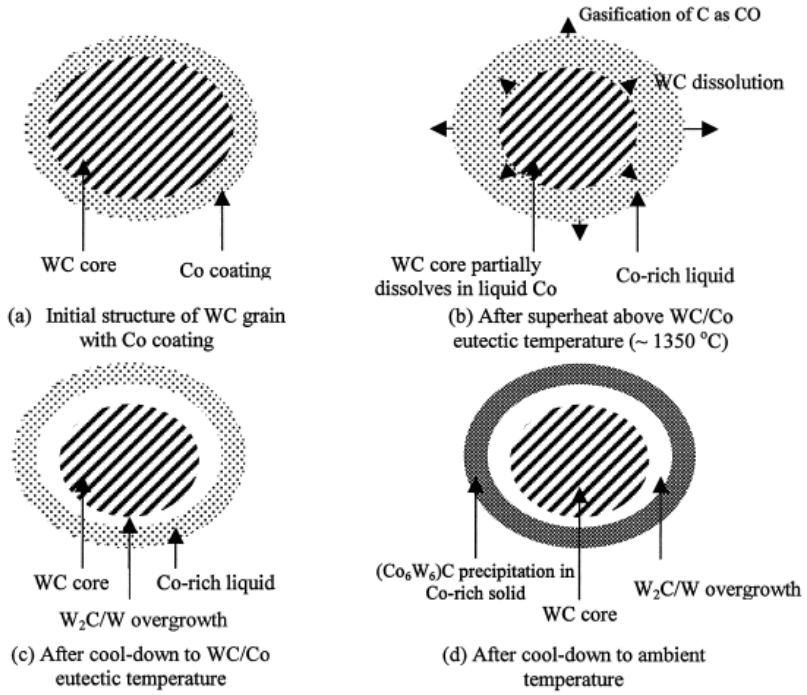


**Figure 2-13 - The decarburisation of WC proposed by Kear et al. [57]**

WC grains that have suffered decarburisation have been described as having a rounded appearance that are either partially or fully enclosed by $W_2C$ crystals that have nucleated and grown on the WC /binder phase boundary by others [58,59] The mechanism shown above can be further complimented by referring to the phase diagram of the W-C system in Figure 2-14. Different forms of $W_2C$ begin to form if the carbon percentage is below 50% when temperatures above 1500K are reached. This is in the range of the flame temperatures found in the HVOF thermal spray process (1000K – 3000K) shown in Figure 2-6, meaning processing this materials by HVOF thermal spray may lead to the WC phase decomposing into $W_2C$. At high concentrations of W (approximately greater than 80% W), elemental tungsten can form if temperatures of 2673K are reached.

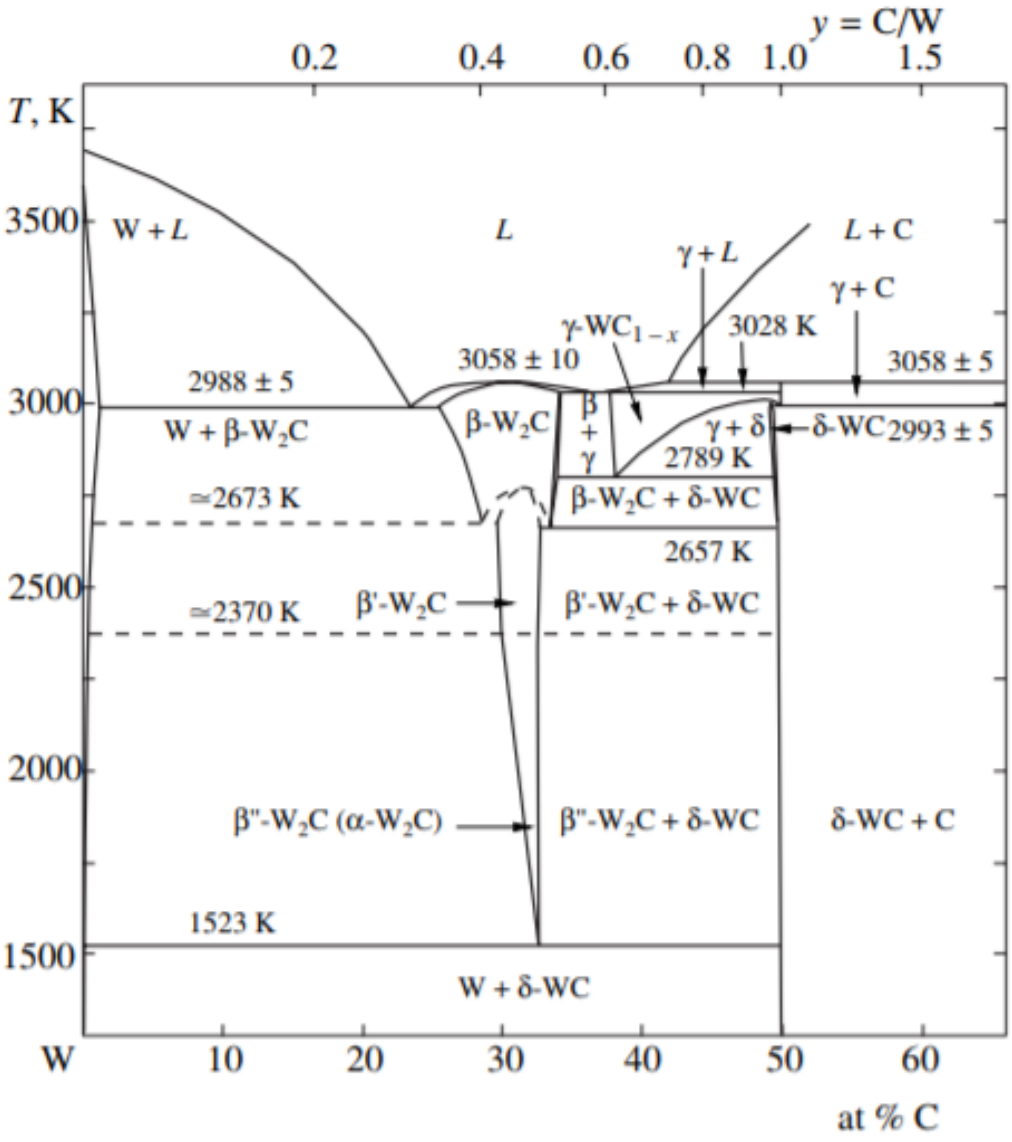


**Figure 2-14 - Phase diagram of the W-C system [60]**

### 2.5.2 Powder and Coating characterisation

WC-Co-Cr powders used in studies where coatings are applied by HVOF thermal spraying are often commercially available powder feedstocks with a composition of 86% WC, 10% Co and 4% Cr (mass %) manufactured by the agglomerating and sintering process with an average size of 45μm. The microstructure of these materials has been well studied with many works

spraying these powders by HVOF thermal spraying [61–68]. The morphology of these powders is described as being roughly spherical with some internal porosity [49,69], with an SEM image showing the morphology of an example of agglomerated and sintered WC-Co-Cr powder given in Figure 2-15.

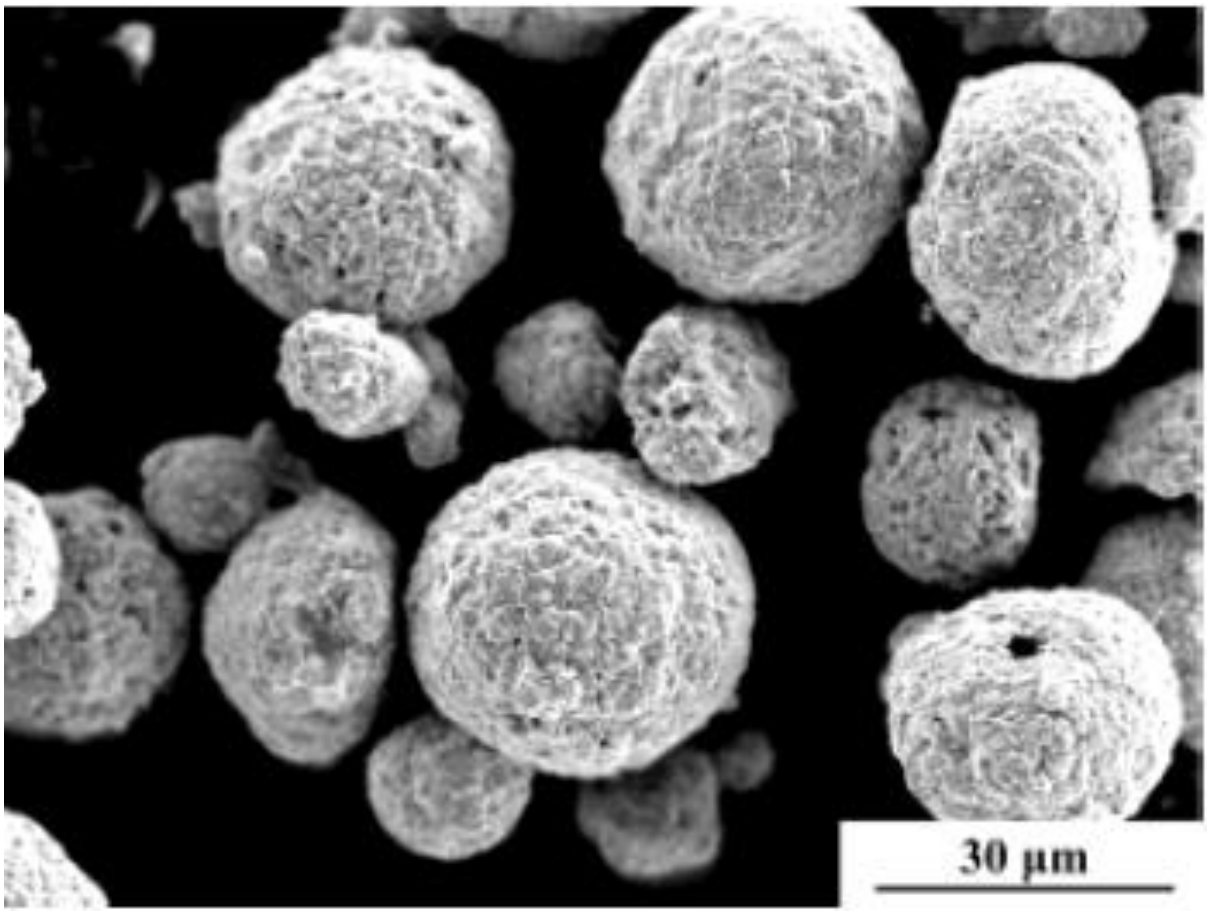


**Figure 2-15 - SEM image showing the morphology of a typical agglomerated and sintered WC-Co-Cr powder [61]**

The phase composition of WC-Co-Cr powders has been investigated in more detail in several studies. Jacobs et al. characterised the WC-10%Co-4%Cr powder AMDRY 5843, produced by Sulzer Metco; its nominal size distribution is quoted by the manufacturer at being -45+16µm, with the

powder being manufactured by the sintering and crushed method. Using XRD, the phases WC, the η-phase $(Co, W)_6C$ were detected. The diffraction lines for the η-phase were shifted to lower lattice parameters, which the authors suggested indicates that a substitution of cobalt atoms by chromium atoms in the crystal structure took place. Alongside these phases, a wide low intensity peak was detected, which indicated the presence of $Cr_7C_3$. Using SEM to image the cross section of the powder in backscattered electron imaging mode, 2 distinct phases were observed in the binder, a cobalt rich phase and chromium rich phase. The total carbon content was found to be approximately 5.31% [70,71].

Guilemany et al. studied the same material as the previously mentioned study, using transition electron microscopy (TEM), XRD and wavelength dispersive spectroscopy (WPS) to characterise the powder. They concluded that 4 main phases were present in the powder microstructure, WC, $Co_3W_3C$, $Cr_{23}C_6$ and metallic Co. The carbon content of the material was determined to be 5.39%, similar to the value found by Jacobs, Hyland and De Bonte [70,72]. Schwetzke and Kreye observed that the phases present in a different sintered crushed WC-10%Co-4%Cr powder were WC, $Co_3W_3C$ and Co. the carbon content was found to be 5.2% [19]. A phase diagram of the WC-Co system calculated at 10% wt. Co is displayed in Figure 2-16. At a carbon content of 5.2% wt, WC, $Co_3W_3C$ and Co FCC phases can be seen to form between the temperature range of 1100°C – 1350°C; this shows the phases detected by Schwetzke and Kreye can coexist.

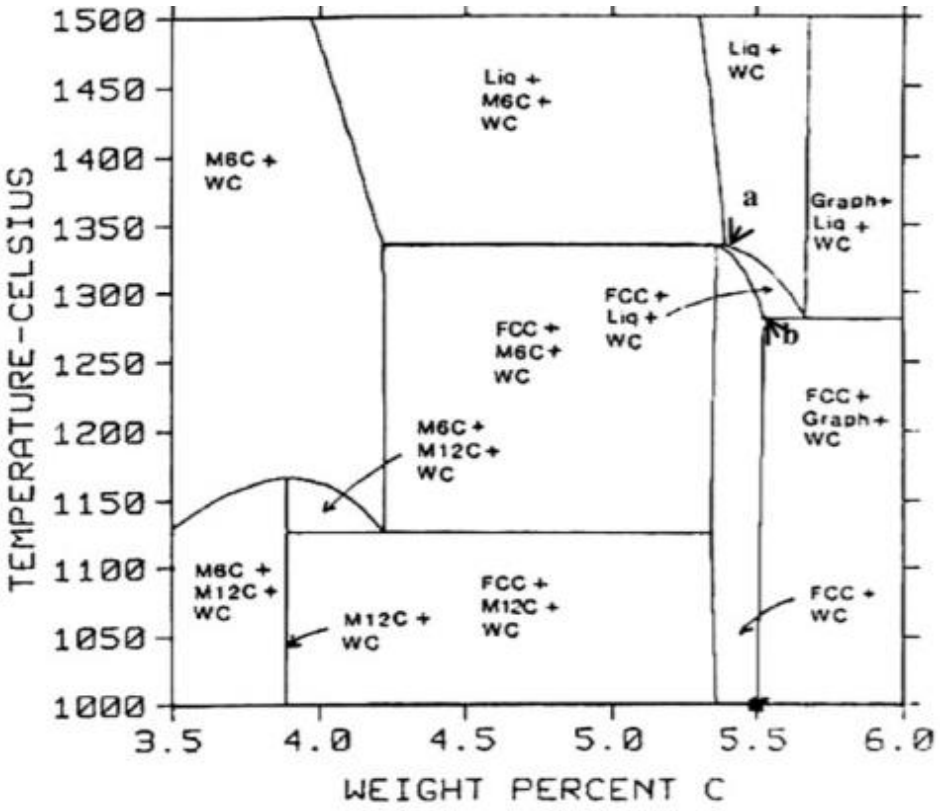


**Figure 2-16 - Phase diagram of the WC-Co system calculated at 10 % wt. Co. The points denoted by a and b define the minimum and maximum carbon contents of alloys which are in two-phase state of fcc + WC just after equilibrium solidification. [73]**

All 3 studies determined that separate cobalt rich and chromium rich phases were present in the binder phase of the powders. However, the work conducted by Jacobs et al. differs from the other two studies, when suggesting that $(Co, W)_6C$ was present, rather than the $Co_3W_3C$ suggested by the other 2 sets of authors. All 3 studies determined that the carbon content of the material was similar.

WC-Co-Cr coatings may contain a number of different phases than the original feedstock powder, due to the fact that significant phase transformations during spraying are common in WC cermet coatings sprayed using HVOF [64]. A number of distinct phases can be observed

throughout the microstructure of a WC-Co-Cr coating; blocky WC grains are surrounded by a binder phase of mixed composition, in a similar fashion to what was observed in the WC-Co-Cr powder.

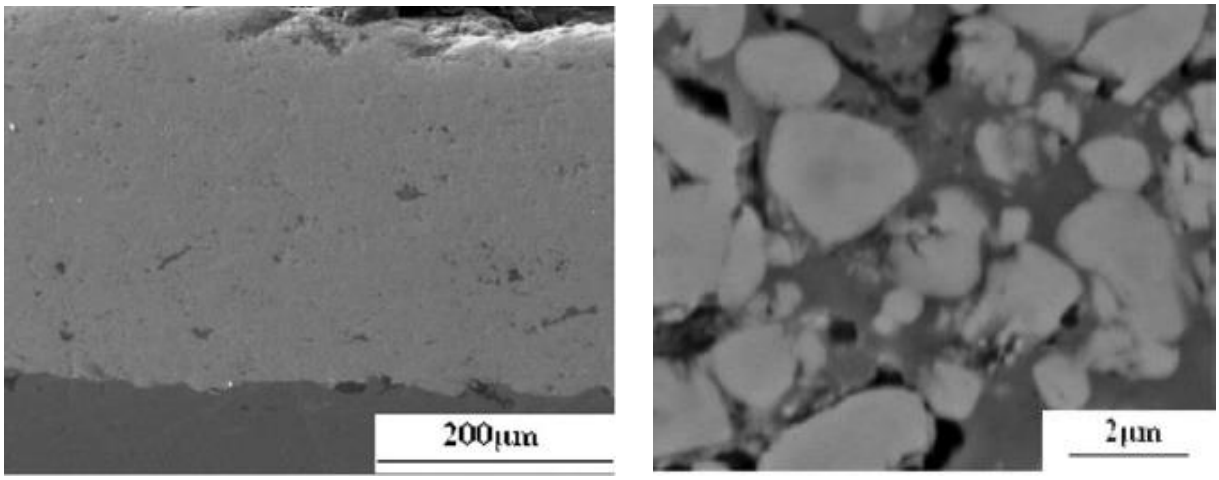


**Figure 2-17 - SEM images of the cross section of a WC-Co-Cr coating [62]**

The lighter phase and darker areas of the binder can be seen in Figure 2-17; the brighter areas have been reported by energy dispersive X-Ray spectroscopy to be Co rich, while the darker phases are Cr rich [62,70]. EDX mapping has shown that no cobalt, and only a small amount of chromium, is detected within the blocky WC grains. Berger et al. theorise that as cobalt and chromium both form extensive solid solutions, the probability of metallic Cr and Co existing together without forming alloys is low; most likely a chromium rich carbide such as $(Cr, Co, W)_7C_3$ has formed, alongside metallic Co [51]. However other authors disagree with this hypothesis, with Bolelli et al. stating that the metal matrix consists of pure Co with large particles of pure Cr, not in a solid solution [74]. They reported detecting tungsten heavy phases of WC, $W_2C$, $Co_3W_3C$ and $Co_6W_6C$, oxide phases such as $Co_3W_3O$ and CoO and pure metal phases Cr and Co.

Referring to the phase diagram in Figure 2-16, the presence of $M_{12}C$ carbides ($Co_6W_6C$) is likely due to a lower carbon content, either due to decarburisation processes or simply the carbon content in the powder feedstock was lower.

In the 2θ range from 35° to 45° phases are present, represented by the broad peaks. This is due to the dissolution of Co to form the oxide phase $Co_3W_3O$, as well as the existence of the $(W,Cr)_2C$ and $WC_{(1-x)}$ phases. The presence of pure Co metal was confirmed during the study by XPS, which agrees with the hypothesis made by Berger et al., regarding the existence of metallic cobalt in the binder phase [50].

### 2.5.3 Effect of changing WC grain size

Changing the grain size in WC cermets has been shown to be one parameter than can alter the properties and performance of thermal sprayed coatings. In theory, according to the Hall-Petch relationship, reducing carbide grain size should increase the strength of the material, due to the fact that reducing the grain size will increase the grain boundary size:

$$\sigma_y = \sigma_0 + {}^{k}/_{\sqrt{d}}$$

Where $\sigma_y$ is yield stress, $\sigma_0$ is a material constant, k is the strengthening coefficient and d is the average grain size.

When considering microhardness, this expression can be adapted to show how microhardness is linked to grain size; this is shown below [75]:

$$H = H_0 + {k_H}/{\sqrt{d}}$$

Where H is microhardness, d is average grain diameter and $H_0$, $k_H$ are material constants.

Using this relation, it is clear that reducing the carbide grain size should increase the material's microhardness. As the grain size is lowered for a coating of a given composition, the mean free path will be lowered. As a result, the soft, ductile matrix will be less exposed, meaning the coating will provide better wear resistance [55]. Reducing the grain size will also increase the fraction of atoms in the material that lie in grain boundaries; as a result of this the material's toughness will rise [76]. As the material's hardness and fracture toughness are increased, it should offer higher levels of wear resistance; therefore, in theory coatings sprayed from nano WC grain sized powders should offer better wear resistance.

The tungsten carbide grain size has been shown to have an effect on the amount of decarburisation that takes place in certain studies. Guilemany, Dosta and Miguel used WC-Co powder with different WC grain sizes, ranging from nano grain sizes (sub 100nm) to grain sizes of 1-4μm. They observed that when spraying the powder with the nano WC grain size, decarburisation was more prominent than when spraying powder with a larger WC grain size. Chung's method [77] was performed to determine the

decarburisation ratio, and the amount of $W_2C$ detected in the coatings sprayed with the powder with nano WC and larger grain sizes were 22% and 8% respectively. The authors reasoned that the increase in decarburisation when spraying WC-Co with a smaller WC grain size was due to the higher surface-to-volume ratio of the WC phase. They also stated that the smaller particles will experience higher temperatures during the spray process than larger ones, and this would also lead to increased decarburisation[78].

However, the results of certain studies conflict the theory that smaller WC grain sizes give better wear resistance; Stewart et al. sprayed samples with two separate WC-Co powders with carbide grain sizes of 2μm and 75nm, and found that under a wide range of abrasive test conditions, the wear rates of the nano grain coatings were between 1.4 and 3.1 times higher than the larger grain coatings. The authors concluded that this was due to excessive decarburisation taking place during the spray process for the nano grained WC-Co powder. The decarburisation process results in a tungsten rich binder phase which has been shown to be a preferential path for crack propagation, indicating that decarburisation may produce a more brittle binder phase. As the smaller carbide grain sizes will suffer more decarburisation during spraying, this effect may be more pronounced in their coatings [55]. It has been argued however that a small degree of decarburisation could be beneficial for the wear performance of WC-Co coatings. Verdon et al. found that too little decarburisation resulted in a large amount of material removal by fracture along brittle island

boundaries, while too much decarburisation lead to the WC dropping to a level where the binder phase was too exposed to erosion [79].

### 2.5.4 Effect of particle size

As was discussed in Section 2.4, the use of fine particle feedstock may be required for use in ID-HVOF applications to counteract the short stand-off distances and smaller dimensions of the spray torch itself. Tillmann et al. applied coatings of WC-10%Co-4%Cr using a powder feedstock with a particle size range of -10+2μm and measured the in-flight particle temperature and velocity when using different spray parameter sets in which the fuel and oxidising gas flowrates were altered. It was determined that fine powders can lead to high quality coatings with low porosity and surface roughness. However smaller particles were shown to be highly influenced by the divergent gas flow of the spray jet and due to their low mass inertia, the velocity of fine particles is more strongly affected by pressure nodes in the divergent supersonic flow. In particular, the effects of bow shock lead to the deflection of fine particles and may lead to some not being deposited on the substrate. Overall a deviation in the deposition rate of up to 23% was measured with differing spray parameters. The amount of decarburisation occurring increased when the fuel flowrate was raised, due to higher particle temperatures [80]. Data comparing different powder size ranges sprayed under the same conditions could be not found.

### 2.5.5 WC-Co-Cr coating performance for wear applications

WC-Co-Cr coatings can be used for resistance from sliding, abrasive and erosive wear at temperatures up to 500°C [63]. With respect to cermet coatings sprayed by HVOF, it has been reported that the abrasive wear rate is dependent on a number of factors; these include the morphology of the starting powder and the size, distribution and hardness of the carbide phase. The coating process itself is also of great importance, as this will influence coating properties that affect wear resistance, such as density, the phases present and residual stresses [81,82].

The abrasive wear mechanisms observed in WC-Co-Cr have been studied; with the reported wear mechanism being found to involve the selective removal of the binder phase caused by plastic deformation and fatigue, due to the repeated action of the abrasive particles. This will be followed by pullout of the hard carbide phase due to microcutting. Some instances of wear due to the cracking or crushing of the carbide phase were also observed, caused by fatigue from the repeated slider passage and loading respectively [62,63].

The addition of chromium to the binder phase has been reported to improve the wear resistance of the coating relative to WC-Co HVOF thermal spray coatings. This is because the addition of chromium has been shown to inhibit the decomposition of the WC phase, to avoid the formation of decarburisation phases such as $W_2C$ and metallic tungsten which increase wear. Alongside this, the presence of chromium in the binder phase has

been shown to bind the carbide phase more effectively, increasing the resistance to carbide pullout [79].

In order to have high wear resistance, high hardness and high fracture toughness throughout the coating are required [83]. Using materials with a smaller carbide grain size can lead to increased hardness and fracture toughness, due to the Hall-Petch effect. This is been proven by Thakur and Arora; who investigated the sliding and abrasive wear of WC-Co-Cr coatings with a conventional and nano WC grain size. They determined that the nano WC grain size powder offered a higher level of sliding wear resistance than the larger grain powder. This was attributed to a smaller coefficient of friction, as well as increased coating hardness. The authors also reported that the nano WC grain size coating had lower levels of porosity and a more homogenous structure than the larger WC grain coating (referring to the WC grain distribution); these factors were attributed to increasing abrasive wear resistance [62].

Indentation fracture toughness testing of WC-Co-Cr coatings sprayed by HVOF thermal spraying has been undertaken [84], in order to better understand the mechanisms of erosive wear. The indentation testing showed that the coatings displayed anisotropic crack propagation, and that crack propagation is much easier parallel to the coating/substrate interface, compared to cracks forming transverse to this interface. This is said to be due to the lamellar structure of the coating as well as the residual stresses present. Furthermore, the fracture toughness of the coating was found to

correlate well with the fracture toughness predicted using the equations proposed by Lawn and Fuller and Evans and Wilshaw [85,86].

Research has been undertaken to examine whether HVOF thermal sprayed coatings can offer a similar level of wear resistance to surfaces protected by electroplated hard chrome coatings. The wear resistance of WC-Co-Cr and WC-Co coatings sprayed by HVOF thermal spraying have been compared with conventional hard chrome plating, with the aim of the study being to investigate if these HVOF thermal spray coatings could replace chrome plating. It was determined that the WC-Co and WC-Co-Cr coatings performed better than the chrome plating when tested against Al-Ni-Bz and Cu-Be blocks. This proves that WC-Co-Cr has the potential to replace hard chrome plating in wear resistance applications in the future, provided the geometry of the component to be coated is suitable [87].

## 2.6 WC-Co/NiCrFeSiB HVOF thermal spray coatings for sliding wear resistance applications

Nickel based alloy coatings have been applied in applications where resistance to corrosion, wear and heat is required [88]. In terms of the application of coatings of these alloys, techniques such as plasma spraying, detonation gun, cold spray, plasma transferred arc hardfacing, laser cladding and HVOF have been demonstrated [89–92]. HVOF thermal spraying is considered one of the more promising deposition methods due to its high particle velocity and low flame temperatures in comparison to some other methods [93], as can be seen in Figure 2-6.

NiCrSiB based alloys are known for their self-fluxing properties. The B, Si and Cr decrease the melting point of the pure Ni so better melting can be achieved at lower flame temperatures. Furthermore, the addition of B and Si improve fluxing and wettability during thermal spray deposition and also protect other elements from oxidation by acting as deoxidators. Chromium, boron, silicon and carbon affect the formation of hard phases throughout the nickel matrix[94].

The composition of the NiCrSiB alloy used in coating studies has been shown to vary in the ranges of 10 - 20% Cr, 2 – 5% Si and 1 – 4% B in weight percent, with the balance being Ni [95].Composite coatings of WC-Co/NiCrSiB have been the focus of a number of studies [65,91,96,97]. Adding reinforcing particles has been shown to improve the coating's mechanical properties, such as hardness and Young's modulus [98]. As a result the addition of a reinforcement hard phase has been shown to improve the coating's resistance to sliding wear [97].

### 2.6.1 Coating and Powder Microstructure

Studies in which WC-Co/NiCrSiB coatings have been applied by HVOF thermal spraying are found to vary in the type of powder feedstock used, with some buying commercially available premixed powder feedstocks and others mechanically mixing two separately bought powders together using equipment such as turbo mixers [65,91,99]. NiCrSiB powder feedstocks have been found to possess a spherical morphology with microporosity on the surface, while the WC-Co particles in the mix resemble those typical of

the agglomerated and sintered cermet WC-Co powders described earlier in 2.5.2 [91]. An SEM image showing the morphology of NiCrSiB/WC-Co powder feedstock particles is shown in Figure 2-18.

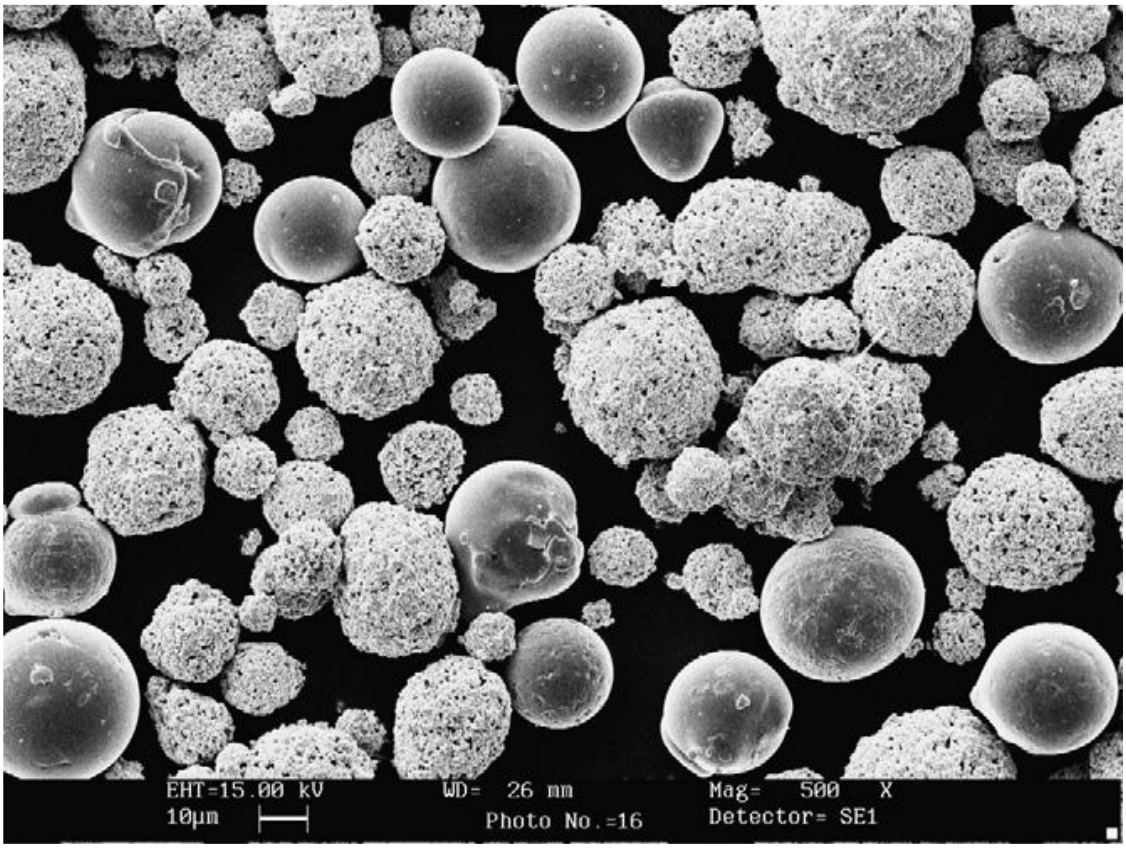


**Figure 2-18 - SEM image showing the morphology of an NiCrSiB/WC-Co powder feedstock [93]**

SEM backscattered electron imaging of the coating cross section has been shown to reveal a microstructure consisting of two distinct phases. Energy dispersive x-ray spectroscopy has determined these to consist of areas of Ni solid solution and cermet material, consisting of WC grains embedded in a Co matrix, with the latter phase appearing brighter due to the greater electron density within this tungsten rich phase [91,97]. With the correct spray parameter optimisation, almost porosity free coatings can be achieved [100].

X-ray diffraction has been used to determine the phases present within the powder feedstock and sprayed coatings. The primary phases found within the powder by were WC, Ni, $Ni_3Si$, CrSi, Co and Cr, shown in Figure 2-19. The only differences were low intensity peaks for $W_2C$ were detected within the coating microstructure confirming some carbon loss occurred during spraying [91,93].

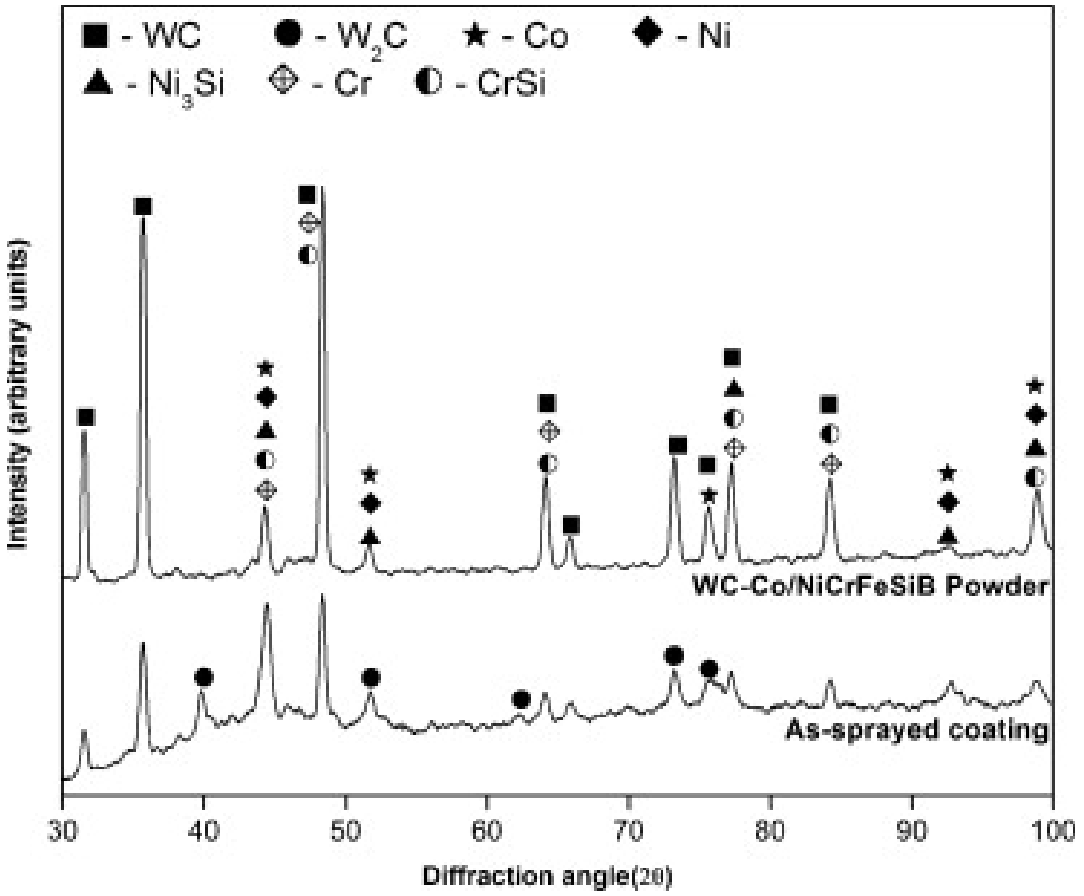


**Figure 2-19 - XRD of NiCrFeSiB/WC-Co powder feedstock and as sprayed coatings [93]**

### 2.6.2 Wear behaviour of HVOF sprayed WC-Co/NiCrSiB coatings

There is little work regarding HVOF thermal sprayed WC-Co/NiCrSiB coatings in the field of wear, with most articles either focusing on coatings

deposited by other means, such as plasma spraying or laser cladding. The main research conducted on the wear behaviour of HVOF thermal sprayed WC-Co/NiCrSiB coatings appears to focus on the erosive wear of the composite coatings with the potential use as a coating to protect pipework from fly ash in fossil fuel power stations. In the two studies found alumina was used as the erodent particle, however the studies differ in the temperature of the wear test, with one being carried out at room temperature, the other at 450 °C [91,93]. The as sprayed coating was found to have an average microhardness of 928 HV0.3 with low porosity by Praveen et al. [91]. The erosion wear test was carried out at 450°C and the main mechanism of wear was determined to be caused by micro-cutting and micro-ploughing leading to the formation of grooves and lips as a result of the impact of the erosive particles in soft binding regions of the coating. These areas were said to act as stress concentrators, leading to further accelerated wear of the coating material. Furthermore small cracks where observed in brittle areas, which could lead to fragmentation of the material and pullout of the cermet hard phase, so the formation of brittle phases such as $W_2C$ and NiO should be avoided if possible for better wear resistance [91]. A similar wear mechanism was observed by Ramesh et al. in a comparable test carried out at room temperature, with the authors concluding coating hardness is a key parameter controlling the coating's resistance to erosive wear [93].

Conciatu et al. investigated the influence of the composition of the composite feedstock powder on the sliding wear resistance of the coating.

Coatings of NiSiCrSiB with 0%, 10%, 20% and 30% WC-Co were sprayed by HVOF and a sliding wear test was carried out at a 10N load against a WC-Co ball. Microhardness of the coating was found to not change significantly as harder phase was added; however, the resistance to sliding wear improved as the composition of reinforcing phase was increased. The coefficient of friction μ was monitored throughout the length of the test; following the initial break in period it was seen to decrease from about 0.75 to 0.65 in the test against pure NiSiCrSiB. For the 10 – 20% WC-Co samples, μ was found to remain constant following the break in period and at 30 % additional WC-Co, μ increased slightly after the break in period from about 0.7 to 0.75. It was hypothesised that these changes were due to the topography and the formation of a tribofilm of the worn surface. Details on the actual mechanism of sliding wear in this system are not documented [97].

## 2.7 Gaps in the literature

From this literature review, it is clear that overall, the application of WC-Co-Cr coatings by HVOF thermal spray is a well understood and researched topic. For the development of an ID-HVOF thermal spray process, further work on comparing the effect of particle size may be required as there are no available studies directly comparing the effect of particle size on the microstructure, mechanical properties and sliding wear performance of the sprayed coatings. It is clear that using fine particle feedstocks may be an advantage for ID-thermal spray applications, however their use comes with

other possible issues such as decreased deposition efficiencies and greater decarburisation rates.

HVOF thermal spraying of WC-Co/NiCrFeSiB is a much less researched material, however studies which assess the microstructure, phase composition and erosive wear rates have been carried out. Work assessing the sliding wear rate of this material with changing WC-Co composition was found; however, details of wear mechanisms were not provided meaning there is no available data in this regard. No work has been currently carried out regarding the application of WC-Co/NiCrFeSiB coatings by an ID-thermal spray process.

What is much less well known is the adaptation of the HVOF thermal spray process to apply WC-Co-Cr or NiCrFeSiB/WC-Co coatings on internal surfaces. As described in Section 2.4, only one available study was found in which WC-Co-Cr coatings were sprayed by ID-HVOF thermal spraying on internally mounted substrates. A fixed stand-off distance was used, meaning no data is accessible regarding the effects of spraying at very low stand-off distances to simulate coating parts with smaller internal diameters. Low magnification SEM images are provided, alongside microhardness measurements but a phase composition analysis and sliding wear testing were not carried out.

# Chapter 3. Experimental Procedures

## 3.1 Thermal spray method

Due to the challenges of applying coatings onto internal surfaces previously explored in the last chapter, the design of the ID-HVOF thermal spray torch must differ from others to be effective. In particular, the length of the nozzle is required to be much shorter than older thermal spray systems to enable the system to fit into tight areas to apply coatings onto internal surfaces. The ID-HVOF thermal spray system utilised in this work was developed by Castolin-Eutectic Monitor Coatings Ltd [40]. It uses a mixture of oxygen, air and fuel gas for combustion, with the hot gases passing through an isentropic conical plug in order to accelerate them to supersonic velocities. A fuel rich mixture of gaseous fuels and oxidisers is used to produce a single annular exhaust extending around a centrally located aerospike meaning a high degree of particle heating can take place without the use of a long nozzle therefore reducing the size of the torch. The powder feedstock is radially injected downstream of the combustion chamber, which means the powder feedstock is not exposed to the high temperatures found within the combustion chamber but is instead heated by the hot gases.

This spray system was used throughout the work conducted within this thesis to deposit coatings in the two different environments of ID thermal spray and conventional thermal spray setups.

The thermal spray coatings studied in Chapter 4 and Chapter 6 were sprayed with the samples set up in a conventional "external" spray configuration. The substrates were first cleaned and grit blasted with brown alumina grit to provide a roughened surface on which to spray the coating to improve the coating to substrate bonding. The substrates were mounted on the outer circumference of a rotating carousel and were cooled using compressed air jets throughout and after the spray run. A schematic of this experimental setup shown in Figure 3-1**.** The spray parameters and stand-off distance used in each chapter will be described in each respective chapter.

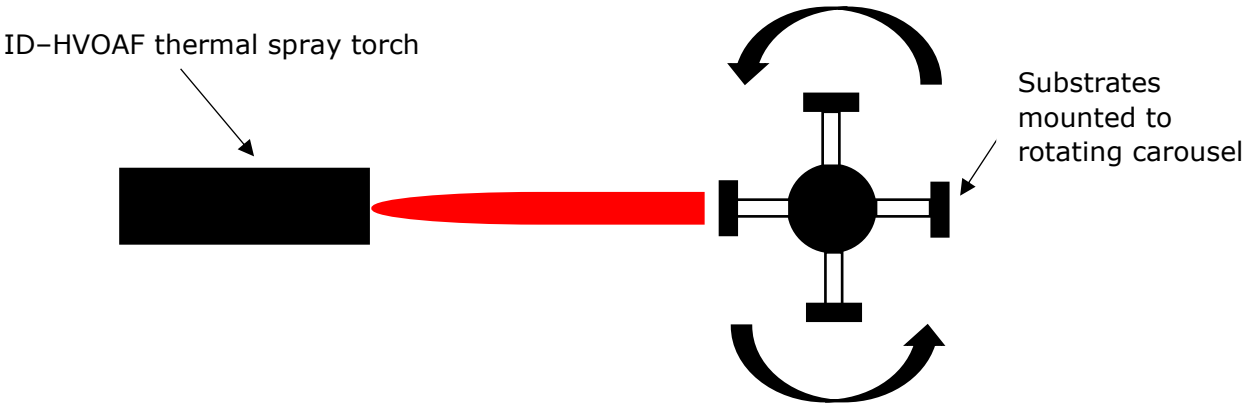


**Figure 3-1 - Illustration showing the thermal spray setup (not to scale)**

For the ID thermal spray trials carried out in Chapter 5, the coatings were sprayed using the ID-HVOF thermal spray system onto discs of 416 stainless steel (12- 14% Cr, 1.25% Mn, 0.15% C, 0.15% S, 0.6% Mo, 0.06% P, 1% Si in weight%) with dimensions of 38.1mm diameter and 6mm thickness. These discs were mounted using magnets on the inside of 3 cylindrical tubes with internal diameters of 70mm, 90mm and 110mm

and an axial length of 200mm; a photograph of the setup shown in Figure 3-2. This corresponds to approximate stand-off distances of 30mm, 50mm and 70mm respectively, meaning the effects of spraying at very small stand-off distances can be investigated.

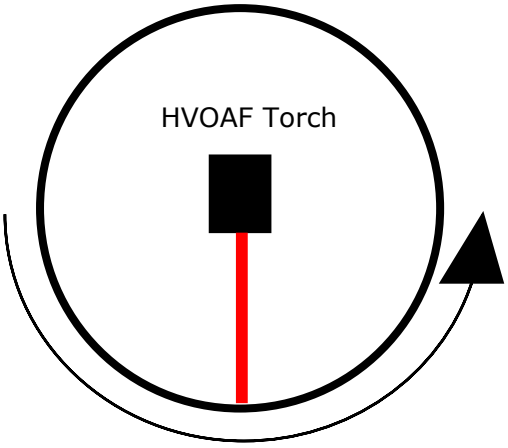


**Figure 3-2 - Photograph and plan view schematic of ID coating deposition setup (drawing not to scale). The torch was fixed in x and y directions and the pipe holding the substrates rotated during deposition.**

The spray torch was positioned inside the cylindrical tube during spraying and moved vertically at 2mm/s as the substrate was rotated around it. The RPM at which the part was rotated was kept constant for each spray run. Air was also blown into the cylinder during spraying to assist cooling and the removal of undeposited loose particles.

## 3.2 Powder and coating characterisation

### 3.2.1 Particle size distribution

To measure the particle size distribution of the dry powder feedstocks used in this study, two separate laser diffraction particle sizers were used: Malvern Mastersizer (Malvern Instruments, UK) and Coulter LS230. (Beckman Coulter Life Sciences, USA). Powder particles pass through a laser beam, which leads to scattering of the light at an angle that is directly correlated to the particle diameter. From the angle and intensity of the scattered light, the diameter of individual particles is determined, with larger particles scattering light at narrow angles with high intensity and smaller ones producing high angle, low intensity scattering. Annular detectors measure the angle and intensity of the scattering to provide an energy distribution and applying Mie scattering theory, this can be computed to produce a particle size analysis based on equivalent spherical diameter [101]. As this method only holds true if the particle size is significantly larger than the incident wavelength, a helium-neon light source with a wavelength of 632.8nm was used, leading to a detection limit

of a 1μm equivalent spherical diameter. For each powder 3 measurements were taken, with the mean size distribution presented.

### 3.2.2 X-Ray diffraction (XRD)

In X-Ray diffraction, a beam of X-rays strikes a sample surface and is constructively diffracted at an angle that is related to the interplanar distance of crystals within the sample according to Bragg's law:

$$n\lambda = 2d \sin\theta$$

Where n is an integer, λ is the wavelength of the incident X-ray beam, d is the interplanar distance and θ is the angle between the incident ray and scattering plane. From collecting a scan of the intensity of the signal at different values of θ, a spectrum can be obtained from which the crystal structure of the sample can be analysed.

A Siemens D500 (Siemens, Germany) X-Ray diffraction instrument was used for all measurements within this study, utilising Cu K α radiation (λ = 1.5406Å) as its wavelength is comparable to the interplanar spacing in crystalline materials measured in this study. A step scan that paused when taking measurements was used in order to reduce signal noise. The diffractometer was run at 40kV and 25mA; step sizes and dwell times differed slightly throughout the study and therefore will be specifically detailed in further chapters.

EVA software (Bruker, USA) was used to process the spectra and characterise the measured peaks to identify the phases present, using

JCPDS diffraction data. Powder samples were prepared by sprinkling powder directly into the holder, whereas scans of coated samples were performed on the top surface of unpolished, as sprayed samples. All coated samples were cleaned with acetone prior to testing to prevent contamination.

### 3.2.3 Scanning Electron Microscopy (SEM)

Scanning electron microscopy is a technique that involves scanning a focused electron beam across the surface of a sample. The interaction of the incident electron beam impacting with the sample produces secondary electrons, backscattered electrons and Auger electrons and a number of detectors within the sample chamber can measure these signals. Secondary electrons are produced by the incident beam knocking electrons around atoms of the sample out of orbit and can only escape from a layer of material close to the sample surface. These signals provide high spatial resolution images of the sample topography. Backscattered electrons are electrons from the incident beam that have entered the sample surface and have been diffracted at a high angle from passing sufficiently close to the nucleus of at atom. These can re-emerge from the sample surface if they have sufficient energy and can be detected to provide compositional information as elements of higher atomic mass show higher contrast [102]. A schematic of the interaction volume produced from the electron beam-sample interaction is shown in Figure 3-3.

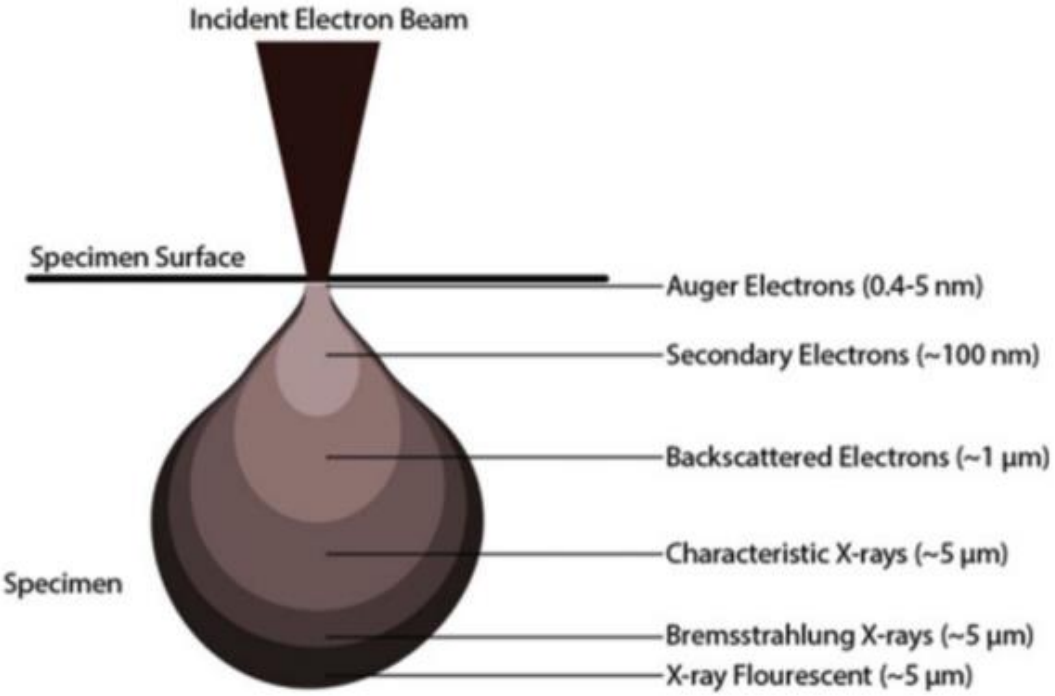


**Figure 3-3 - Schematic illustration showing the interaction volume produced from the scattering of the electron beam within the sample [103]**

The morphology and cross section of the feedstock powders used in this study were imaged using a Jeol 6490LV scanning electron microscope (Jeol Ltd, Japan) operated at 20kV.

To image the powder feedstock, the sample material was sprinkled onto an adhesive carbon tab attached to an aluminium stub. Powder cross sections were prepared by mounting particles in a conductive mounting material which was then grinded using SiC papers (240, 400, 800, 1200 grit sizes) followed by polishing down to a 1µm diamond finish.

Cross sections of the sprayed coatings were imaged using SEM throughout this work, utilising secondary (SE) and backscattered (BSE) electron imaging modes. Samples were prepared by sectioning with a precision cutting machine, using a SiC cutting disk. The movement speed of the

cutting disc was set between 0.010–0.015mm/s to prevent any delamination of the coating. The samples were mounted within a conductive mounting compound (MetPrep Ltd, UK), then ground and polished in a similar method as described above. Prior to imaging, the mounted coating cross sections were cleaned with detergent and IMS to remove any surface contamination.

### 3.2.4 Porosity measurements

The porosity of the sprayed coatings was estimated using a thresholding method with an image analysis program (Image J) [104]. Secondary electron SEM images were used to provide the necessary images of the sample surface. A contrast was selected for each image in which any pores appear black, while the coating material is brighter. With this knowledge, the software can remove pixels from the image that do not have this darkest black colour and then calculate the percentage coverage of the remaining black pixels. A magnification was chosen for each coating that provided a view of most of the coating vertical thickness, without the surface or coating/substrate interface showing. As the thickness of each coating differed, this magnification was changed for each sample. For each porosity reading 5 separate SEM secondary electron images each in different locations directly horizontal from each other were analysed, with the mean value and standard error presented.

## 3.3 Mechanical properties testing

### 3.3.1 Microhardness

The microhardness of coatings sprayed in this study was evaluated by carrying out indentation hardness measurements. In these tests the amount of plastic flow of material following indentation is analysed by indenting a material using an indenter tip with known geometry and load. The area of the produced indent is then measured, with softer materials producing larger indents under a given load. In this study a Vickers indenter was used, which incorporates a diamond shaped tip with a 136° angle; an illustration of this indenter tip is displayed in Figure 3-4.

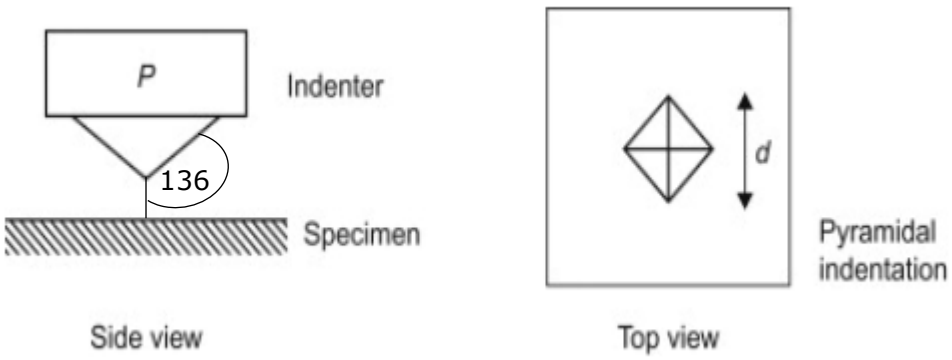


**Figure 3-4 - Schematic of Vickers indenter tip used for indentation tests adapted from [140]**

As the geometry and dimensions of the indenter tip is known alongside the indentation load, the microhardness of the material being tested can be calculated:

$$HV = \frac{2P\,sin\left(\frac{136}{2}\right)}{d^2}$$

Where HV is Vickers hardness, P is indentation load in grams and d is the length of the diameter in mm [105].

Vickers microhardness was measured on polished coating cross sections using a Buehler microhardness tester (Buehler, USA). For each sample, 6 indents were produced parallel to the coating/ substrate interface using a load of 0.3kgf with a dwell time of 10s. The mean value of these measurements is displayed, alongside the standard deviation between the values used as the displayed error. Indents that were found to contain cracks in or around them were discarded and repeated to attempt to reduce the error within the readings.

### 3.3.2 Fracture Toughness

The fracture toughness of a material is a quantitative method of determining a material's resistance to brittle fracture when a crack is present. Fracture toughness was measured using the indentation method. Polished coating cross sections were indented using a macro hardness indenter in order to induce cracks at the edge of the indents as presented

in Figure 3-5 using a load of 2.5kgf and a dwell time of 10 seconds. The lengths a and c were measured using optical microscopy.

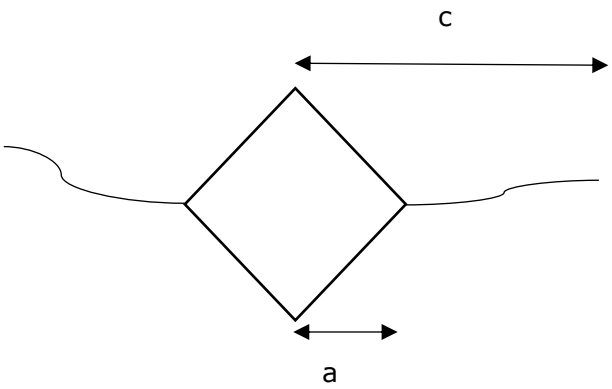


**Figure 3-5 - Measuring fracture toughness from an indentation using the method by Evans and Wilshaw**

The measured parameters were then substituted into the below equation for determining the indent fracture toughness developed by Evans and Wilshaw [86].

$$K_{Ic} = 0.079\left(\frac{P}{a^{3/2}}\right) log\left(\frac{4.5a}{c}\right)$$

Where $K_{IC}$ is fracture toughness (MPa.$m^{0.5}$), P is indentation load (N), a is length of the indentation half diagonal (m) and c is the crack length from the indent centre (m). In order for measurements to be valid, the criteria $0.6 \leq c/a \leq 4.5$ must be met; all measurements of $c$ and $a$ were determined to fit within this range for all samples measured. In fact, for all samples the c/a ratio was determined to be less than 2.5, indicating a Palmqvist crack system. This is consistent with other studies with WC-Co based cermets [106,107]. However, the indents were not polished down to confirm for certain whether the crack systems were Palmqvist or median in nature.

### 3.3.3 Elastic Modulus

Elastic modulus of the internally sprayed samples was measuring by using nanoindentation. A Berkovich tip was chosen, with an initial load of 0.02mN and a loading/unloading rate of 0.15mN/s used. The depth of each indent was set to 200nm, with a 10s dwell time at maximum load. 30 indentations were measured on each sample, arranged approximately 50μm apart in 3 rows each containing 10 indents. The method developed by Oliver and Pharr [108] was used to determine the reduced elastic modulus. The elastic modulus, independent of the response of the indenter tip was calculated:

$$\boldsymbol{E = \frac{(1 - v^2)}{\frac{1}{E_R} - \frac{(1 - v_i^2)}{E_i}}}$$

Where E is elastic modulus (GPa), $E_R$ is reduced modulus (GPa) of the coating, $E_i$ is the elastic modulus of the indenter tip, v is the Poisson ratio of the coating and $v_i$ is the poisson ratio of the indenter.

The poisson ratios of the coating v and indenter tip $v_i$ were assumed to equal 0.3 and 0.07 respectively and the elastic modulus of the Berkovich tip $E_i$ was assumed to be 1140GPa, based on values used in other relevant studies [69].

## 3.4 Dry Sliding Wear Testing

### 3.4.1 Sliding wear testing

For sliding wear testing of the as sprayed coatings at a load of 10N, unlubricated testing was carried out using a rotary ball-on-disc microtribometer (Ducom, Bengaluru, India). This instrument is capable of directly measuring the frictional force produced from the sliding contact between the sample being tested and the counterbody, meaning real time coefficient of friction measurements are possible. The maximum load supported by this instrument is 60N, meaning a different instrument was needed for testing at higher loads.

The high load sliding wear tests on the coated materials were performed on a rotating ball-on-disc style tribometer, shown in Figure 3-6.

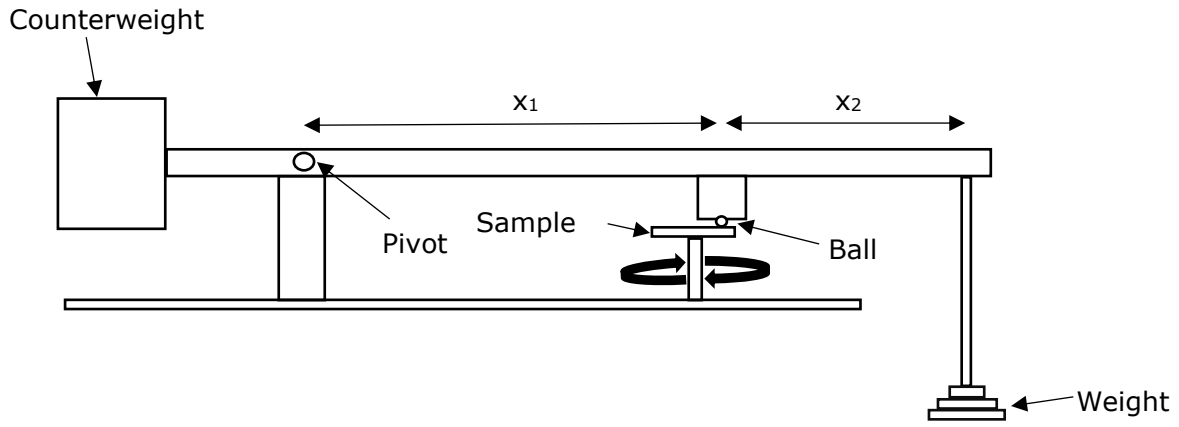


**Figure 3-6 - Schematic of the ball on disc tribometer used in this study**

The load was varied between 96N, 168N and 240N to investigate the effect of increased load on the wear rate and mechanism of wear taking place. Testing was carried out without lubrication at room temperature for a

distance of 500m with a sliding speed of 0.05m/s. After each test a new counterbody ball was used and each coated sample was degreased with methylated spirit prior to starting the test. During each run the friction coefficient was monitored using a linearly variable differential transformer (LVDT) connected to a data logger. From running a calibration comparing known loads to the outputted voltage the friction coefficient could be computed; to provide this data a calibration test was performed prior to running the actual wear test, in which weights were incrementally added to the hanger with the voltage measured from the LDVT being logged.

To relate the mass of weights on the hanger to the normal force exerted on the sample by the counterbody, the following expression was used:

$$\boldsymbol{x_2 N = F(x_1 + x_2)}$$

Where N is the force (kg) on the sample, F is the weight place on the hanger (kg) and $x_1$ and $x_2$ are the perpendicular distances (m) from the pivot to the ball, and ball to the centre of mass of the hanger respectively.

### 3.4.2 Calculation of volume loss of coatings and counterbody

The volume loss of the worn coatings was measured using the profilometry method used in other studies [52]. A contact surface profilometer (Taylor Hobson Ltd, UK) was used; this method involves a probe being dragged along the sample surface, with the changes in the surface height along the probes path measured. This is achieved mechanically by a feedstock loop that records the force from the sample pushing up against the probe as it

moves across the sample surface. A feedback system is used to keep the arm with a set amount of torque applied on it, known as the setpoint. Thus, the changes in the height of the arm holder can therefore be used to reconstruct the surface topography.

For each sample, 4 line traces perpendicular to the direction of the counterbody movement were measured. From this information, the cross sectional area of the material removed within the wear track could be determined in 4 different locations. The mean area from these 4 measurements was then multiplied by the circumference of the scar to give an estimate of the volume of material removed. A length of 3mm was used for the measurement length for each separate reading to ensure the profiler tip passed along the entire width of the wear track. Prior to each set of readings, the surface profilometer was calibrated using the set calibration blocks and provided by Taylor Hobson Ltd.

The wear of the counterbody ball has been shown to result in a nearly flat circular cap being formed. Therefore assuming that this represents the removal of a spherical cap of material, the following process can be followed to determine the volume of counterbody material removed: the radius of the circular scar was measured using optical microscopy and was then substituted into the following expressions [109]:

$$\boldsymbol{d = r - \sqrt{(r^2 - a^2)}}$$

$$\boldsymbol{V = \pi d^2 \left( r - \frac{d}{3} \right)}$$

Where d is the depth of wear scar (mm), R is the ball radius (mm), a is the radius of wear scar (mm) and V is the volume loss of counterbody ($mm^3$).

## 3.5 Investigation of worn surfaces

### 3.5.1 Scanning electron microscopy

Plan view and cross-sectional images of the wear scars on the coated samples were analysed using a Jeol 6490 LV SEM. EDX was employed to analyse the elemental composition of different phases present. For plan view images, the discs were mounted atop an aluminium stub using adhesive carbon tape to fix the sample. To prepare the cross section samples, the samples were sectioned across the wear track using a precision cutting machine. These were then mounted in a resin based mount, as mounting in a similar fashion to other samples using the conductive mounting compound was found to stress the sample and cause coating delamination. In order to ensure the samples were conductive therefore, gold coating was used.

### 3.5.2 Raman spectroscopy

Raman spectroscopy is a method of identifying structural information within a material by illuminating the sample with a source of monochromatic light; this interacts with molecules and can lead to Raman scattering. This is the inelastic scattering of photons, which results in the energy of laser photons being shifted either up or down. The Raman scattered light is detected using a spectrograph [110]. This method has an advantage of being able to focus the laser on a particular small area of a sample, meaning gaining structural

information on areas of sample in the order of size of micrometres. In this study, this method was used to gain information on the composition of phases found on the worn surfaces of the as-sprayed coatings.

Raman spectroscopy was carried out using a LabRAM HR spectrometer (Horiba jobin YVON, Japan) modified by the addition of an automated xyz stage (Märzhäuser, Germany). The instrument was calibrated using a standard Si (100) reference band at 520.7cm$^{-1}$ and the Rayleigh line at 0cm$^{-1}$. A laser with a wavelength of 659.41nm with a 300μm pinhole was utilised with a 10% laser filter used to prevent damaging the sample. The individual spectra were collected for 20s and were repeated 3 times to improve the signal to noise ratio. Following data correction, the spectra were corrected by applying linear baseline subtraction in order to remove effects of fluorescence.

# Chapter 4. WC-Co-Cr powder selection for HVOF deposition on internal surfaces for wear resistance applications

## 4.1 Introduction

The additional challenges brought on by the short stand-off distances and reduced spray torch dimensions required for ID-HVOF processes may require the use of finer particle feedstocks to achieve optimum coating properties. At a given flame power and HVOF thermal spray torch, smaller particles may reach higher in-flight velocities due to their lower mass but may not necessarily be deposited due to inertia and bow shock effects. Assuming comparable morphologies, the increased surface area to volume ratio of smaller powder particles may lead to more efficient heat transfer between the hot gases and the in-flight material in comparison to larger powders (Section 2.4).

There are other factors that must be considered when selecting WC-Co-Cr powder feedstocks for HVOF thermal spraying of coatings for wear resistance applications, including composition and WC grain size. The composition of 86 % WC, 10% Co and 4% Cr (mass %) was established as the most widely used, with all relevant HVOF thermal spray studies making use of this composition (Section 2.5.2). For this reason, alongside the wide commercial availability of 86%WC - 10%Co - 4%Cr powders, this composition was used for all WC-Co-Cr coatings sprayed throughout this chapter and beyond.

WC-Co-Cr HVOF thermal spray coatings that perform well in applications where a high resistance to sliding and abrasive wear is required must possess a high microhardness and fracture toughness (Section 2.5.5). The literature review determined that using nanostructured powders with a much smaller WC grain size was one method that can possibly improve the mechanical properties of the coatings; however a greater amount of decarburisation of the WC phase may occur when spraying these nanostructured powders (Section 2.5.3).

In this chapter, the effect of WC grain size and particle size range on the properties and wear behaviour of WC-Co-Cr coatings sprayed by an ID-HVOF thermal spray system will be investigated.

## 4.2 Materials

The three WC-Co-Cr powders were provided by H.C Starck Ltd (Munich, Germany), with details of each of the powders studied displayed in Table 4-1. The MC-30 and MC-15 powders are stated by the manufacturer to have a medium WC grain size but differ in powder particle size range. The third feedstock powder NC-30 has a nanoscale WC grain size, therefore meaning that the effect of WC grain size and powder particle size range on the coating microstructure, mechanical properties and wear resistance can be compared. All feedstock powders were deposited on to discs of EN 1.4401 grade 316 stainless steel (16% Cr, 10% Ni and 2% Mo in wt.%) with a diameter of 38.1mm and a thickness of 6mm using the ID-HVOF thermal spray system.

| Commercial Designation | Powder No. | Method of manufacture | Particle size range stated by manufacturer (µm) | WC grain size stated by manufacturer | Average WC grain size (µm) |
|---|---|---|---|---|---|
| AMPERIT 557.059 | MC-30 | Agglomerated and sintered | -30+5 | Medium | 1.47±0.40 |
| AMPERIT 554.067 | MC-15 | Sintered and crushed | -15+5 | Medium | 1.26±0.14 |
| AMPERIT 507.059 | NC-30 | Agglomerated and sintered | -30+5 | Nanometric | 0.32±0.05 |

**Table 4-1 - Details of the powder feedstocks studied within this chapter**

## 4.3 Spray Parameters

The spray parameters used in this study were kept constant between each powder type, with the air flowrate fixed between 60–500 SLPM and oxygen flowrate between 50–170 SLPM, aiming for 100% stoichiometric combustion. The stand-off distance was set to 120mm. The exact parameters were unable to be disclosed due to confidentiality agreements. Prior to coating deposition, all coating materials were grit blasted using alumina grit followed by cleaning with acetone in order to improve coating/substrate bonding.

## 4.4 Feedstock characterisation

Secondary electron (SE) and backscattered electron (BSE) SEM images of the MC-30 feedstock powder are presented in Figure 4-1. This powder was received with a nominal size distribution of -30+5µm and was manufactured by the agglomerating and sintering method. The powder can

be observed to have a roughly spherical shape, with holes visible showing a hollow core for some particles. The WC phase is represented by the phase with the brightest contrast in the BSE SEM image, with the WC grains shown to possess a "block-like" shape. These are embedded in the binder phase, visible as the areas with a darker contrast in BSE.

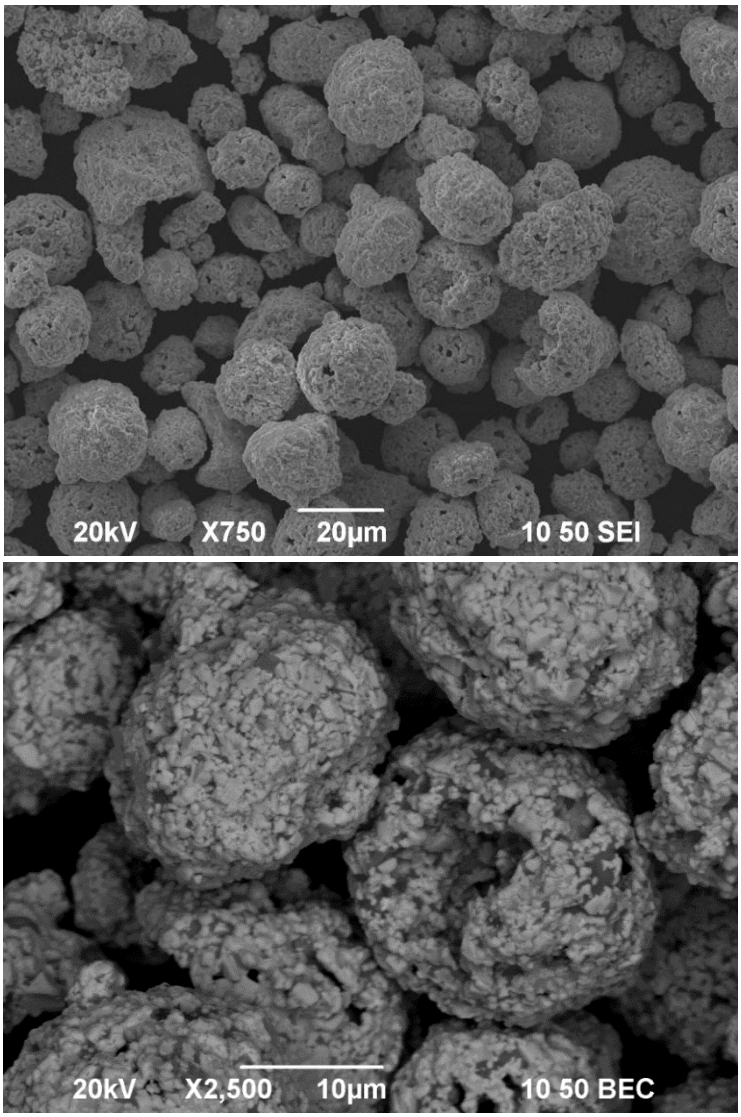


**Figure 4-1 – SE (top) and BSE (bottom) SEM images of the MC-30 powder feedstock**

SE and BSE SEM images of the polished cross section of the MC-30 powder feedstock are displayed in Figure 4-2. From the cross section the inner

porosity present within the particles can be clearly observed. BSE images reveal areas of the binder phase with varying contrast, indicating possible differences in composition throughout the binder.

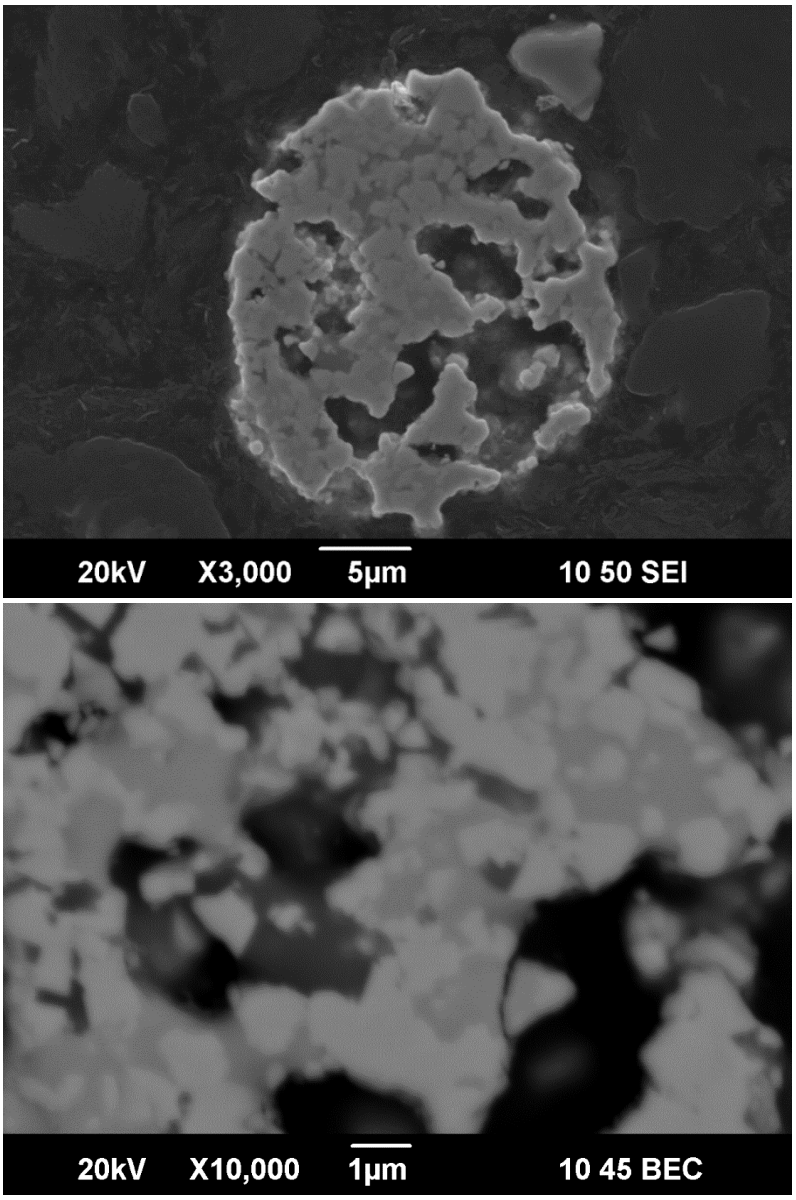


**Figure 4-2 - SE (top) and BSE (bottom) SEM images of the polished cross section of the MC-30 powder feedstock**

Secondary electron (SE) and backscattered electron (BSE) SEM images of the MC-15 feedstock powder are shown in Figure 4-3**.** This powder has a

nominal size distribution of -15+5μm and was manufactured by the sintering and crushing method The particles can be observed to have an irregular shape, unlike the near spherical shape of the MC-30 powder; this difference is likely due to the different method of manufacture used. The powder particles appear to be very dense, with no inner porosity visible in both Figure 4-3 and in images of the MC-15 cross sectional shown in Figure 4-4. The size of the WC grains in this powder are stated by the manufacturer to be in the same range as those found on the MC-30 powder; measurements confirmed that this claim is accurate, with the size of the WC grains visible on the MC-30 and MC-15 powders measured at approximately 1.47±0.40μm and 1.26±0.14μm respectively.

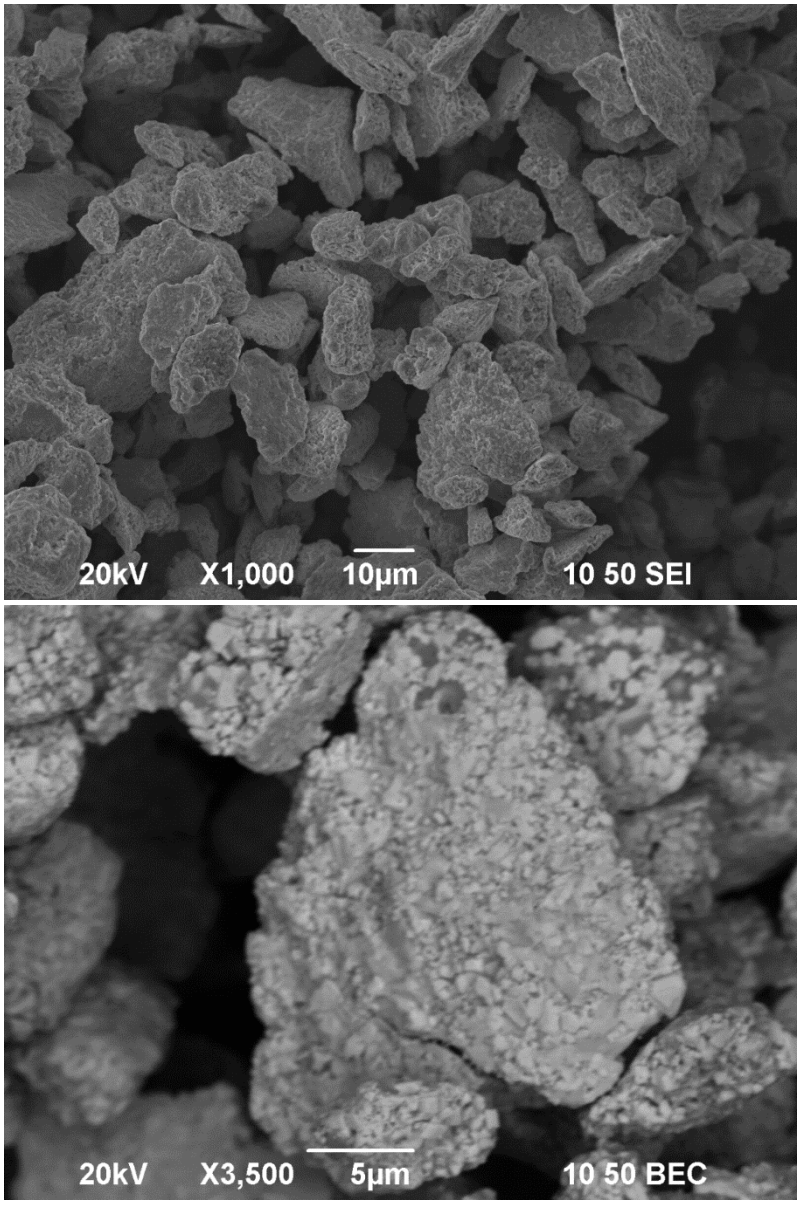


**Figure 4-3 - SE (top) and BSE (bottom) SEM images of the MC-15 powder feedstock**

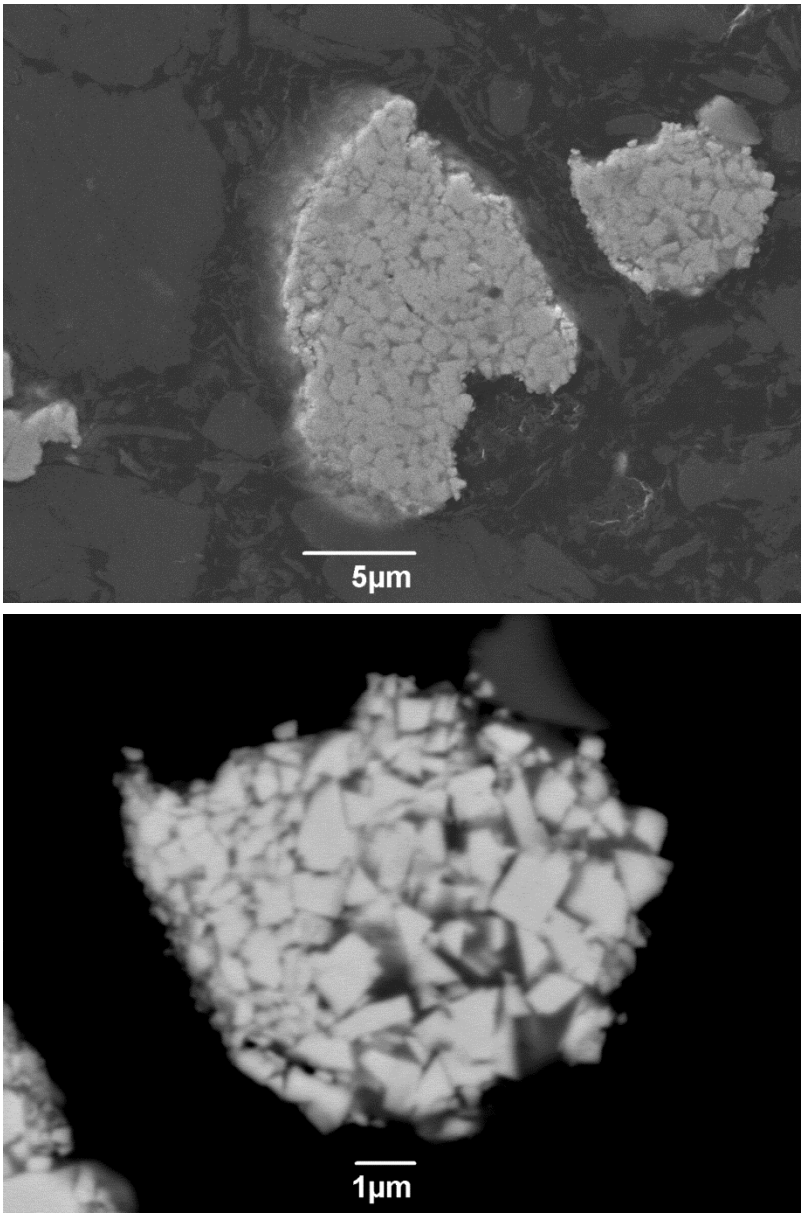


**Figure 4-4 - SE (top) and BSE (bottom) SEM images of the polished cross section of the MC-15 powder feedstock**

Secondary electron (SE) and backscattered electron (BSE) SEM images of the NC-30 feedstock powder are shown in Figure 4-5. The nominal size distribution of the powder feedstock is stated as being the same as the MC-30 powder at -30+5µm and it was produced using the agglomerating and sintering method. The particles can be observed to have an almost spherical morphology like that of the MC-30 powder, which is expected due to both

powders sharing the same method of manufacture. The WC grain size of this powder feedstock is stated by the manufacturer as having a nanometric grain size. This was confirmed with the mean grain size being found at 0.32±0.05 μm, therefore significantly smaller than the WC grain size of the other two powder feedstocks. SEM images of the polished powder cross section reveal small regions of inner porosity. Unlike the MC-30 particles however in which individual particles are observed to be largely hollow, the inner porosity of the NC-30 particles consists of much smaller unconnected pores. This can be seen in the SEM images of the powder cross section in Figure 4-6.

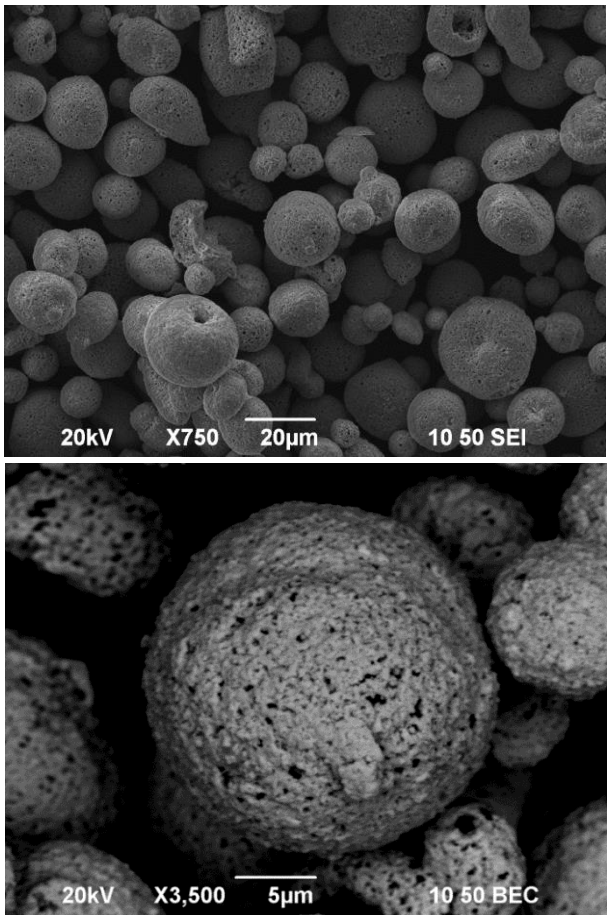


**Figure 4-5 - SE (top) and BSE (bottom) SEM images of the NC-30 powder feedstock**

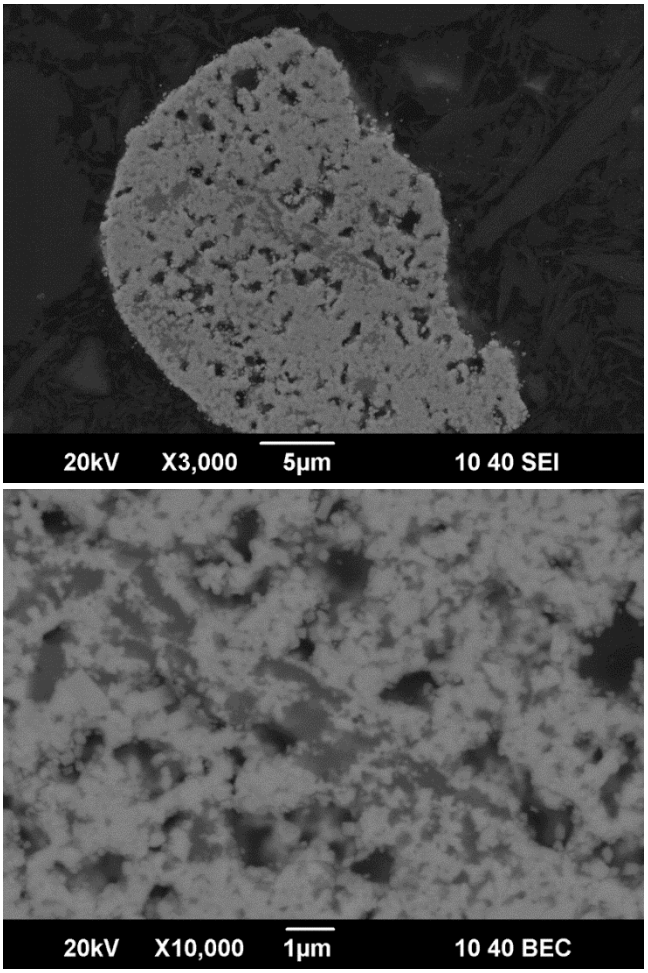


**Figure 4-6 - SE (top) and BSE (bottom) SEM images of the polished cross section of the NC-30 powder feedstock**

XRD diffractograms measured from the three powder types are shown in Figure 4-7. The phase content of the two powders with the stated medium WC grain size, MC-30 and MC-15 were both found to have a similar phase content. Aside from the primary WC phase these powders were found to content amounts of η-phase carbide $Co_6W_6C$ and a cubic Co phase. Similar WC-Co-Cr powders used for thermal spraying have also been shown to contain η-phase carbides and cubic Co, including recent work [70,71].

Differences can be observed for the nanostructured NC-30 powder feedstock, with no η-phase carbide detected within this powder. Traces of

elemental W (cubic) were detected, with a characteristic peak at 2θ=38.37°, alongside traces of $Cr_3C_2$.

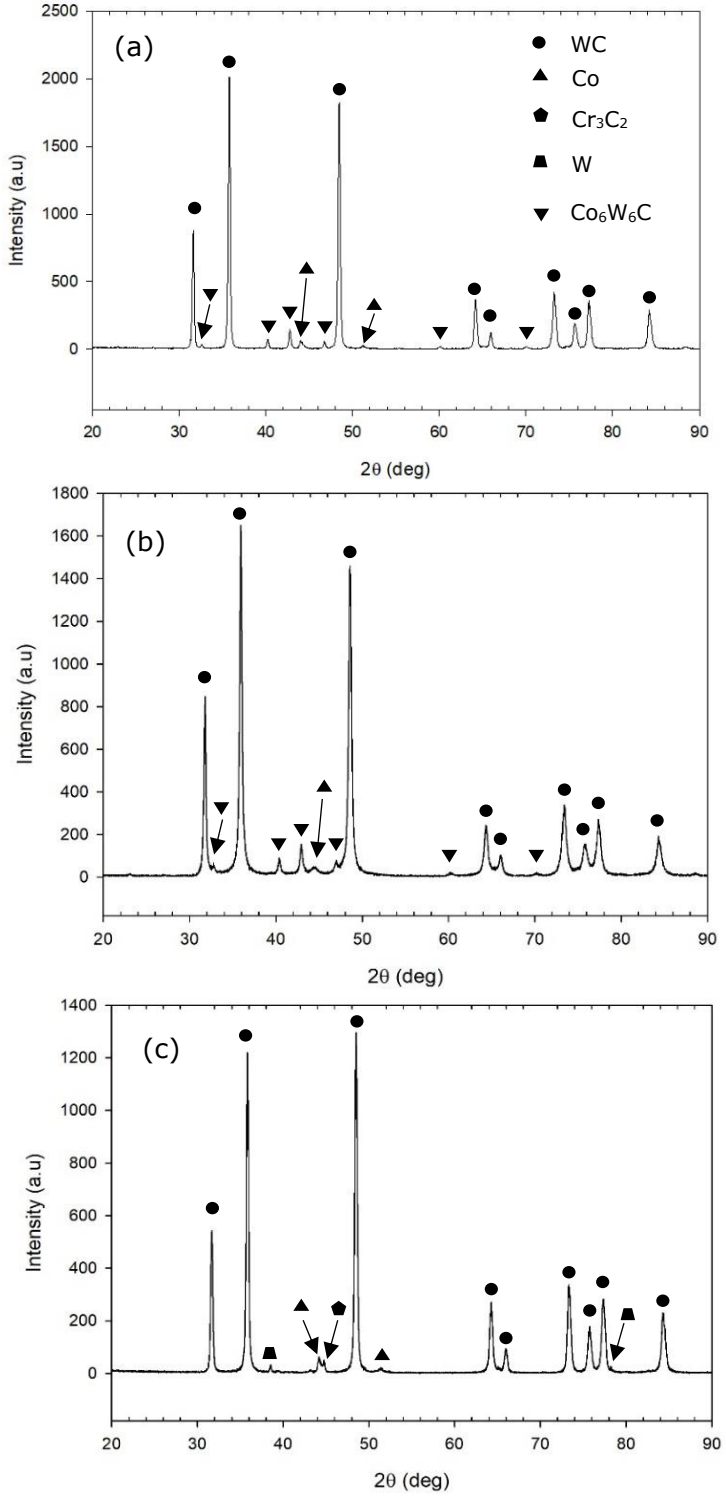


**Figure 4-7 - XRD diffractograms of powder feedstocks (a) MC-30 (b) MC-15 (c) NC-30**

## 4.5 Coating characterisation

The XRD diffractograms of the coatings are displayed in Figure 4-8. All three coatings were found to contain varying amounts of $W_2C$, indicating that a degree of decarburisation occurred during spraying in all cases. This is particularly apparent by noting the large peaks positioned at 2θ≈40°, which corresponds to the (101) peak of $W_2C$. The intensity of this peak relative to others measured within each scan was found to be the largest for the MC-15 coating. The $Co_6W_6C$ and cubic Co phases that were detected within the MC-30 and MC-15 powders can be no longer be clearly defined in the coatings. For the NC-30 coating, phases found in the powder such as elemental W and $Cr_3C_2$ can no longer be detected. A single broad peak can be seen for all three coatings in the region 41°<2θ<49° indicative of the formation of amorphous material during the spray process, agreeing with previous work discussed in Section 2.5.2.

To assess the extent of the decarburisation taking place, the index of carbon retention was calculated for each coating using the following expression:

$$\boldsymbol{ICR} = \frac{\boldsymbol{I_{WC}}}{\boldsymbol{I_{WC} + I_{W2C}}}$$

Where $I_{WC}$ is the intensity of the (100) peak of WC at 2θ=35.6° and $I_{W2C}$ is the (101) peak of $W_2C$ at 2θ=39.6°.

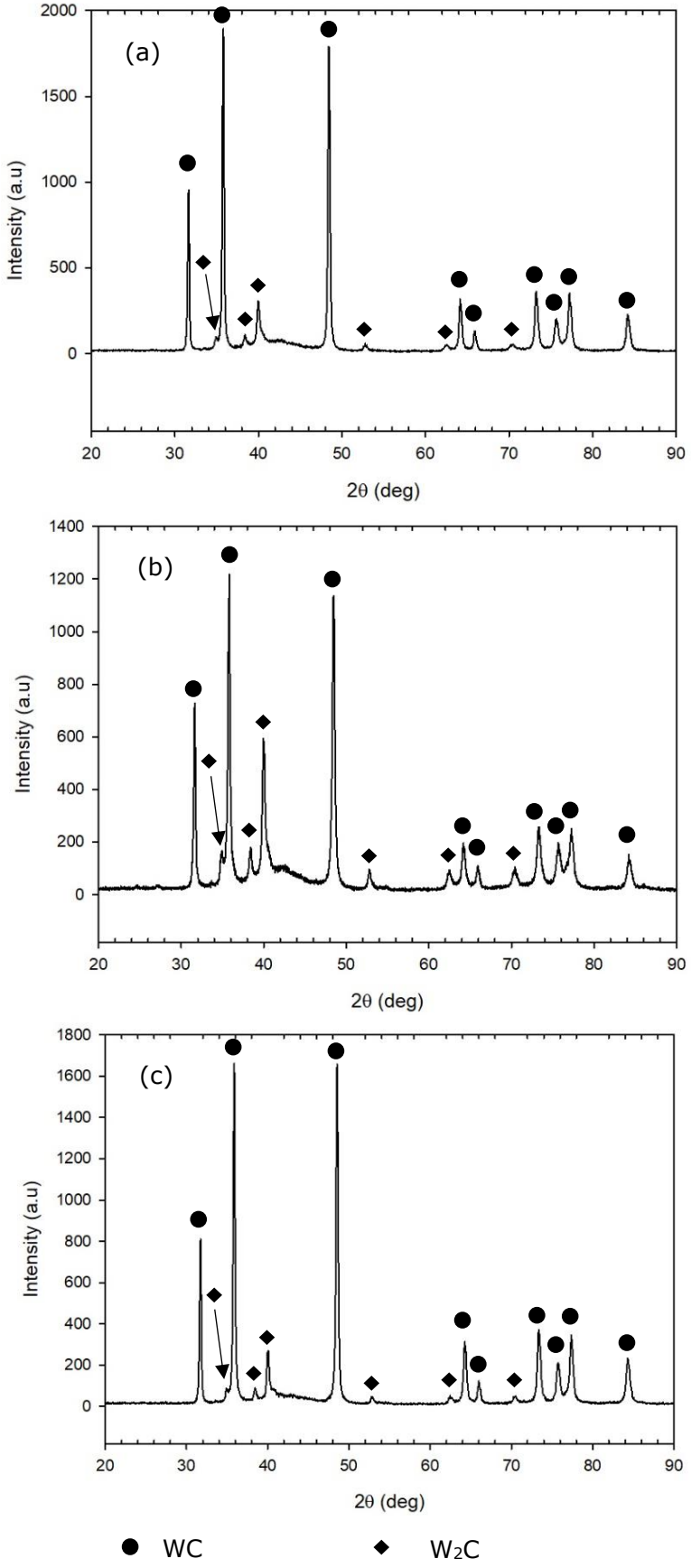


**Figure 4-8 - XRD diffractograms for the as sprayed coatings**

The ICR for each coating is displayed in Table 4-2 with the most decarburisation occurring in the finer MC-15 powder with an ICR equal to 0.67. The index of carbon retention was found to be very similar for both the MC-30 and NC-30 coatings.

| Coating | Coating Thickness (µm) | Porosity (%) | Index of carbon retention (ICR) |
|---|---|---|---|
| MC-30 | 317 | 0.5±0.2 | 0.86 |
| MC-15 | 512 | 0.3±0.1 | 0.67 |
| NC-30 | 290 | 0.3±0.1 | 0.85 |

**Table 4-2 - Thickness, porosity and index of carbon retention of the three as sprayed coatings**

Low magnification SE SEM images of the three coatings are displayed in Figure 4-9. No large cracks or delamination from the substrate was observed in any of the coating; all coatings can be seen to possess dense structures that are well bonded to the substrate. It can be observed that the thickness of the NC-30 coating is higher than that of the other two, possibly indicating a higher deposition efficiency. All coatings were found to have low levels of porosity at <1%, with the data presented in Table 4-2. The MC-30 coating was found to have the highest measured porosity at 0.53±0.24 % and MC-15 the lowest with 0.27±0.11%, with the NC-30 coating in between at 0.34±0.15%. Overall, when taking the margin of error into account, all three coatings likely contain similar levels of porosity.

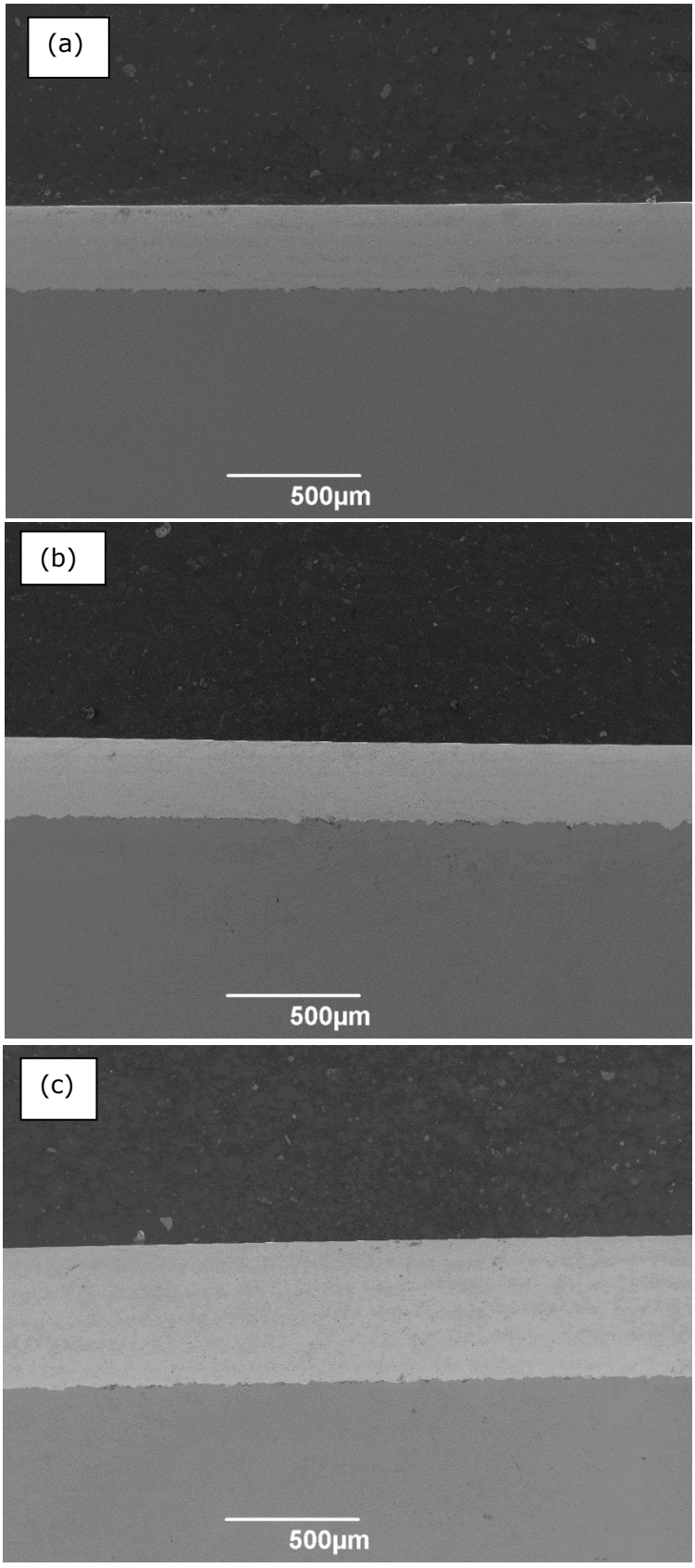


**Figure 4-9 - Low magnification SE SEM images of the cross section of the three coatings. (a) MC-30 (b) MC-15 (c) NC-30**

A higher magnification BSE SEM image of the MC-30 coating is displayed in Figure 4-10.

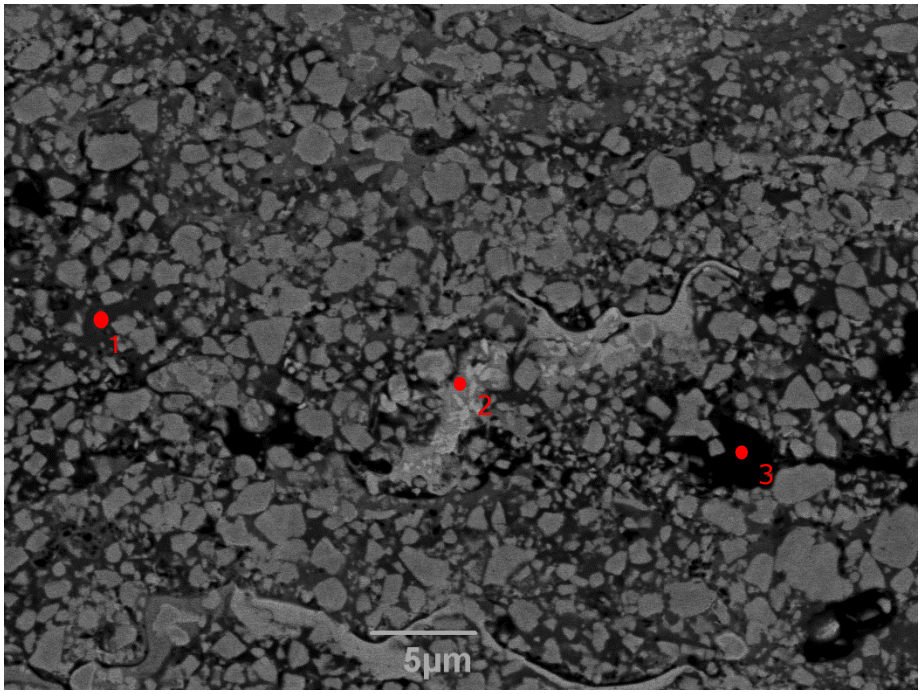


**Figure 4-10 –High magnification BSE SEM image of the MC-30 coating cross section. The positions in which EDX point scans were taken are marked on the images with red dots**

The binder phase can be seen to give off a range of different contrasts in BSE, indicating different phase compositions throughout. WC grains with a brighter phase around their perimeter can be seen in certain areas, embedded in a binder phase with a brighter contrast than other areas of the binder. This has been previously shown to indicate that decarburisation mechanisms have taken place, with the bright phase around the perimeter of the WC grains found to be $W_2C$, as discussed earlier in Section 2.5.1. Alongside these areas, splats with a thin string-like structure can be seen. An area of the binder phase with no grains of WC with a black contrast in BSE can also be seen, indicating matter with a much lower atomic number

is found in this area. In order to investigate the contrast differences throughout the binder phase, EDX points scans were carried out in the positions marked by red dots on Figure 4-10, with the results presented in Table 4-3. It can be observed that the contrast of the binder phase directly correlates with the weight percentage of W measured, with the darkest areas containing little W (point 3) and the brightest being mostly W rich (point 2). Furthermore, Cr rich areas of the binder appear to exist within this coating, with the dark area measured (point 3) having a weight percentage of approximately 47 % Cr.

| EDX Point No. | C (wt.%) | Cr (wt.%) | Co (wt.%) | W (wt.%) |
|---|---|---|---|---|
| **1** | 12 | 7 | 26 | 55 |
| **2** | 14 | 5 | 15 | 66 |
| **3** | 17 | 47 | 26 | 10 |

**Table 4-3 - EDX measurements for the MC-30 coating**

A higher magnification BSE SEM image of the MC-15 coating is displayed in Figure 4-11. Many WC grains, more than that observed in the MC-30 coating can be seen to be surrounded by a layer of material exhibiting a brighter contrast, with the surrounding binder in these areas also having a brighter contrast in a similar manner to that described above. This coating was determined by XRD to have the lowest Index of Carbon Retention (ICR), meaning the most decarburisation took place when spraying this powder feedstock; therefore, seeing the highest presence of features characteristic of decarburisation in this coating is expected. Much darker patches of the binder can again be seen throughout the microstructure,

with EDX scans again confirming these areas are Cr rich in a similar manner to that shown for the MC-30 coating. Splats with the thin string like shape can also again be observed throughout the microstructure of this coating.

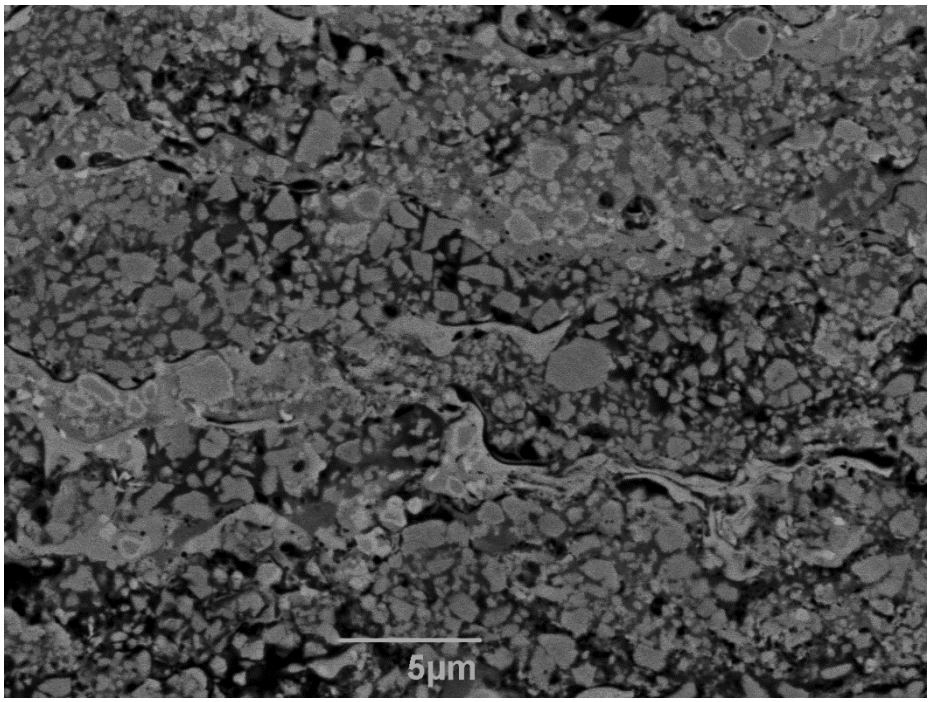


**Figure 4-11 -High magnification BSE SEM image of the MC-15 coating cross section**

A higher magnification BSE SEM image of the NC-30 coating is displayed in Figure 4-12. The smaller size of the WC grains can clearly be seen throughout the microstructure. Like the other two coatings areas exhibiting a brighter contrast can be observed, accompanied in some areas by the splats with a thin string like shape. In some of these areas, grains of WC can no longer been seen, which is likely due to them being dissolved fully into the surrounding binder phase during spraying. The presence of the dark areas, previously shown to be Cr rich can be seen throughout the coating, but to a lesser degree in comparison to the MC-30 and MC-15 coatings.

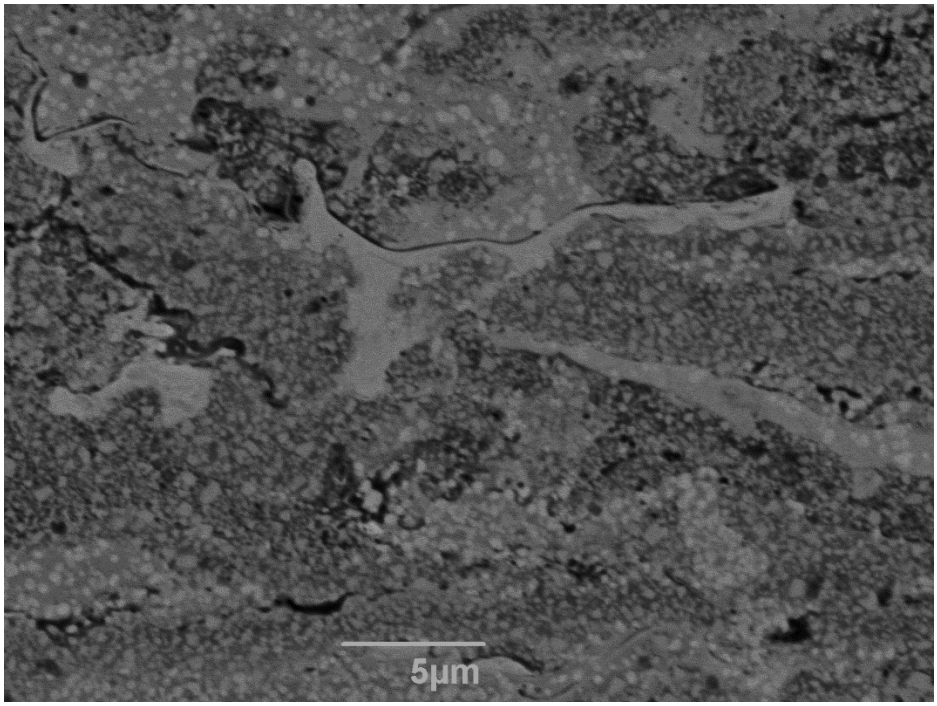


**Figure 4-12 – High magnification BSE SEM image of the NC-30 coating cross section**

The measured microhardness and indentation fracture toughness for the three coatings is presented in Table 4-4.

| Coating Name | Microhardness (HV0.3) | Indentation Fracture Toughness $K_{IC}$ ($MPa.m^{0.5}$) |
|---|---|---|
| MC-30 | 1313 ± 60 | 4.0 ± 0.4 |
| MC-15 | 1341 ± 43 | 3.9 ± 0.5 |
| NC-30 | 1246 ± 58 | 3.6 ± 0.7 |

**Table 4-4 - Microhardness and indentation fracture toughness of the three coatings**

The MC-15 coating was found to be the hardest coating at 1341±43, followed by MC-30 and then NC-30 with a microhardness of 1313±60 and 1246±58 respectively. Not only did the nanostructured NC-30 coating have

the lowest microhardness of the three coatings tested, it also was found to have the lowest indentation fracture toughness at 3.62±0.65MPa.$m^{0.5}$ meaning this coating had the worst mechanical properties overall. The MC-30 coating was found to have the highest toughness of all coatings tested at 4.00±0.36MPa.$m^{0.5}$.

## 4.6 Sliding wear testing

To assess the sliding wear resistance of the coatings under different loads, sliding wear tests were carried out using the setup described as high load testing in Section 3.4.1 at loads of 96N, 168N and 240N. The sliding wear tests were conducted against a sintered 94% WC - 6% Co ball with a diameter of 9.5mm (Dejay Ltd, Launceston, UK), with the remaining parameters provided in Section 3.4.1, chosen to simulate typical conditions for components in the aerospace industry that experience sliding wear.

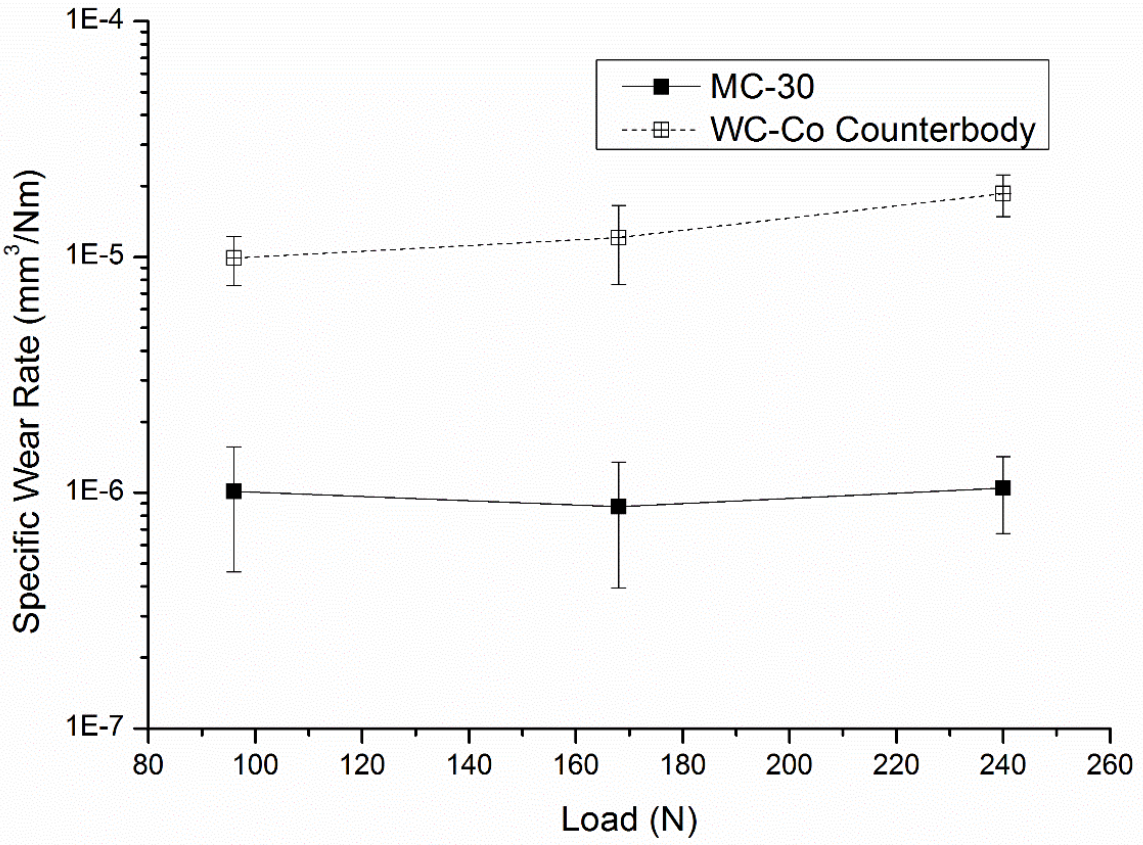


**Figure 4-13 - Specific wear rates of the MC-30 coating and respective counterbody**

The specific wear rates of the MC-30 coating and corresponding WC-Co counterbody are presented in Figure 4-13. The specific wear rate of the coating can be seen remain similar at all three different loads, with only the specific wear rate of the counterbody increasing. This could suggest that the same mechanism of wear is taking place at all loads. Similar specific wear rates were measured for the MC-15 coating presented in Figure 4-14, at 96N and 240N although an increase was seen at 168N. At this load however, the total wear within the system was balanced by an increase in

counterbody wear. A decrease in specific wear rate was measured when the load was raised from 168N to 240N, accompanied by a sharp increase in counterbody wear.

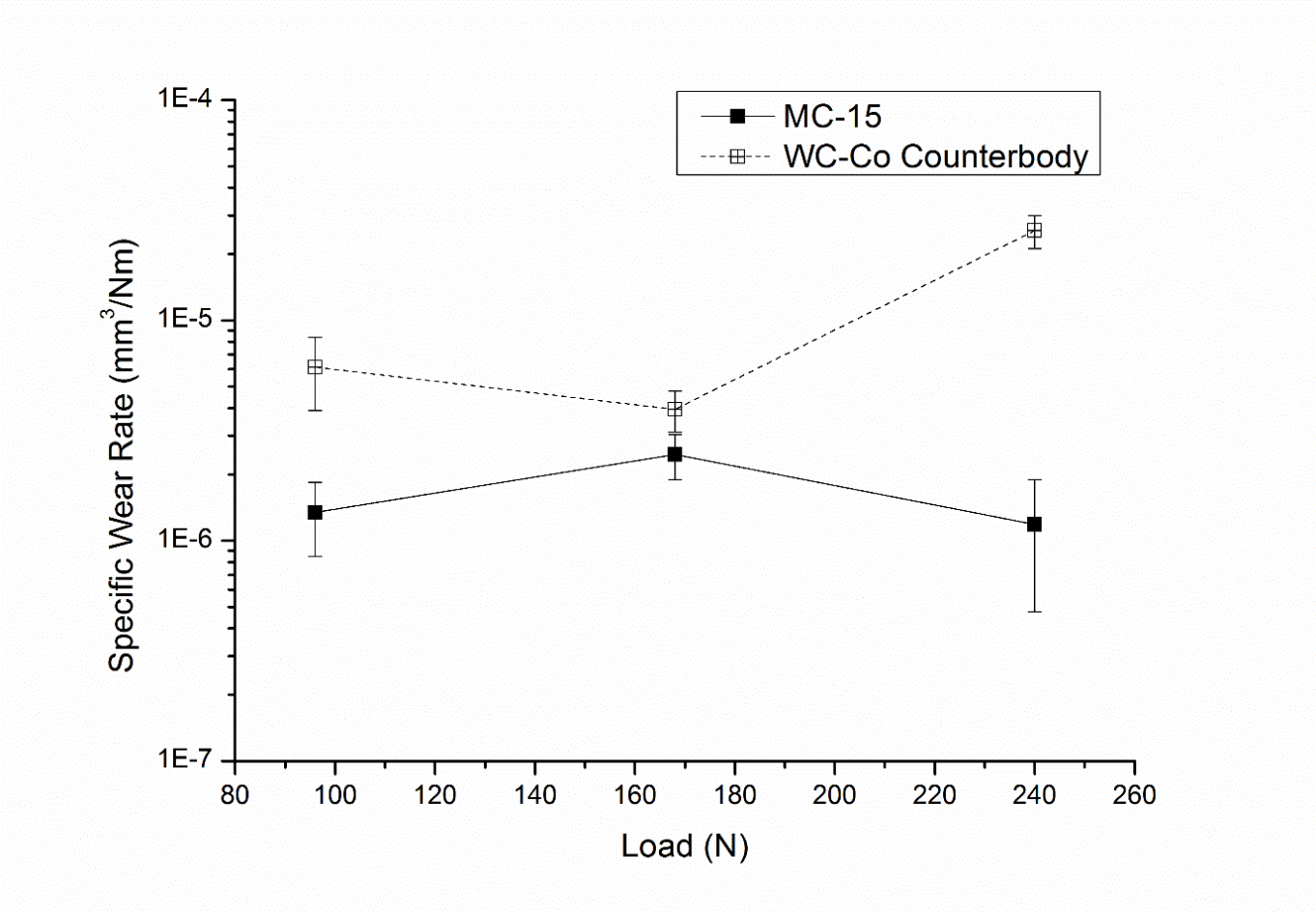


**Figure 4-14 - Specific wear rates of the MC-15 coating and respective counterbody**

The specific wear rates measured for the NC-30 coating across the three loads was found to follow a different trend compared to the other two coatings, displayed in Figure 4-15. For the NC-30 coating and its associated counterbody, the specific wear rate was found to increase as load was increased. Furthermore, at 96N the specific wear rate was found to be almost an order of magnitude lower than the other two coatings. However, the increased load resulted in specific wear rates at 240N that are the

highest out of all coatings tested. This could suggest either that a different wear mechanism is taking place for the nanostructured coating, or that its inferior microhardness and fracture toughness in comparison to the other coatings tested within this study results in this coating suffering greater wear at the highest load of 240N. The fracture toughness of the NC-30 coating is lower than that seen in another study on a nanostructured WC-Co-Cr coating [111].

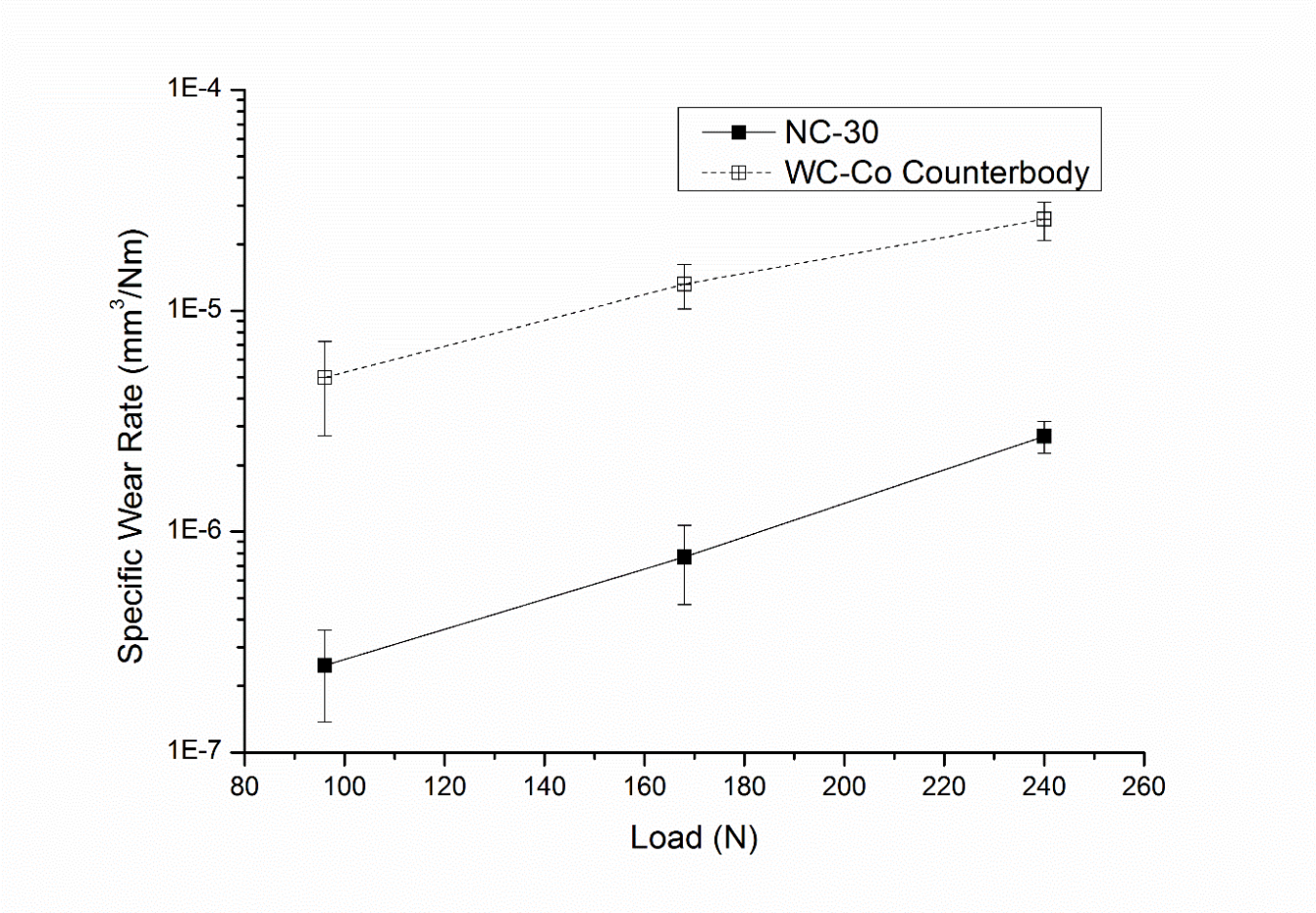


**Figure 4-15 - Specific wear rates of the NC-30 coating and respective counterbody**

## 4.7 Examination of worn surfaces

To gain further insight on the mechanisms of wear taking place in the three coatings, the worn coating surfaces were examined using SEM imaging.

Secondary electron SEM images of the worn surfaces of the coatings tested at the 96N load are displayed in Figure 4-16. The presence of another phase can be observed on the worn surfaces of the MC-30 and MC-15 coatings, in which cracks can be seen at higher magnifications. BSE SEM imaging reveals this phase has a darker contrast, as seen in Figure 4-17, indicating a lower atomic number than the bulk coating material. An EDX point scan on this brittle, darker phase reveals that this phase consists primarily of tungsten and oxygen, suggesting these phases are oxidised particles. They could have formed due to the work done on the coating surface by the counterbody being converted to heat energy, resulting in the occurrence of tribo-oxidation processes.

The brittle oxide phase however was not observed on the worn surface of the NC-30 coating at 96N, perhaps explaining the lower specific wear rate of this coating at this load. Instead on the worn surface of the NC-30 coating, scratches can be seen running parallel to the direction of the movement of the counterbody. These scratches seen on the worn surface may have formed from a three body abrasion mechanism, in which loose material originating from the coating gets trapped between the coating and counterbody, resulting in ploughing of the coating taking place as discussed in Section 2.1.2. Material can be seen breaking off the coating surface in

Figure 4-18, alongside areas in which fine cracks can be observed. These cracks indicate brittle fracture may be occurring in this coating, resulting in debris being released from the worn surface. This is likely due to compressive stresses being generated in front of the counterbody as it slides over the coating, leading to cracks forming perpendicular to the direction of the movement of the counterbody. Over time, these cracks will meet and result in sections of material breaking off the coating surface.

When the load was raised to 168N (Figure 4-19), the oxidised particles can now be seen on all three coatings, particularly on the worn surface of the MC-15 coating. This coating was found to have the highest specific wear rate at this load, suggesting the high amount of oxidised material may be linked to the high wear rate. Scratches can be observed on the worn surfaces of the MC-30 and NC-30 coatings, indicating that abrasion is again occurring with a similar mechanism to that described previously.

At the highest load of 240N, the oxidised particles can again be seen on all three coatings, as seen in Figure 4-20. It can be observed that the width of the wear track on the NC-30 is much wider than that on the other two coatings.

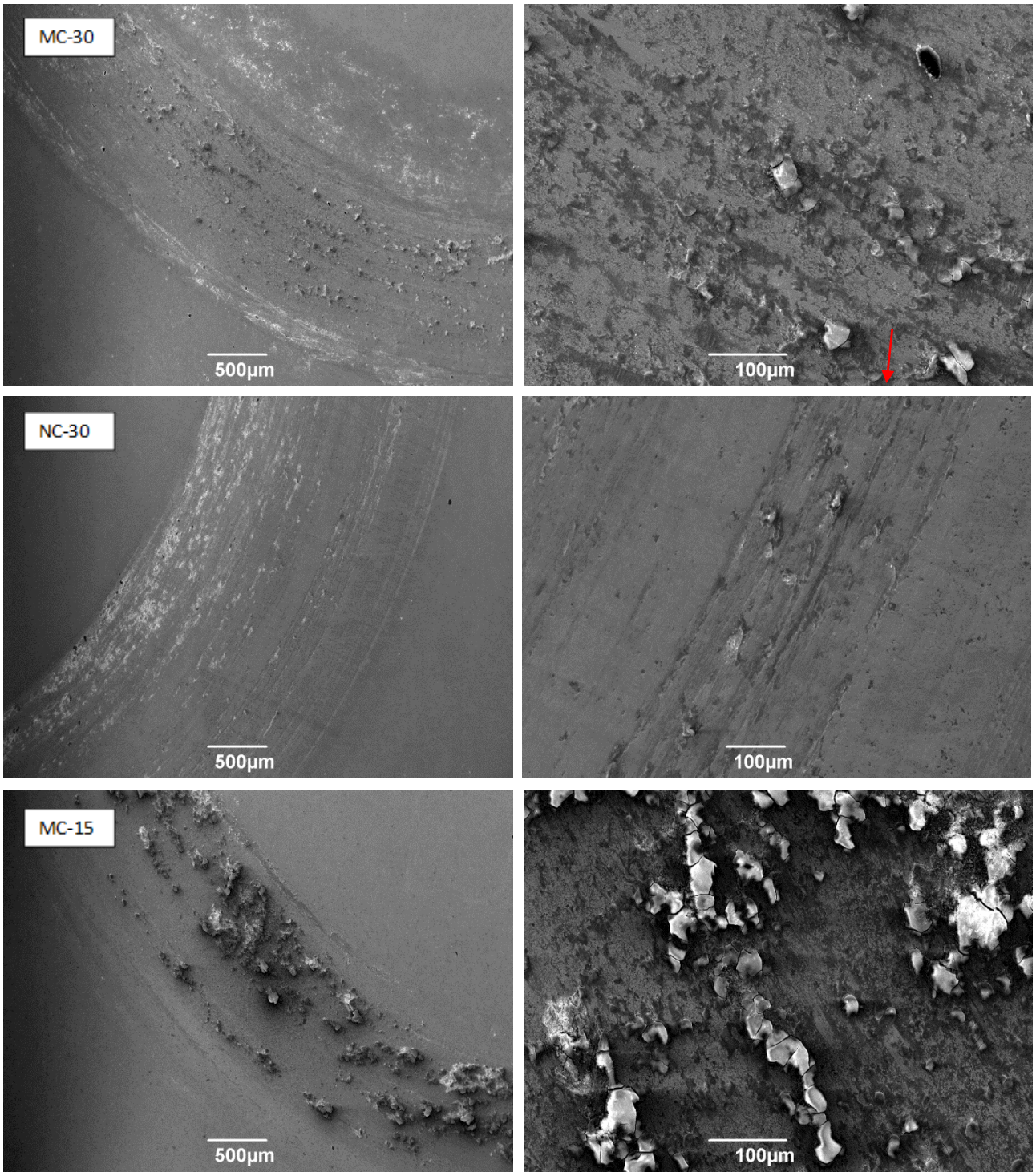


**Figure 4-16 - Left: Lower magnification SE SEM images showing the plan view of the worn surfaces of the three coatings at 96N. Right: Higher magnification top down SE images of the worn surfaces. A brittle phase can be observed on the coating surfaces, most notably on the MC-30 and MC-15 coatings and is marked on the images**

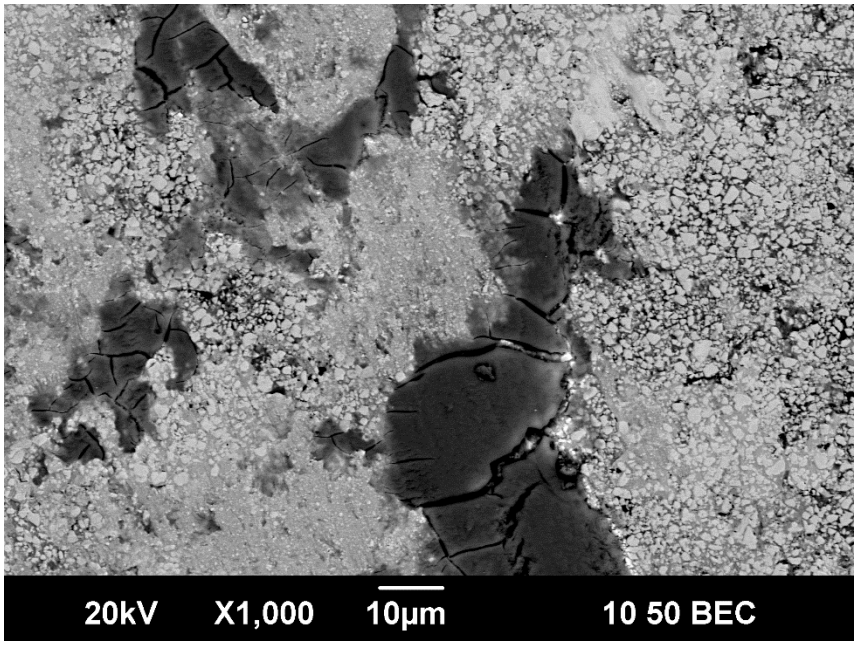


**Figure 4-17 - BSE SEM image showing contrast difference between the bulk coating surface and the observed brittle phase on the worn surface of the MC-30 coating**

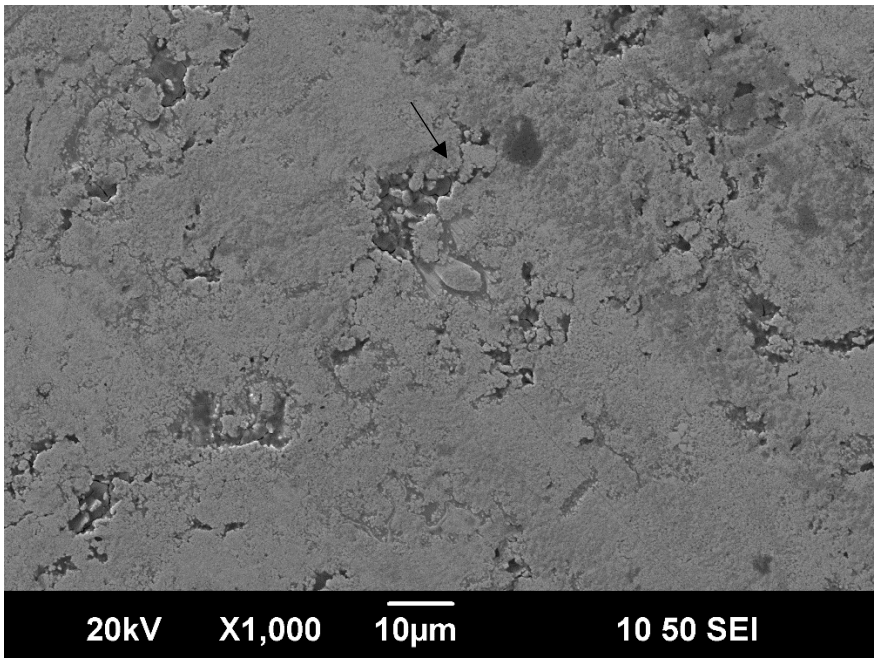


**Figure 4-18 - SE SEM image of the worn surface of the NC-30 coating tested at 96N. Areas in which coating material can be seen breaking off are marked with an arrow**

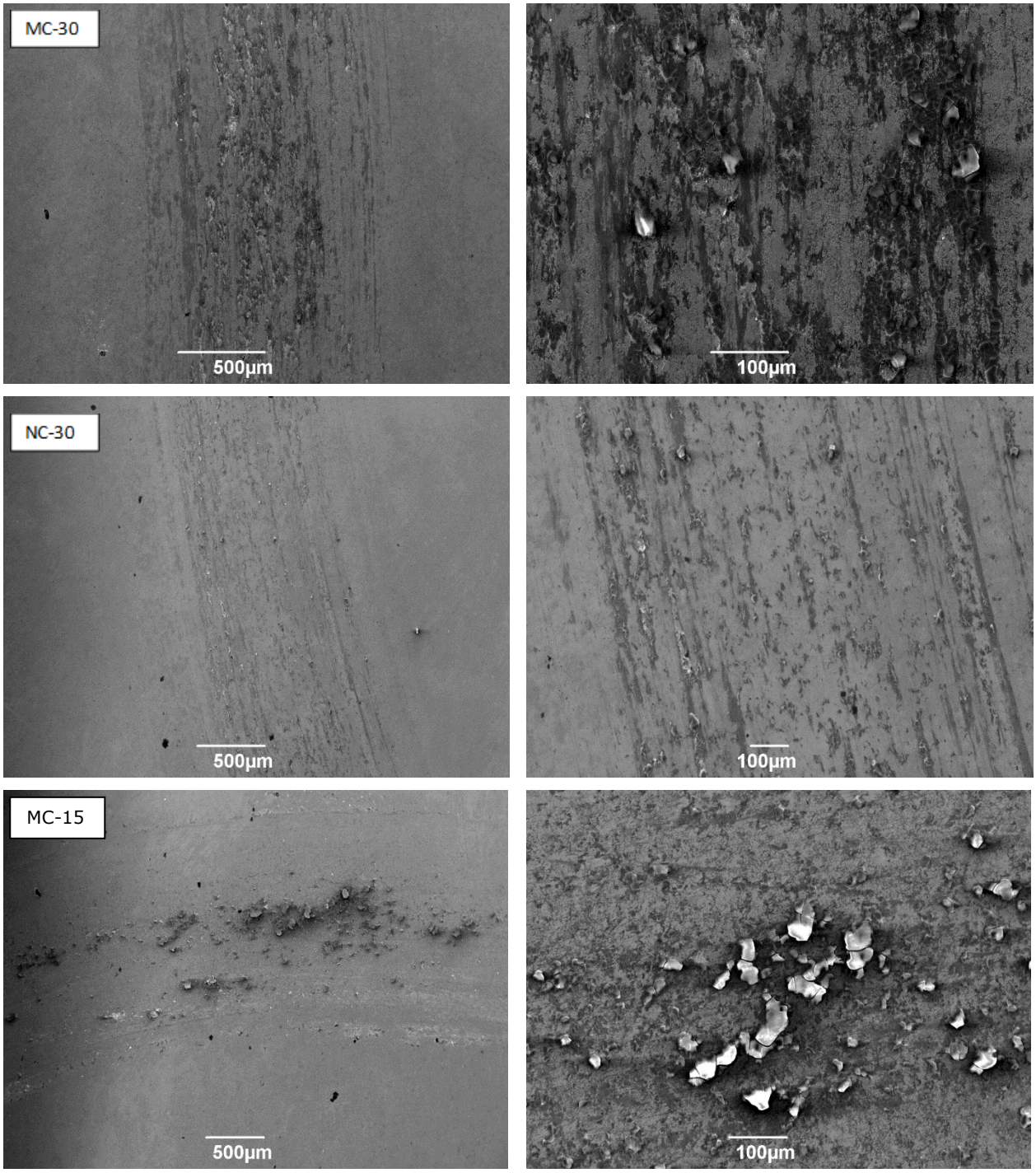


**Figure 4-19 - Left: Lower magnification SE SEM images of the plan view of the worn surfaces of the three coatings at 168N. Right: Higher magnification top down SE images of the worn surfaces**

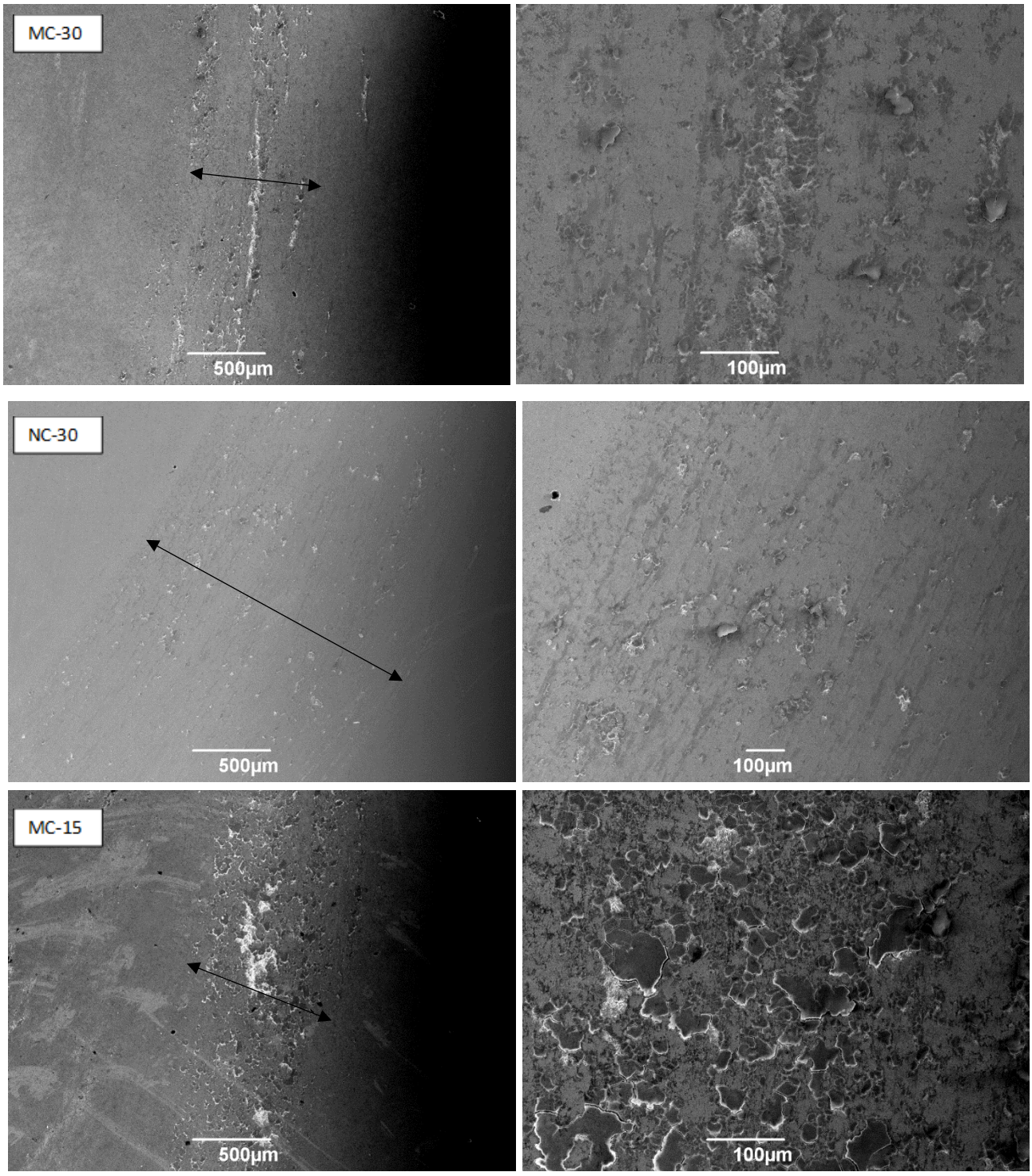


**Figure 4-20 - Left: Lower magnification SE SEM images of the plan view of the worn surfaces of the three coatings at 240N. Right: Higher magnification top down SE images of the worn surfaces**

## 4.8 Discussion

### 4.8.1 Powder feedstock characterisation

Different phases were found to be present within the NC-30 powders compared to the other two, with the presence of $Cr_3C_2$ and W detected within the nanostructured powder but not within the other two.

Elemental W has been shown to form at temperatures above 1500K in the WC-Co-Cr system [112]. The binder phase becomes molten and the dissolution of the WC grains can occur and as discussed in Section 2.5, this can lead to the formation of $W_2C$ and W. High magnification BSE images of polished NC-30 powder in Figure 4-6 reveal contrast difference throughout the binder phase in the regions surrounding grains of WC. This may be due to the addition of tungsten to the binder phase, providing more evidence for the explanation above. Due to their lower surface area to volume ratio, the WC grains found on the NC-30 are much more susceptible to dissolution than the larger ones found on the other two powders. This could explain why XRD measurements could not detect any $W_2C$ and W within the microstructure of the MC-30 and MC-15 powders, as the larger WC grains are more resistant to dissolution and may not therefore dissolve into the binder as readily during the manufacturing of the powder.

Aside from tungsten rich phases, XRD did not reveal the presence of $Cr_3C_2$ within the microstructure of the two larger grained MC-30 and MC-15 powders but did within NC-30. Cr rich carbides have previously been shown to form when dissolution of WC grains into a CoCr matrix takes place

[70,112], showing their presence may also be due to carbide dissolution during processing. However, the presence of elemental tungsten and $Cr_3C_2$ were not detected within the sprayed NC-30 coating, meaning these phases either underwent transition into another phase due to the temperature changes during the spray process, or exist in the coating at levels below the detection limit of XRD methods. It is therefore unclear whether the presence of these extra phases within the NC-30 feedstock powder influences the overall coating properties and sliding wear resistance.

### 4.8.2 Coating characterisation

The fine powder feedstock was seen to suffer more decarburisation than the other larger powders during the spray process, indicated by this coating having the lowest ICR. This indicates that when using this spray system alongside the spray parameters used within this study, overall particle size can be seen to have a larger effect on decarburisation than WC carbide size. It is described in Section 2.5.1 that decarburisation processes occur when the binder phase becomes molten, meaning the rate of carbon loss is strongly affected by the in-flight temperature of the sprayed particles. Assuming the composition of each powder is similar, the MC-15 particles would have a lower mass than particles of the MC-30 and NC-30 powders, due to their smaller size. If assuming the specific heat capacity of the materials is constant due to having the same composition, less heat energy would be required to melt the MC-15 particles in comparison to the other two powders. Therefore, the higher carbon loss occurring in the MC-15

powder is likely due to these particles reaching higher temperatures in flight in comparison to the other powders. At higher temperatures decarburisation increases due to either heightened solubility of the liquid binder, or increased liquid fraction of the binder phase.

The MC-30 particles can be seen in Figure 4-1 to possess less compact morphology in comparison to the NC-30 particles in Figure 4-5, which could suggest the real surface area of MC-30 particles may be larger than that of the NC-30 particles. A smaller overall surface area would result in reduced heat transfer into the particle during the spray process for the NC-30 powder and this may counteract the effect of the nanostructured WC grains more easily dissolving into the liquid binder.

### 4.8.3 Mechanical properties of coatings

It was previously discussed in Section 2.5.3 that powders with a smaller WC grain size should lead to sprayed coatings with a higher microhardness and fracture toughness due to the Hall-Petch effect. However, it has been found that the coating formed from the nanostructured powder had the worst mechanical properties of all three coatings tested. The MC-15 powder was found to produce the coating with the highest microhardness, and there are two possible explanations for this. Firstly, due to this powder undergoing the most decarburisation, the MC-15 coating will contain more $W_2C$ than the other two coatings. It has previously been shown that the microhardness of cast WC and $W_2C$ are 17000MPa and 30000MPa respectively [113], meaning that the presence of more $W_2C$ within the MC-

15 coating microstructure may lead to an increase in microhardness. However, $W_2C$ has been shown to have a lower fracture toughness than WC, with a fracture toughness of 3.6MPa.$m^{1/2}$ compared to 5.9MPa.$m^{1/2}$ in WC, meaning increased decarburisation results in a reduction in coating fracture toughness. This hypothesis has been discussed in other work [67,114], and this could explain why the MC-15 coating has a higher microhardness, but lower fracture toughness than the MC-30 coating. Another reason for the higher microhardness of the MC-15 coating could be due to higher in-flight velocities reached by the smaller particles, as under the same conditions smaller particles require less kinetic energy to reach a certain velocity than larger particles of the same material, due to their lower mass. A previous study carried out using the same ID-HVOF thermal spray torch determined that increased particle velocities lead to greater cold hardening effects, due to increased peening of the substrate [115].

### 4.8.4 Sliding wear behaviour

As discussed within the literature review in Section 2.5.5, the existence of phases formed by decarburisation had previously been stated to reduce the sliding wear resistance of WC-Co-Cr thermal spray coatings, as their presence is said to increase the overall brittleness of the coating. The MC-15 coating, which was found to have the lowest ICR, indicating a higher ratio of $W_2C$ to WC within the coating microstructure was seen to wear the most at the 96N and 168N loads seemingly in agreement with the above hypothesis. As the load was increased to 240N the performance of the MC-

15 coating was found to be better than the NC-30 coating, with wear rates of MC-15 at 240N being similar to those at the lower loads. This may indicate that the lower microhardness and fracture toughness of the nanostructured coating make it the most vulnerable to sliding wear at high loads.

The relationship between specific wear rate and load appears to differ for the nanostructured coating in comparison to the other two. At the lower 96N load, the oxidised particles did not form in as greater numbers of the worn surface of the NC-30 coating, possibly indicating lower frictional forces and therefore less heat energy available. However, without accurate friction coefficient measurements, this claim cannot be verified.

Wear of the spherical counterbody produces a flat surface on the side of the ball contacting the coating, with the surface area of this flat surface expanding as counterbody wear increases. As a result, the actual contact area between the counterbody and coating surface will increase throughout the test, leading to a reduction in contact pressure. This could possibly explain the reduction in specific wear rates for the MC-15 coating at high load when accompanied by a sharp rise in counterbody wear. A similar argument can be used to possibly explain the lower number of oxidised regions on the worn surface of the NC-30 coating tested at the 240N load. Due to the greater width of the worn surface, the contact area between the two surfaces is larger meaning frictional forces are less concentrated. This may have the effect of spreading out the heat produced by the contact over

a larger area resulting in lower localised temperatures and therefore decreased tribo-oxidation.

## 4.9 Summary of chapter and recommendations for ID-HVOF thermal spray

From the results presented in this chapter, differences in microstructure, mechanical properties and wear behaviour can be seen between the coatings of the nanostructured NC-30 powder and the larger WC grained MC-30 and MC-15.

It was determined that when spraying using the spray parameters utilised within this work, the nanostructured NC-30 powder was found to decarburise to a similar degree to the MC-30 powder. The fact that the nanostructured NC-30 powder was found to suffer decarburisation at a similar level to that of the MC-30 powder contradicts previous work on nanostructured WC-Co-Cr powders discussed in Section 2.5.3. It has been said that nanostructured powders were found to undergo more carbon loss, because the smaller carbide grains more readily dissolve into the molten binder than larger carbide grains [55]. However, the results of this study indicate that the size of the particles has a much more significant effect on decarburisation than WC grain size, with the MC-15 powder having a lower ICR than the other two powders.

The nanostructured NC-30 coating was measured to have a lower microhardness and indentation fracture toughness that the larger WC grained coatings. This result again is a contradiction to previous work, in

which a nanostructured WC-Co powder was found to result in coatings with a higher microhardness in comparison to a coarse-grained WC-Co powder. In the mentioned referenced study, the nanostructured powder was seen by the other researchers to decarburise severely, leading to a high amount of $W_2C$ and W within the coating microstructure in comparison to the other larger grained WC-Co coating. Due to the hardness differences between bulk WC and $W_2C$ discussed in Section 4.5, this could explain the microhardness differences found within the aforementioned study and the work presented within this chapter [55].

As discussed in Section 2.4 ID-HVOF thermal spray systems must be capable of applying coatings at potentially very short stand-off distances, with smaller, lighter particles offering the advantage of requiring less kinetic energy to be accelerated to the velocities needed to provide sufficient plastic deformation on impact with the substrate. The MC-15 coating was found to have the highest microhardness of all tested within this study, alongside comparable fracture toughness and wear resistance to the other coatings tested. The larger amount of decarburisation suffered by this powder during spraying due to its smaller size was seen to not severely reduce the wear resistance of the coating. Therefore, the results presented within this chapter indicate that this powder may be suitable for the ID-HVOF thermal spray experiments covered later throughout this thesis. As the nanostructured NC-30 powder produced coatings with the worst mechanical properties of all coatings tested alongside no significant

advantage in wear resistance, this powder will not be used for subsequent ID-HVOF thermal spray trials.

# Chapter 5. ID-HVOF thermal spraying of WC-Co-Cr coatings

## 5.1 Introduction

Having the ability to deposit coatings that perform to an acceptable level in today's market at stand-off distances as small as possible is of great importance to the thermal spray industry. This would provide a wider variety of potential applications for ID-HVOF thermal spraying, opening the technique to new markets in which previously HVOF thermal spraying was not feasible. As discussed in Section 2.4, applying coatings at very small stand-off distances presents significant challenges, due to the greater particle acceleration required to produce good coatings at smaller stand-off distances. This issue can partly be rectified using finer powder feedstocks, which itself presents new problems such as increased heating of the particles. However, the results of Chapter 4 indicated that coatings sprayed from a powder feedstock with a smaller particle can compete with ones sprayed from larger powders in wear resistance applications and will therefore be used in the subsequent experiments.

The literature review identified that there is a current lack of knowledge regarding the microstructure and sliding wear resistance of WC-Co-Cr coatings sprayed by HVOF thermal spraying at small stand-off distances. This is likely because the dimensions of the majority of the commercially used HVOF thermal spray systems limited them for use in applications where longer stand-off distances are possible, therefore removing the

problems mentioned above. It was also determined in the literature review that there is only current one study in which WC-Co-Cr coatings were applied on internal surfaces using an ID-HVOF thermal spray process [1] and it involved spraying onto cylindrical parts with an internal diameter of 200mm, meaning the effect of spraying WC-Co-Cr thermal spray coatings on the internal surfaces of parts smaller than this is currently unknown.

As highlighted in Section 2.4 certain control aspects of the spray process are more difficult to manage in ID thermal spray processes in comparison to outer diameter spraying, for example substrate cooling and the accumulation of residual particles. Excessive heating of the substrate during the spray process can affect the properties of the final coating, including changing the residual stresses and phase composition within the coatings. The effects of thermal diffusion coefficient mismatch between coating and substrate will be increased at higher substrate temperatures leading to higher thermal stresses present within the coatings. This has been shown to result in greater unwanted tensile residual stresses within HVOF thermal spray coatings. While measures can be taken to control substrate overheating issues in ID thermal spray processes, such as using special tube or air-jet cooling systems it is still largely unclear how the microstructure and tribological properties of the coatings, as well as the residual stress profile of the coatings are affected by the internal thermal spray setup.

In this chapter the ID-HVOF thermal spray system will be used to apply coatings of the MC-15 powder studied in Chapter 4 onto the internal surface of cylindrical tubes with internal diameters of 70mm, 90mm and 110mm to investigate the effect of part diameter on the microstructure, mechanical properties and wear resistance of the sprayed coatings. The feedstock powder used for all coatings was the previously studied MC-15 powder; details and characterisation of this powder feedstock can be found in Section 4.4.

## 5.2 Spray Parameters

A mixture of hydrogen (200 – 300 SLPM), air (100 – 400 SLPM) and oxygen (100 -200 SLPM) was used to spray all coatings studied, with the combustion chamber pressure coming to 8bar. When spraying samples at each ID, the same spray parameters were used in order to investigate the effect of the change of ID.

## 5.3 Coating Characterisation

### 5.3.1 Phase analysis

The coatings sprayed within the 70mm, 90mm and 110mm tubes are named as ID70, ID90 and ID110, respectively. To assess the phase composition of the as sprayed coatings, XRD was used, with the results presented in Figure 5-1. The phases WC, $Co_6W_6C$ and a solid solution of (Co,Cr) were found within the powder feedstock. When comparing the XRD diffractograms of the coatings to that of the MC-15 powder feedstock, the

formation of $W_2C$ can be seen to have occurred during the spray process. The presence of $Co_6W_6C$ can no longer be detected in the coatings, with $Co_3W_3C$ detected instead, implying carbon has dissolved in the binder phase during spraying, as the ratio of carbon to metallic elements in the binder is greater for $Co_3W_3C$ in comparison to $Co_6W_6C$. Diffraction peaks within the $2\theta=37°-46°$ range can be seen to have broadened, indicating possible amorphous material within the microstructure of the coatings [56]. Quantitative Rietveld refinement determined that the $W_2C$ content of the ID70, ID90 and ID110 coatings was at 6.76wt.%, 6.81wt.% and 4.68wt.%. However, the ID110 coating was found to contain the highest weight percentage of the η-phase carbide $Co_3W_3C$ of all coatings, at 8.19%wt. in comparison to the ID70 and ID90 coatings with η-phase carbide contents of 6.66wt.% and 6.81wt.%.

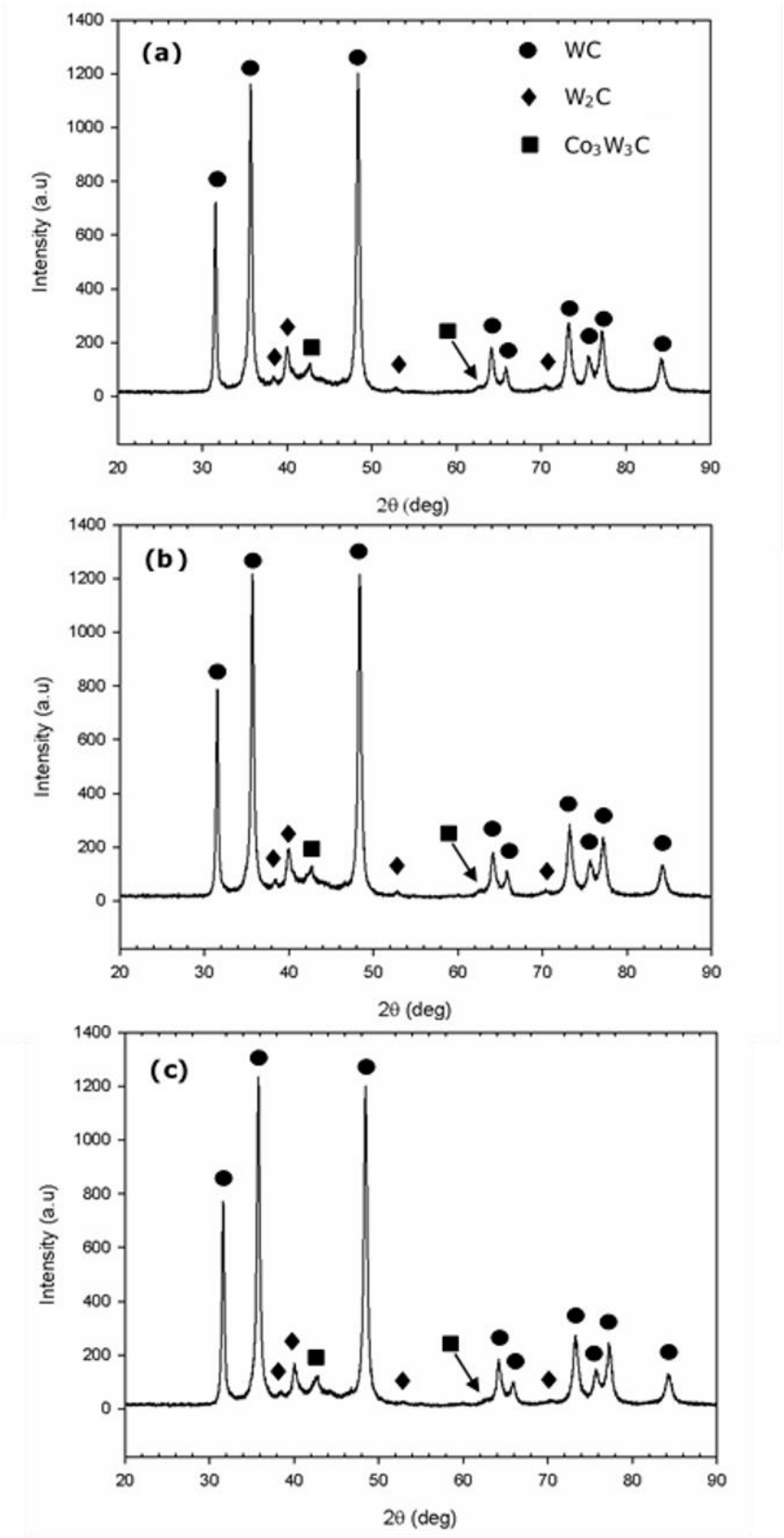


**Figure 5-1 - XRD diffractograms of the three sprayed coatings and feedstock powder (a) ID70 (b) ID90 (c) ID110**

### 5.3.2 Coating mechanical properties and microstructure

The microhardness, indentation fracture toughness, elastic modulus, coating thickness and porosity are presented in Table 5-1 below.

| Coating Name | Thickness (µm) | Microhardness (HV 0.3) | Indentation Fracture Toughness $K_{IC}$ ($MPa.m^{0.5}$) | Elastic Modulus (GPa) | Porosity (%) |
|---|---|---|---|---|---|
| ID70 | 224±7 | 1201±106 | 3.9±0.4 | 375±82 | 1.6±0.8 |
| ID90 | 214±7 | 1319±40 | 4.8±0.2 | 419±52 | 1.4±0.4 |
| ID110 | 129±4 | 1310±51 | 3.3±0.5 | 342±74 | 1.4±0.5 |

**Table 5-1 - Microhardness, Indentation fracture toughness, elastic modulus, thickness and porosity of the as sprayed coatings**

The thickness of the three coatings was seen to differ significantly, with the ID110 coating found to have a lower thickness than the other two coatings. This could be related to the increased linear speed of the substrates during the spray run when mounted within the larger cylindrical tube, with the substrates mounted within the larger tube moving at a higher linear speed in relation to the torch.

The ID70 coating was found to have the lowest microhardness and highest porosity, with also the largest standard deviation of readings, implying more non-homogeneity throughout the microstructure. The ID90 coating was measured to have the highest indentation fracture toughness and elastic modulus of all coatings measured, with ID110 having the lowest in both regards. The measured standard deviation of the elastic modulus was found to be significant for all three coatings. Due to the small size of the nano indenter used, the area of indentation could have covered either a WC

grain, area of binder phase or a combination of two. As each of these different phases within the coating exhibit very different mechanical properties, this could explain the large deviation in elastic modulus readings. 30 indents were performed to determine the mean elastic modulus for each coating to attempt to improve the reliability of the results, however it appears that the amount of error may still be significant.

Low magnification BSE SEM images of the three coatings are displayed in Figure 5-2; the difference in coating thickness can be clearly seen. Throughout the microstructure of all coatings but particularly in the ID70 coating, areas of a phase with a darker contrast can been observed. EDX point scans carried out in these areas determined the composition of this phase was primarily Fe, with trace amounts of Si and Mn also detected, indicating that these are impurities within the coating microstructure.

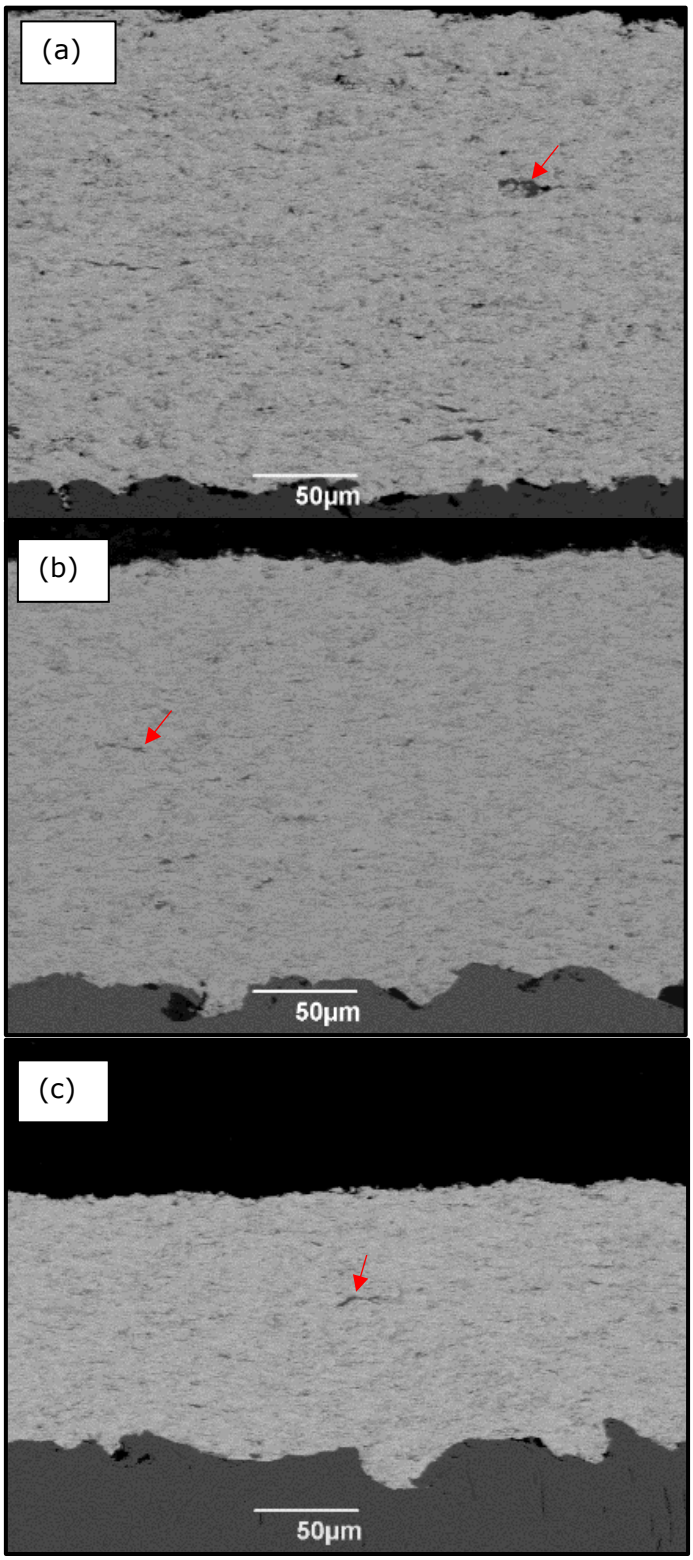


**Figure 5-2 - Low magnification BSE SEM images of the coating cross section. (a) ID70 (b) ID90 (c) ID110. Impurities within the coating likely originating from the substrate are marked with arrows**

The microstructure of the three coatings can be seen in the BSE SEM images in Figure 5-3. Grains of WC can be observed embedded in a binder phase with a varying contrast, like that seen in the WC-Co-Cr sprayed in the previous chapter.

In the SEM image of the ID70 coating in Figure 5-3a, splats with a shape reminiscent of the original feedstock powder can be observed, with an example shown below in Figure 5-4. The presence of such splats could indicate that these particles underwent insufficient plastic deformation on impact with the substrate, resulting in irregularities within the lamellar coating structure. The presence of this feature was not observed within the ID90 and ID110 coatings, meaning it could be an effect caused by the shorter standoff distance.

In areas of the ID110, a dark phase can be observed lying between the splats in certain areas of the coating, with an example shown below in Figure 5-5. EDX point scans along this phase reveal the phase contains a mixture of tungsten, oxygen and then lesser amounts of carbon, cobalt and chromium.

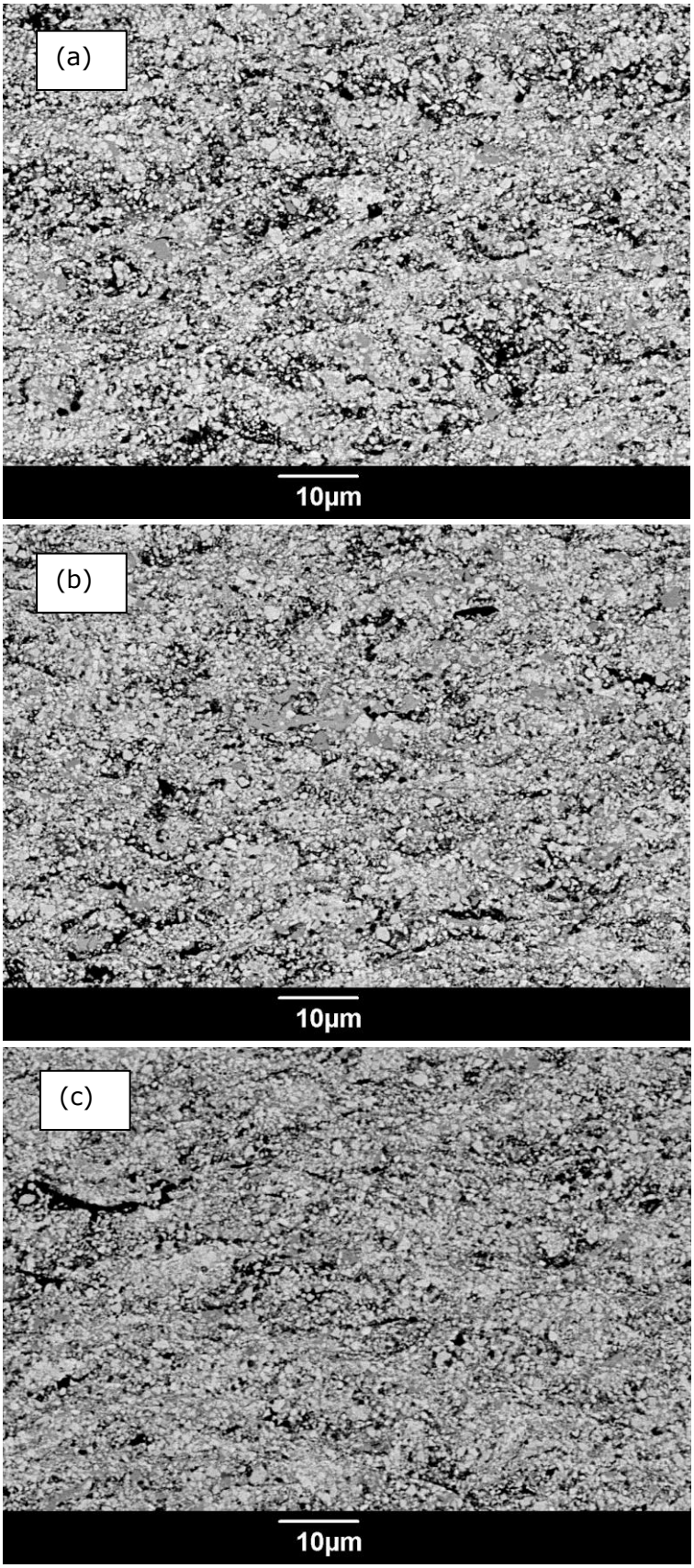


**Figure 5-3 - Higher magnification BSE SEM images of the cross section of the three coatings (a) ID70 (b) ID90 (c) ID110.**

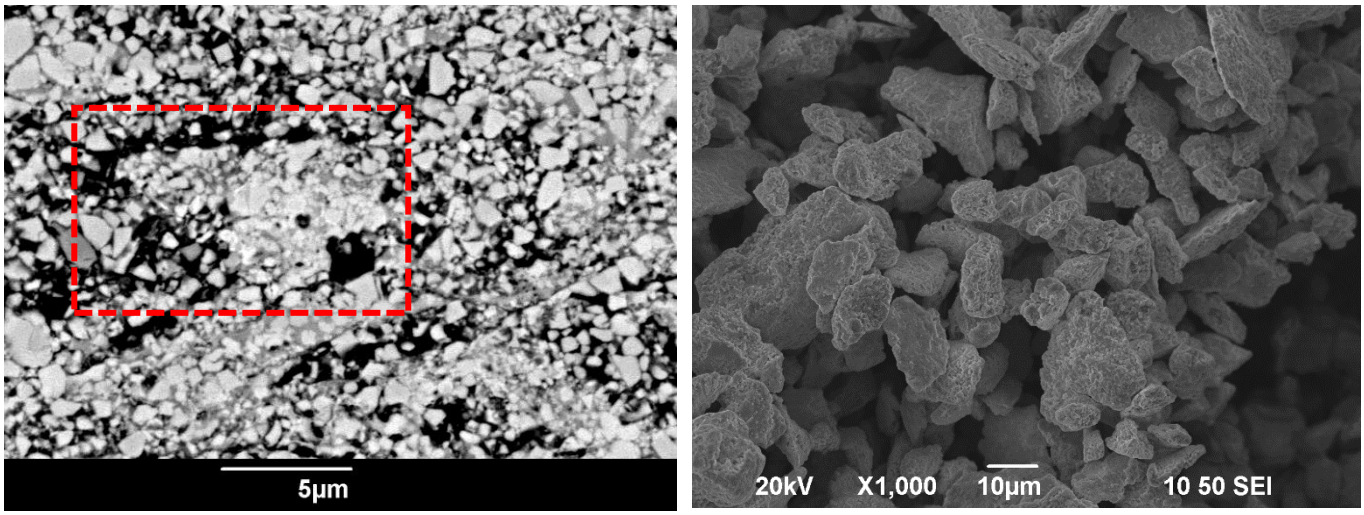


**Figure 5-4 - SEM images of the cross section of the ID70 coating showing an example of a splat having a similar shape to that of the MC-15 powder feedstock. Porosity can be seen at the splat perimeter**

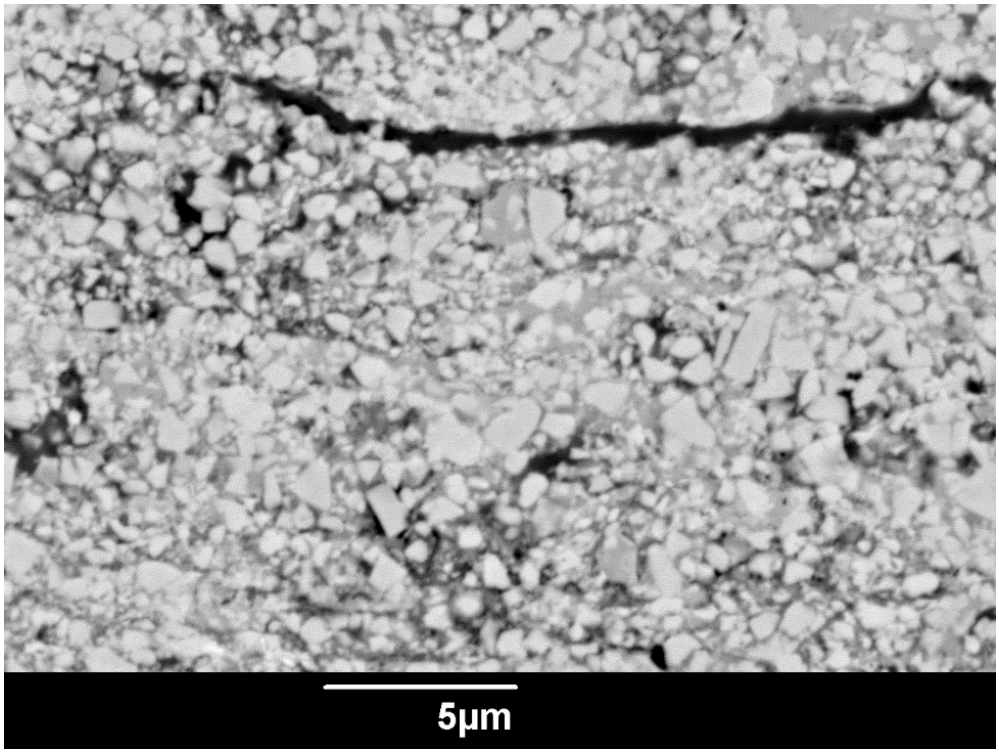


**Figure 5-5 - BSE SEM image showing an example of an intersplat phase found within the ID110 coating cross section**

## 5.4 Sliding wear behaviour and examination of worn surfaces

The specific wear rates of the three coatings measured when testing at both loads are presented in the bar graph in Figure 5-6 below.

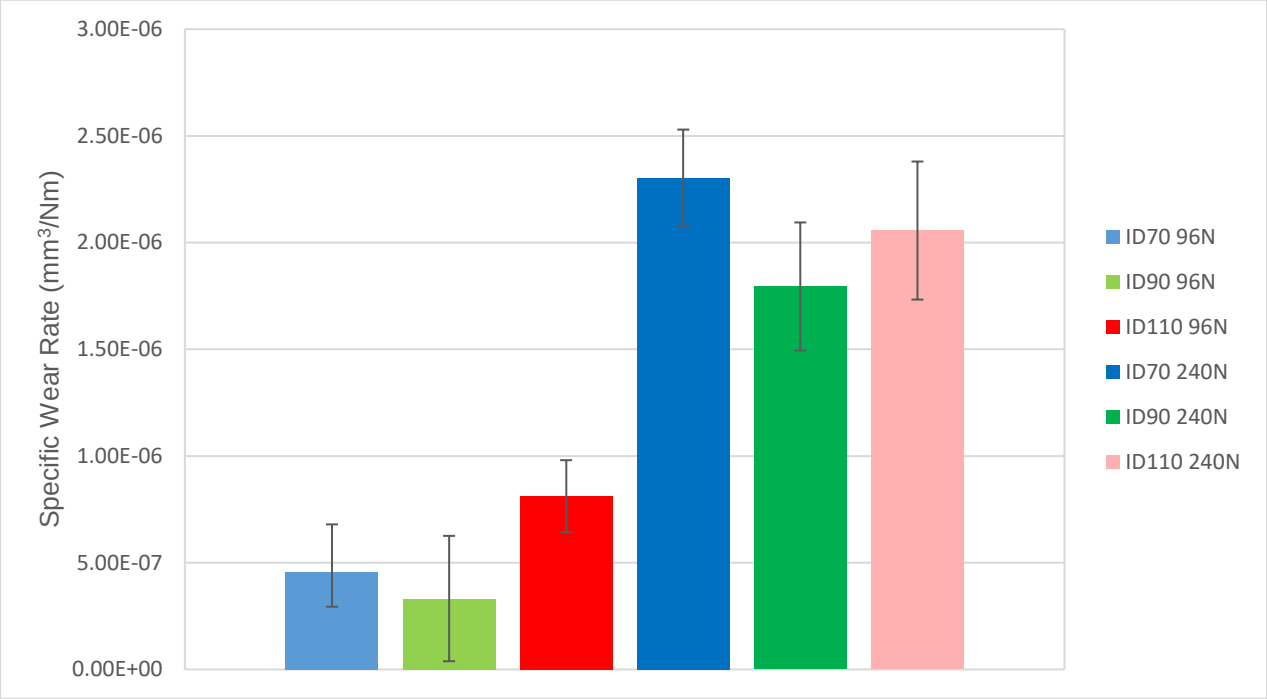


**Figure 5-6 -Specific wear rates of the three coatings when tested at the 96 N and 240 N loads**

At the lower 96N load, all specific wear rates were seen to be in the $10^{-7}$mm3/Nm range indicating that wear is relatively mild. At the lower load the ID110 coating was found to suffer the highest specific wear rate; however, as the load was increased to 240N the ID70 coating was found to undergo the most material loss. At both loads the ID90 coating was found to be the best performer out of the three coatings.

To gain further insight regarding the mechanisms of wear taking place, the plan view of all wear tracks was imaged using SEM. The images of the worn coating surfaces from the tests carried out at the 96N load are presented

in Figure 5-7. On the ID70 sample, isolated areas with a darker contrast can be observed. EDX point scans in these areas reveal a high oxygen content and tungsten content, like that seen on the worn surfaces of the coatings studied in the previous chapter. It is therefore likely again that the formation of these features is again due to tribo-oxidation processes. Cracks can be seen running across the worn surface of the ID70 coating, perpendicular to the direction of the counterbody movement. Small pores can be seen particularly on the worn surface of the ID90 coating; these are likely sites at which the pullout of grains of WC has occurred due to the size and positions of these voids being in line with that of the WC grains seen throughout the coating. Meanwhile on the worn surface of the ID110 coating evidence of large areas of material pullouts can be seen; with an example site in Figure 5-7f being at least 50μm in diameter. It can also be observed that the wear track on the ID110 is much wider than the track on the ID90 coating.

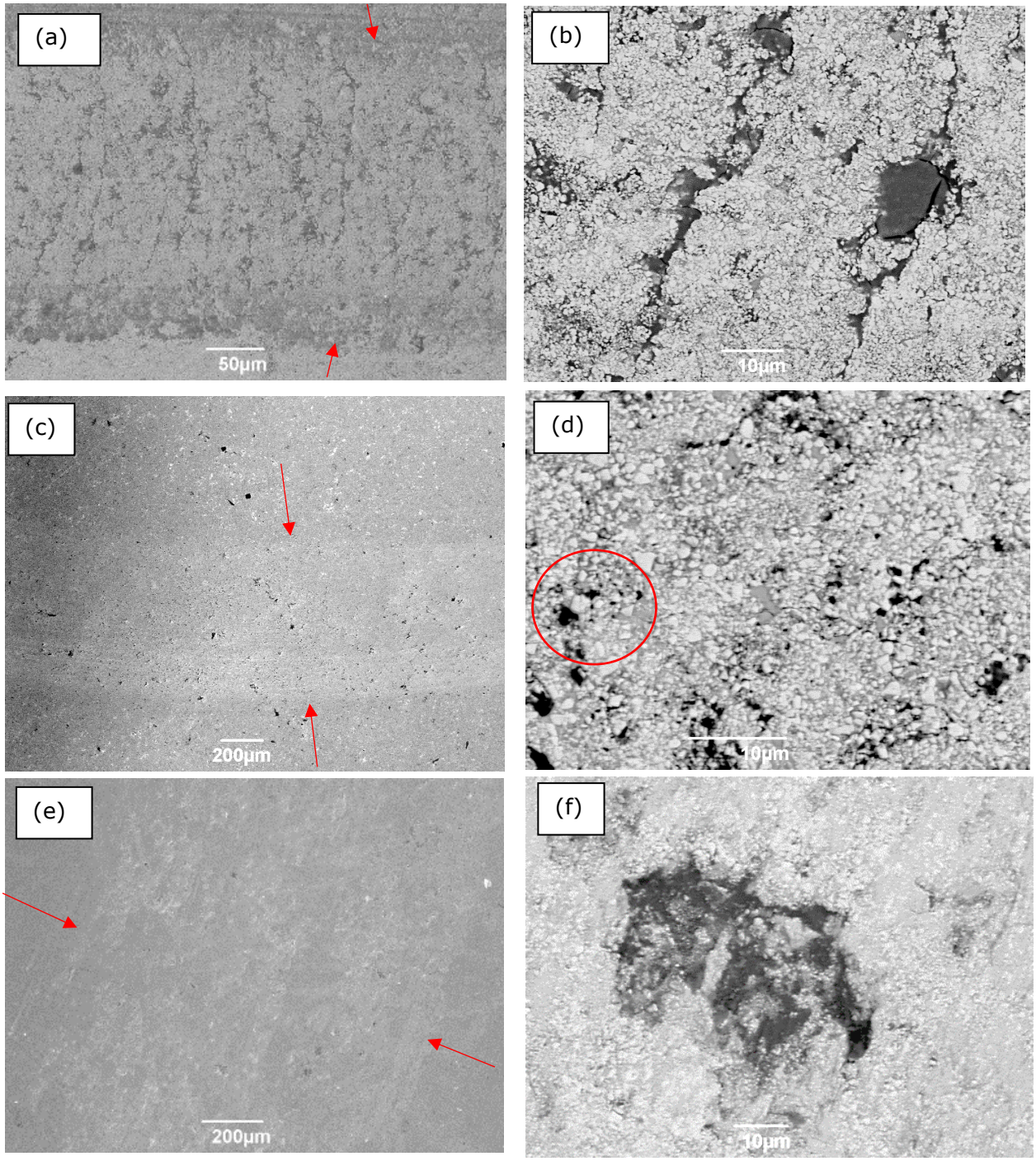


**Figure 5-7 - Plan view SEM SE images of the wear scars produced from the sliding wear tests at 96N. The position of the wear track lies between the arrows. The images on the right show higher magnification BSE images of the wear track surface, with an area in which WC grain pullout has occurred circled. (a,b) ID70 (c,d) ID90 (e,f) ID110**

When the load was increased to 240N, differences can be seen on the worn surfaces of all three coatings, displayed in Figure 5-8. The surfaces of the ID70 and ID90 coatings share some similar features.

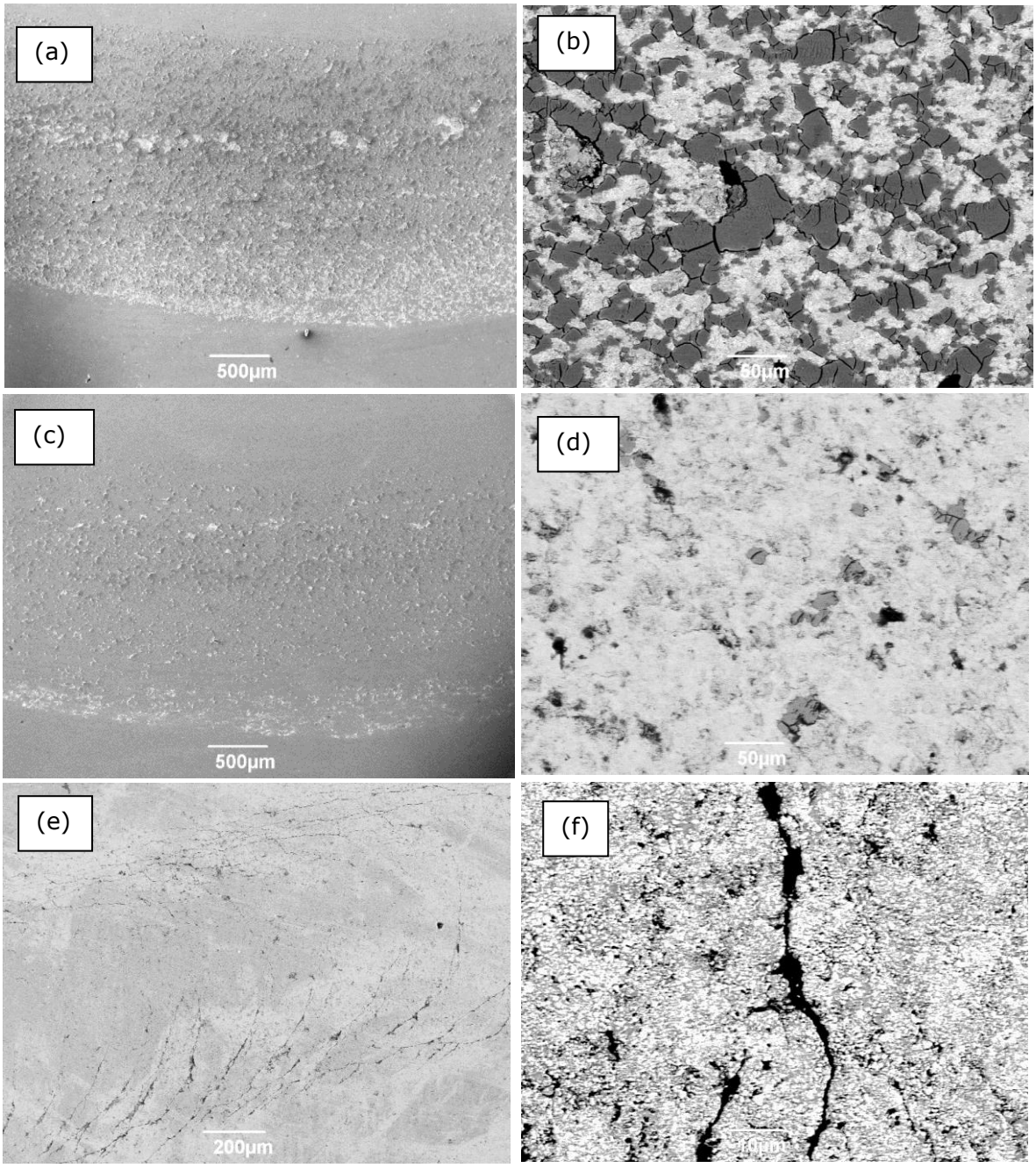


**Figure 5-8 - Plan view SEM images of the wear scars produced from the sliding wear tests at 240N for all three coatings. The images on the left column show low magnification SE images of the wear track and the image on the right column show higher magnification BSE images. (a,b) ID70 (c,d) ID90 (e,f) ID110**

While the patches of oxidised material can be again observed on the worn surfaces of both of these coatings, it is much more abundant on the worn surface of the ID70 coating. This coating was measured to suffer the highest wear at 240N, indicating their formation may be a key factor in the mechanism of wear taking place. On the worn surface of the ID110 coating in Figure 5-8e cracks can be seen on the track that appear to originate from the track centre, before propagating out to the edge of the track, perpendicular to the counterbody movement direction. The cracking can be seen to propagate particularly through the binder phase.

To uncover more information on the wear mechanisms taking place, the cross sections of the worn coatings were imaged using SEM, with the images displayed in Figure 5-9. The cross section of the ID70 and ID90 shows a similar shape at both loads, with no sub surface cracking observed. In contrast to this, large subsurface cracks can be observed within the ID110 coating following the sliding wear testing at both loads. Cracks can be seen propagating into the centre of the coating parallel to the coating/substrate interface from the bottom of the wear track.

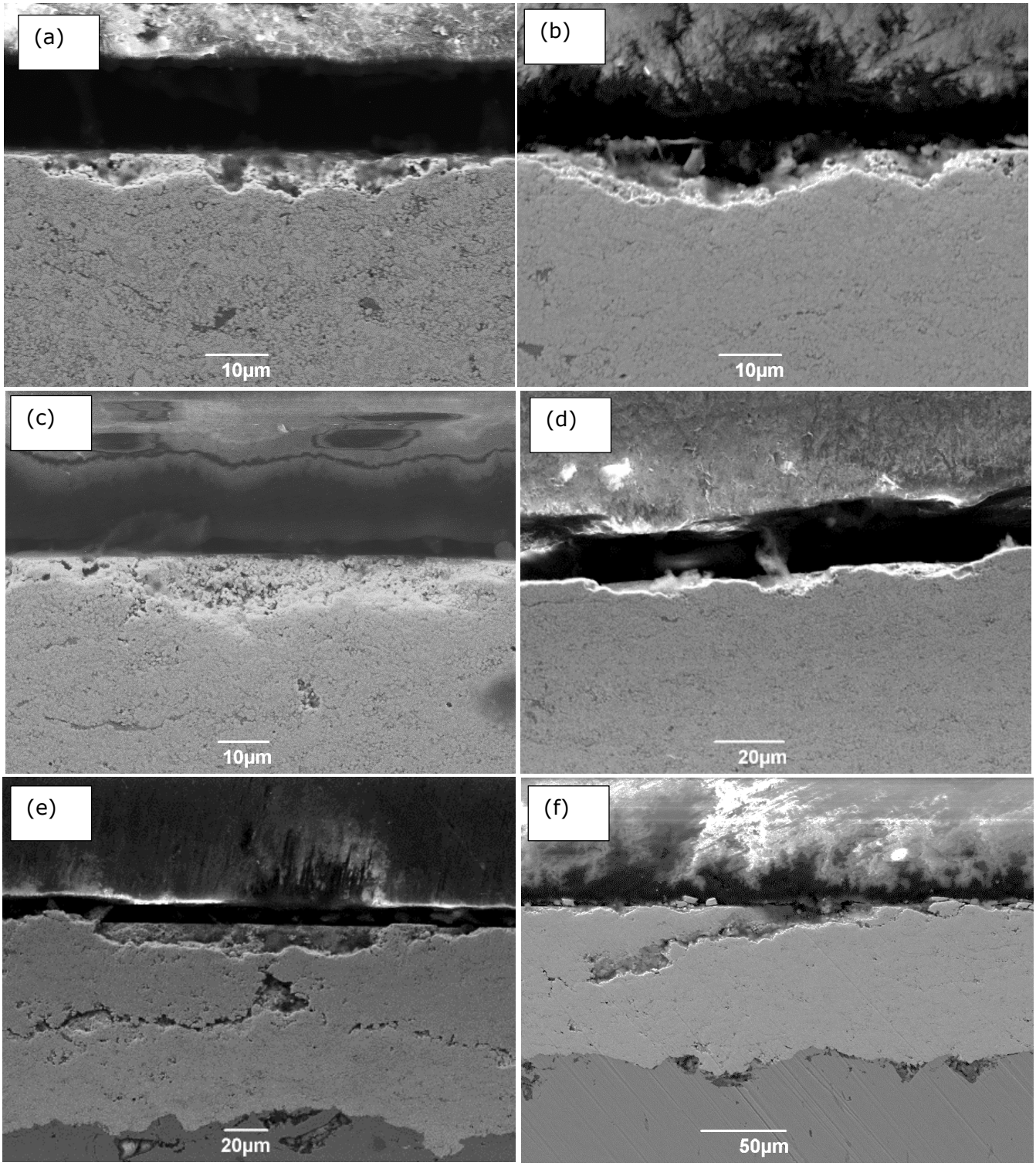


**Figure 5-9 - SEM images of the cross section of the worn coating surfaces. (a) ID70 96N (b) ID70 240N (c) ID90 96N (d) ID90 240N (e) ID110 96N (f) ID110 240N**

## 5.5 Discussion

### 5.5.1 Effect of part diameter on coating microstructure and phase content

From the results presented throughout this chapter, it is clear that the internal diameter of the cylindrical tube has an effect on the microstructure, mechanical properties and subsequently the sliding wear resistance of the coatings.

The XRD results and Rietveld analysis revealed differences in the phase composition of the coatings. The presence of $W_2C$ was detected in all three coatings, however this phase was present in lower amounts in the ID110 coating in comparison to the other two. Due to the longer stand-off distance used when spraying this sample, this result contradicts previous data in which it has been stated the use of longer stand-off distances should lead to an increase of the $W_2C$ phase, as the in-flight particles are at an elevated temperature for a longer period of time, allowing more decarburisation to take place [37]. It was also determined that the ID110 coating contained a higher amount of $Co_3W_3C$ phase than the other two coatings, a phase that was not detected in the feedstock powder and as a result must have formed during the spray process. Due to the tungsten and carbon contents of this phase, it is likely also a product of WC grain dissolution into the CoCr binder during the spray process. The presence of η-phase carbides has been detected in WC based coatings that have been subjected to elevated temperatures for a period of time, for example WC-Co coatings that were

found to contain no η-phase carbides after spraying were found to contain large amounts after heat treatment at 600°C [116].

It has been previously shown that $W_2C$ is not thermodynamically stable at temperatures below 1523K, with the phase undergoing solid state decomposition at temperatures below this point [60]. Due to the rapid solidification of splats following impact with the substrate in traditional external thermal spray processes, there is little time for this decomposition to occur meaning $W_2C$ is present in the final solid coating. For cases in which the coatings undergo slow cooling or further heat treatment, the stable crystalline η-phase carbides are formed instead. The phase diagram of the W-Co-C system indicates the formation of $M_6C$ carbides without the presence of $M_{12}C$ occurs when temperatures exceed approximately 1150°C. [73]. As particle temperatures in HVOF thermal spraying likely exceed 1150°C [14], the conditions may be right for $M_6C$ carbide to form.

The lower $W_2C$ and higher $Co_3W_3C$ content of the ID110 is likely related to differences in the thermal state of the particles during deposition. Two possible reasons can be formulated to explain the differing phase content: either particles sprayed at the longer stand-off distances started to cool in-flight prior to impact with the substrate, resulting in the formation of η-phase carbides. Alternatively, the substrate temperatures during the spray process when spraying the ID110 coating was higher than that when spraying the other coatings. This would result in slower cooling of the

deposited splats post deposition heating, promoting η-phase carbide formation.

Evidence for the first explanation could possibly be given by the fact that the coating thickness of the ID110 was a lot lower than the other two coatings. The in-flight temperature of the particles prior to impacting the substrate has been shown to affect the deposition efficiency, particularly if the degree of melting of the particle is affected. When the degree of melting of the in-flight particles is lower, particles may simply bounce off the substrate meaning they are not deposited, resulting in a lower coating thickness and higher porosity [117]. However, it was determined that the porosity of this coating was actually lower than that of the ID70 coating, and the hardness was similar to the ID90 coating, which would likely not be the case if the particles were insufficiently melted on impact. Therefore, it is more likely that the difference in phase content of the ID110 coating is due to an increase in the substrate temperatures during the spray process. Unfortunately, a record monitoring the temperatures of the substrate during the spray process was not kept, meaning these claims cannot be verified for certain. The increased presence of $Co_3W_3C$ within the coating microstructure of WC-Co has been shown to lower the overall fracture toughness of the material [84,118], meaning this could explain the lower fracture toughness of the ID110 coating. The measured elastic modulus of the three coatings was seen to follow the same trend as the fracture toughness, similar to that seen in other work on WC-Co-Cr thermal spray

coatings [119], with the ID90 coating having the highest fracture toughness and elastic modulus and ID110 the lowest.

Differences in the mechanical properties of the three coatings can be observed. The microhardness of the ID70 coating was determined to be lower than that other of the other two coatings, as well as this coating having the highest porosity. As heightened porosity has been shown to be linked with reduced microhardness in thermal spray coatings, this could possibly explain the difference in microhardness between the ID70 coating and the other two. It is also possible that this microhardness reduction is linked to the temperature and velocity of the in-flight particles. The microhardness of thermal spray coatings has been previously shown to be strongly linked to in-flight particle velocity, with higher velocities resulting in coatings with increased hardness [119]. At the short stand-off distance used when spraying the ID70 coating, it is possible in-flight particles are still undergoing acceleration meaning the velocity at the moment of impact with the substrate is lower than when spraying at larger stand-off distances. This may also explain the increased porosity found within the ID70 coating, due to the reduced velocity leading to lower plastic deformation of the particles on impact leading to the formation of pores. Splats within the ID70 coating still retaining a shape similar to that of the original powder feedstock were seen in places throughout the microstructure, which may be present because of insufficient deformation on impact of particles lacking enough velocity, providing evidence for this explanation. Most splats within the ID70 coating appear well flattened

throughout the microstructure, with only some appearing under deformed as observed in Figure 5-4.

For traditional HVOF thermal spray torches that use axial injection for the feedstock powder, the majority of the particle acceleration occurs within the combustion chamber and nozzle [120]. However, the feedstock powder is injected radially downstream of the combustion chamber when spraying with the ID-HVOF thermal spray torch used within this chapter. This means the particle acceleration will only take place outside the torch within the flame meaning there may be less time for the injected powder to distribute. Due to effects present within the flame such as turbulence and flow fluctuations, it is possible that particles may undergo different amounts of acceleration depending on their actual position within the flame and a lower residence time of the particles in the flame when spraying at shorter stand-off distances could increase this issue.

The effect of coating thickness on the properties of WC-Co-Cr thermal spray coatings has been previously investigated; for very thin coatings with a thickness of 59μm, increasing this thickness to 80μm led to a hardness increase of almost 250 HV0.3. However as the thickness was increased further up to a thickness of 150μm, the increase in hardness began to quickly tail off, with subsequent layers doing little to raise the coating hardness [121]. The measured thickness of the three coatings within this study are all within the range of thickness at which extra layers were shown to provide little benefit to hardness; therefore it is unlikely the thickness

differences between the coatings can be used to explain any hardness variations.

Impurities originating from the substrate were found to be present within all three coatings but were observed more within the ID70 coating. As magnets were used to mount the substrate discs within the inside of the cylindrical tubes, it is possible that loose debris produced during spraying was attracted to the magnet, before being covered up by the subsequent passes of the spray torch resulting in impurities within the layers of the coating. The effect was more prominent when spraying the ID70 coating due to the reduced size of the tube meaning any debris is closer to the mounting magnets and as a result, these impurities were found more within this coating.

### 5.5.2 Effect of part diameter on coating wear behaviour

The specific wear rates of the three coatings, alongside the SEM images of the worn coating surfaces, indicate that there may be differences in the mechanisms of wear occurring within this study. When tested at the 96N load, cracks can be seen lying across the whole width of the wear track and is accompanied by oxidised material. When the load is raised to 240N, the amount of visible oxidised material on the surface of the track is shown to increase. Due to the lower microhardness of the ID70 coating, material can be broken off the surface of the coating more easily, which may then lead to the formation of oxidised material via tribooxidation processes. The oxidised coating material may then fall into the pits left from the pull-out

of coating material, leading to spots of oxidised areas found across the worn surface. As the load is increased the effect is amplified due to the higher contact pressure, leading to accelerated debris formation and oxidation. The size of the oxidised sites on the worn surface is in the ranges of the size of one of more feedstock particles meaning the coating may be fragmenting at a multisplat level. This could indicate the cohesion between the splats, or groups of splats is not as high within this coating and this could be linked with the insufficient particle acceleration caused by the short stand-off distance.

On the worn surface of the ID90 sample tested at the 96N load, sites at which the pull out of the WC grains has occurred can be observed, similar to that seen in other work [18]. The edges of the hole left from these WC pull outs can be seen to consist of binder phase with straight edges characteristic of brittle fracture, meaning brittle fracture of the binder phase likely occurred resulting in pull out of the WC grains. When the load was raised to 240N areas of the coating in which larger scale pull out can be observed. This could be caused by the coalescence of cracks within the binder phase leading to reduction of the fracture toughness in these areas. The same oxidised material can also be seen on the surface of this coating, likely due to debris being created during the wear test that is vulnerable to oxidisation in a similar manner to the ID70 sample.

The increase in specific wear rate when the load was raised from 96N to 240N was found to be the smallest for the ID110 coating and the SEM

images show the smallest difference in track width between the two loads. Cracks can be seen at the edge of the wear track at the 240N load propagating from the centre of the track to the edge, parallel to the direction of counterbody movement. Compressive stresses are generated ahead of the counterbody, and cracks are formed pushing the coating material outwards towards the edge of the wear track. Localised regions of the coating in which defects such as porosity or impurities may provide areas in which the coating can buckle in response to these stresses [122], and then these spread due to propagation of interfacial cracks. Although the specific wear rate of this coating was found to be lower than that of the ID70 coating at the 240N, the subsurface of the coating under the wear track was found to have suffered severe damage, suggesting it may not be suitable for any application at higher loads.

The ID70 coating performed worse in the sliding wear tests than the ID90 coating at both loads due to its lower microhardness and fracture toughness in comparison to the other coating. ID110 was observed to crack at both loads, unlike the other two coatings, likely due to its reduced fracture toughness. From the results gathered within this chapter it appears the fracture toughness has a more dominant effect on the wear behaviour of the coatings than the microhardness, particularly at the 96N load. This is because while the microhardness of the ID90 and ID110 coatings was found to be similar, the specific wear rates and wear mechanisms were different. The results indicate that brittle fracture of the binder phase is a main cause of wear in these coatings regardless of whether individual WC grain or

larger scale material pull out is occurring. The reduced fracture toughness of the ID110 coating resulted in greater crack propagation from the wear tests in comparison to the other two samples leading to the highest specific wear rate measured at the 96N load. When the load was raised to 240N the ID70 coating then suffered the highest measured specific wear rates. This coating had the lowest microhardness of the three coatings, suggested that at the higher load the wear rates of the coating are largely affected by the coating microhardness.

The results of this chapter suggest the most durable coating for a wear resistance application was the ID90 coating, suggesting the spray parameters are best optimised for this stand-off distance of 50mm.

### 5.5.3 Differences between ID-HVOF and outer diameter HVOF thermal sprayed coatings

To assess differences inherent to ID-HVOF, the samples studied within this chapter were compared to the sample sprayed with the same feedstock powder, MC-15 coating studied in the previous chapter.

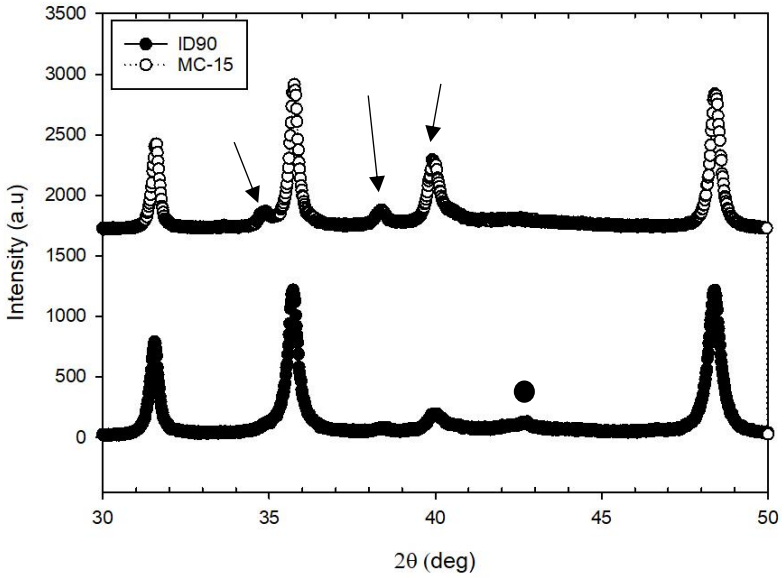


**Figure 5-10 - XRD diffractograms of the MC-15 and ID90 coatings. Peaks used to identify the presence of $W_2C$ are marked with arrows and $Co_3W_3C$ is marked with a circle**

The MC-15 coating from Chapter 4 was seen to contain a more significant amount of $W_2C$ in comparison with the ID-HVOF sprayed coating, as can be observed in the comparison shown in Figure 5-10. When comparing to the externally sprayed samples studied in Chapter 4, a difference in phase composition can be seen. The internally sprayed coatings were all found to contain lower amounts of $W_2C$ due to the less intense peaks at $2\theta \approx 40°$. The stand-off distance used when spraying the MC-15 coating was fixed at 120mm, in comparison with the 50mm stand-off for the ID90 coating; this further distance travelled by the particle in flight likely can explain the increase in $W_2C$ found within the coating due to an increased time in the flame at elevated temperature prior to deposition. XRD diffractograms show peaks with a greater intensity at $2\theta \approx 43°$ for the internally sprayed samples, indicating more $Co_3W_3C$ was found within these coatings in comparison to

the externally sprayed samples. As discussed in Section 5.5.1 the formation of $Co_3W_3C$ can occur when the temperature of the substrate is insufficiently cooled during the spray process. For internally sprayed coatings, cooling of the substrate may be more challenging due to the enclosed space, resulting in slower quenching of the particles on impact. This may have the effect of allowing the thermal decomposition of $W_2C$ to occur more readily, leading to the promotion of the formation of $Co_3W_3C$ in the microstructure. This may explain why the $Co_3W_3C$ phase was found within the internally sprayed coatings but not the outer diameter samples studied in the previous chapter.

The mechanical properties and specific wear rates of the MC-15 coating from Chapter 4 and best performing ID-HVOF coating ID90 are compared in Table 5-2.

| **Coating Name** | **Microhardness (HV0.3)** | **Fracture toughness ($MPa.m^{0.5}$)** | **Porosity (%)** | **Specific wear rate at 96 N ($mm^3/Nm$)** | **Specific wear rate at 240 N ($mm^3/Nm$)** |
|---|---|---|---|---|---|
| ID90 | 1319±40 | 4.82±0.24 | 1.29±0.41 | (3.32±8.27) x $10^{-7}$ | (1.79±0.30) x$10^{-6}$ |
| MC-15 | 1341±43 | 3.89±0.52 | 0.27±0.11 | (1.34±0.46) x$10^{-6}$ | (1.19±0.71) x$10^{-6}$ |

**Table 5-2 - Comparison of the microhardness, fracture toughness and porosity of outer diameter (MC-15) and ID HVOF (ID90) coatings**

The MC-15 coating sprayed in the traditional outer diameter setup can be observed to have a higher microhardness and lower porosity in comparison to the internally sprayed ID90 coating, but its fracture toughness was reduced. The lower microhardness of the ID90 coating can possibly be explained by the reduced amount of $W_2C$ within in the coating in

comparison to the MC-15 coating combined with a greater percentage of porosity.

Specific wear rates were found to higher for the outer diameter coating MC-15 at both the 96N and 240N loads in comparison to the ID90 coating. Data presented in Chapter 4 and Chapter 5 regarding the wear behaviour of the two coatings reveals that cracking can be seen in positions on the worn surface, indicating that brittle fracture plays a role in the mechanism of wear. This means fracture toughness of the coatings plays a vital role in the tribological behaviour of the coatings when tested in this sliding wear setup, as coatings with a higher fracture toughness will be more resistant to the propagation of these cracks therefore heightening their resistance to sliding wear.

## 5.6 Summary of Chapter

In this chapter, WC-Co-Cr coatings were sprayed onto substrates mounted within 3 cylindrical tubes with internal diameters of 70mm, 90mm and 110mm using the ID-HVOF thermal spray torch, in order to investigate the effect of part diameter and therefore stand-off distance on the microstructure, phase composition, mechanical properties and sliding wear resistance of the sprayed coatings.

The coatings sprayed within the different sized tubes differed in phase composition, mechanical properties and resistance to sliding wear. Spraying within the smallest diameter tube produced coatings with the

lowest microhardness and highest porosity. With splats still retaining the shape of the original powder feedstock present within this coating, the low microhardness and high porosity is likely due to particles being unable to accelerate sufficiently when spraying within the smallest tube due to the reduced stand-off distance.

The coating sprayed within the 90mm tube ID90 was found to have the best mechanical properties and lowest wear rates during wear testing, showing the spray parameters used were best optimised for this stand-off distance.

The coating sprayed within the 110mm tube was found to contain lower amounts of $W_2C$ and higher amounts of η-phase carbide $Co_3W_3C$ in comparison to the other coatings. These η-phase carbides are said to form when substrate cooling is insufficient and their presence within the coatings was found to reduce the coating fracture toughness, implying that substrate temperatures possibly were higher during the spray process when spraying the ID110 sample. The higher η-phase carbide content of the ID110 coating resulted in severe crack propagation during wear testing making these coatings not suitable for use in this current state.

The results of this chapter show that spraying WC-Co-Cr coatings onto internal surfaces is viable, however it is apparent that substrate temperature control is of vital importance as substrate overheating can lead to degradation of the coating fracture toughness in particular, which can negatively affect the sliding wear resistance of the coating.

# Chapter 6. Microstructure and sliding wear behaviour of WC-Co/NiCrFeSiB composite coatings for future ID applications

## 6.1 Introduction

As discussed in the literature review, NiCrFeSiB coatings are useful for applications in which resistance to corrosion, wear and heat are required. In particular, the use of NiCrFeSiB powders combined with a reinforcing hard phase such as WC-Co to the powder feedstock have been shown to compensate for the lower hardness of the Ni alloy, leading to an improvement in the sliding wear resistance in the coatings.

It has been previously identified during the literature review that the application of such composite coatings by HVOF thermal spraying is a little researched area, with current studies largely focusing on the erosive wear of these composite coatings. One study did investigate the sliding wear performance of WC-Co/NiCrSiB composite coatings, but the work was missing detailed analysis of the worn surface of the coatings and counterbody materials, meaning the mechanisms of sliding wear are still unknown. In this chapter, composite coatings sprayed from a WC-Co/NiCrFeSiB mixed powder feedstock were subjected to sliding wear testing against two different counterbody materials to assess the coating's performance. Counterbodies of $Al_2O_3$ and WC-Co were used in order to assess the performance of the coatings when contacted against a brittle

ceramic material, alongside a like-on-like style coupling as carried out in the previous chapters.

The effects of spraying a composite powder feedstock with a HVOF thermal spray torch designed for internal surfaces is also currently unknown, meaning the results presented during this chapter may provide a valuable insight into the future application of these composite coatings for an ID-HVOF thermal spray process. The effect on the final sprayed coating of changing the spray parameters is also currently not known; therefore coatings sprayed using two different parameter sets were studied within this chapter in order to provide insight into the effect of the gas flowrate into the torch on the coating performance. Lowering the overall gas flowrate into the torch will reduce the operating cost of the process, improving the economic potential of the process. However, it is currently unclear to what degree this would affect the final coatings.

In this chapter, the effect of changing the gas flowrate into the ID-HVOF thermal spray torch when spraying WC-Co/NiCrFeSiB composite coatings will be investigated. Sliding wear testing against two different counterbody materials will be carried out in order to assess the sliding wear behaviour of the coating against different materials, providing insight into the feasibility of these composite coatings for a potential ID application to provide resistance against sliding wear.

## 6.2 Coating deposition

For the work carried out within this chapter, a commercially available powder feedstock consisting of 50/50wt.% WC-Co/NiCrFeSiB (AMPERIT® 560.090, H.C Starck, Germany) with a nominal powder size of 45/5µm was deposited onto the same AISI 416 stainless steel discs used in the previous chapter using the ID-HVOF thermal spray torch. A traditional outer diameter setup was used in the same configuration as carried out in Chapter 4, as the aim of these experiments was to investigate the feasibility of spraying this composite powder feedstock with the ID-HVOF thermal spray torch for future ID applications. The stand-off distance used when spraying all samples was fixed at 100mm.

Table 6-1 shows the spray parameters used within this chapter; note the ranges of the fuel, oxygen and air flowrates utilised for all samples are shown due to commercial sensitivity.

| **Fuel** | **Input Pressure** | **Flow rate** |
|---|---|---|
| Fuel | 10bar | 200-300 SLPM |
| **Oxidiser** | **Input Pressure** | **Flow rate** |
| Oxygen | 10bar | 100-200 SLPM |
| Air | 10bar | 100-400 SLPM |
| **Combustion Pressure** | **Flame Temp** | **Gas Velocity** |
| 6-8 bar | 2000-3000K | Mach 2-2.5 |
| **Powder Injection Method** | Axial Partially Inside or Outside the Torch | |

**Table 6-1 - Spray parameter ranges used for the samples sprayed within this chapter**

To investigate the effect of spray parameters on the microstructure and therefore consequently the sliding wear resistance of the coatings the total flowrates entering the torch were set at 150L/min and 500L/min, with the exact composition unable to be disclosed. The aim of increasing this input gas flowrate is to lower the temperature of the flame. The coatings sprayed at the low and high input gas flowrates are named NiSF_LF and NiSF_HF respectively throughout the following chapter.

## 6.3 Powder feedstock characterisation

SEM images of the feedstock powder and BSE images showing the cross section of the powder particles is displayed below in Figure 6-1.

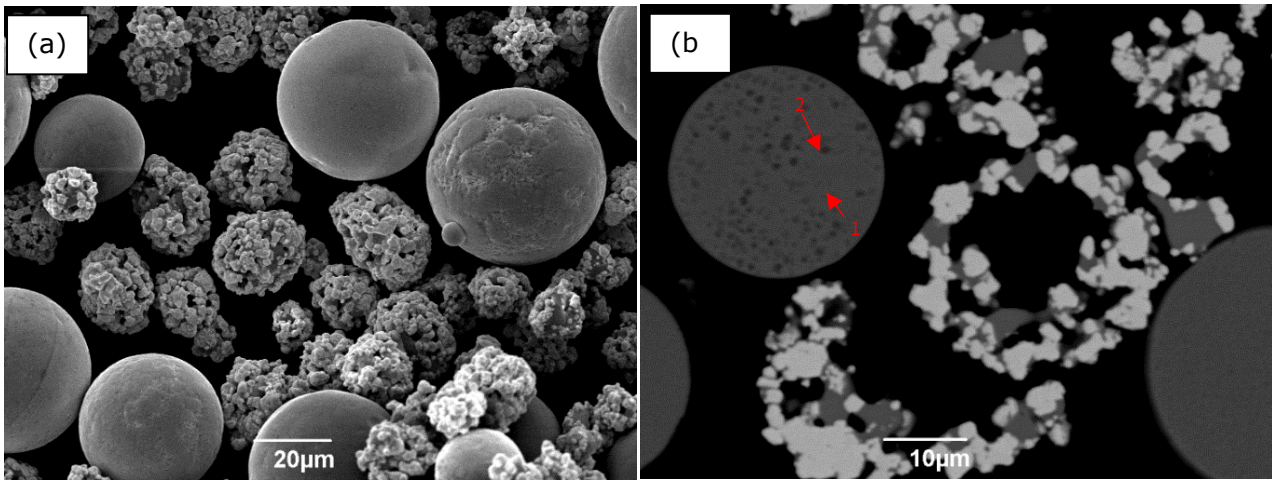


**Figure 6-1 - (a) SEM image of the composite powder feedstock. (b) BSE image of the cross section of powder particles**

The WC-Co particles can be seen as the smaller, roughly spherical shaped particles with an exterior covered in block like grains of WC similar to the WC-Co-Cr powders studied in the previous chapters; meanwhile the Ni alloy can be seen as the larger spherical particles. The BSE images of the powder cross section reveal the WC-Co particles are largely hollow, however in

contrast the Ni alloy particles appear to be non-porous. Two distinct phases exhibiting a separate contrast can be observed within the cross section of these Ni alloy particles, with EDX point scans revealing the composition difference between these regions in Table 6-2. The spots with a darker contrast were found to be rich in Cr, with the Ni content dropping from about 71wt.% in the surrounding areas to 29.5wt.% in the Cr rich region.

| **Location (all in wt.%)** | **C** | **Si** | **Cr** | **Fe** | **Ni** | **B** |
|---|---|---|---|---|---|---|
| Point 1 | 6 | 4.6 | 14.8 | 3.7 | 70.9 | - |
| Point 2 | 11.3 | 1.5 | 35.8 | 2.8 | 29.5 | 19.1 |

**Table 6-2 - Measurements from EDX point scans on the cross section of a Ni alloy particle**

From the SEM images in Figure 6-1, it can be observed that the size of each powder type in the composite feedstock differs significantly. The size distribution of the composite powder feedstock is displayed below in Figure 6-2 and this size difference can be seen. The most common particle sizes detected were at approximate diameters of about 25μm and 44μm and from the SEM images of the composite powder feedstock it can be assumed this corresponds with the sizes of the WC-Co and Ni alloy particles respectively.

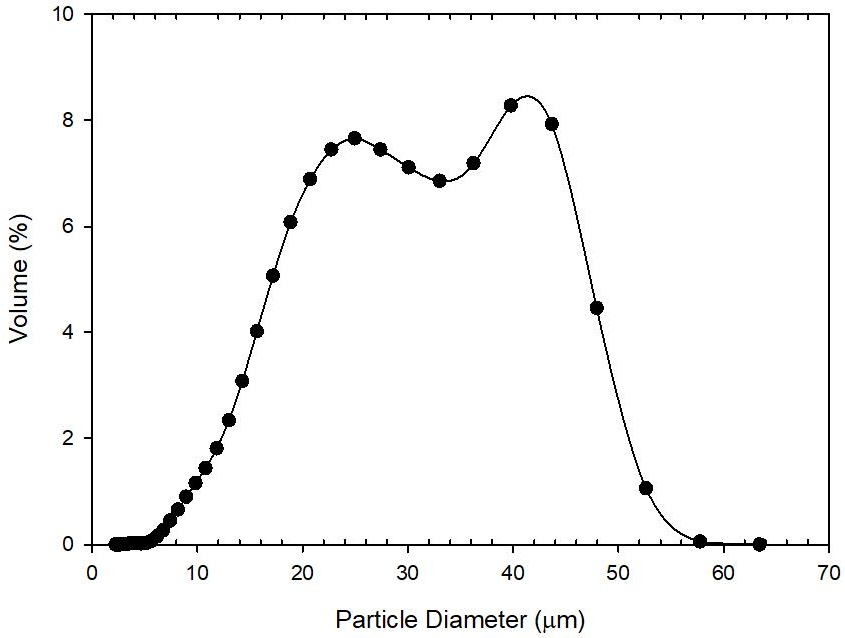


**Figure 6-2 - Particle size distribution of the composite powder feedstock**

The phase composition of the powder feedstock was investigated using XRD, with the resulting diffractograms presented below in Figure 6-3.

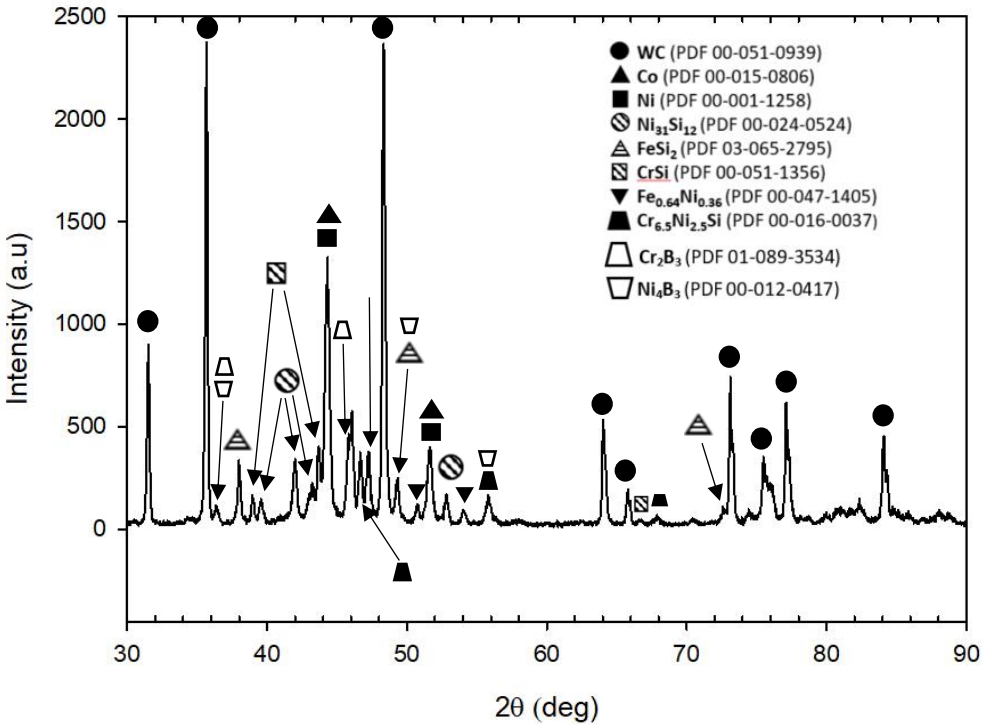


**Figure 6-3 - XRD diffractogram of the composite powder feedstock**

The phases that can be attributed to the WC-Co particles include WC and Co, similar to that seen in other work [58], with the rest of the detected crystalline phases being linked to the Ni alloy particles. The phase composition of the Ni alloy can be observed to be much more complex; apart from the Ni phase, the presence of a number of silicides and borides were detected as seen in other work where similar alloys were studied [123].

## 6.4 Coating characterisation

XRD diffractograms of the as sprayed coatings are displayed in Figure 6-4. Little difference can be observed between the phase compositions of both coatings, indicating that increasing the gas flowrate into the torch had little effect on the phase composition of the coatings. However, a clear difference can be seen in the phase composition of the coatings in comparison to the feedstock powder in Figure 6-4; the presence of a broad hump between approximately $2\theta=37°<2\theta<50°$ can be observed indicating the formation of amorphous or nanocrystalline phases during the spray process.

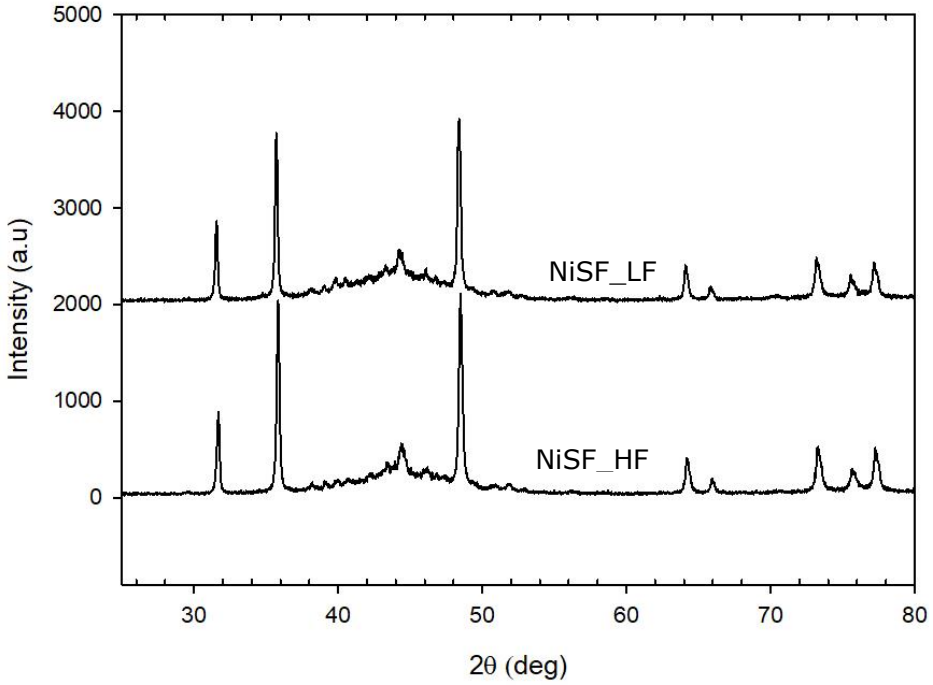


**Figure 6-4 - XRD diffractograms of the as sprayed coatings**

The peaks attributed to minor phases present within the Ni alloy can be seen to have reduced in intensity, as well as being observed to disappear completely at higher 2θ values. It is likely that these minor crystalline phases that were detected in the powder feedstock formed a solid solution during the spray process and were not able to fully recrystallise when the in-flight particle impacted the substrate and solidified. Unlike the coatings studied in the previous chapters, no $W_2C$ or elemental W was detected within the coating microstructure indicating little to no decarburisation of the WC-Co powder occurred during the spray process when spraying under both conditions.

SEM SE and BSE images of the cross sections of the as sprayed coatings are presented in Figure 6-5. Both coatings were found to have densely packed structures containing little porosity. No signs of cracking were

observed, and coatings were found to have good adhesion to the substrate, characterised due to the lack of any cracking or delamination across the coating/substrate interface. The measured thickness of the NiSF_HF and NiSF_LF coatings was 518±11µm and 576±8µm respectively.

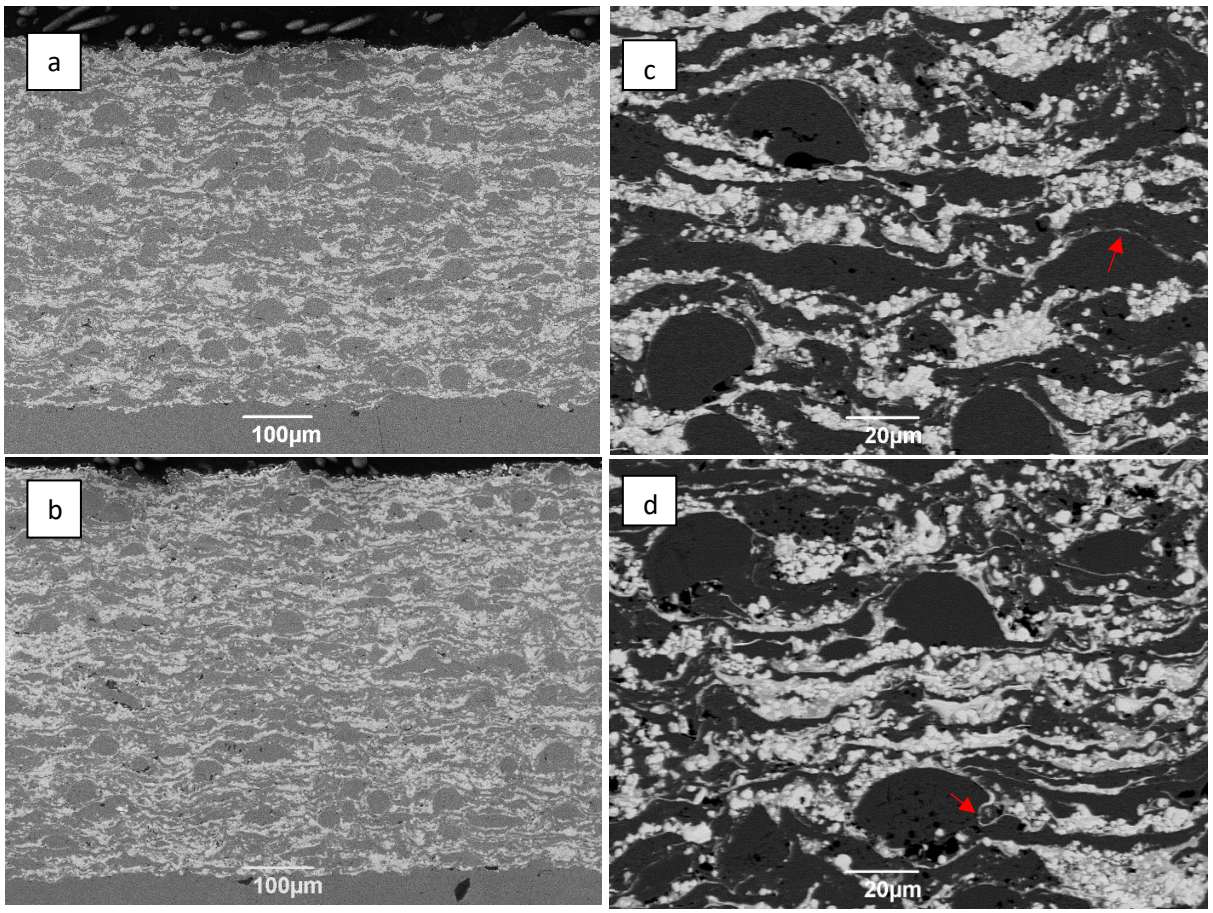


**Figure 6-5 - (a,b) SEM SE images of the NiSF_HF and NiSF_LF coating cross section. (c,d) BSE images of the coating microstructures. Intersplat phases are marked on the images with a red arrow.**

The splats of Ni alloy and WC-Co can be observed throughout the microstructure, with the WC-Co splats having a brighter contrast. Many of the darker Ni alloy particles can be observed to have retained their original spherical shape when being deposited onto the substrate. The approximate diameter of these spherical splats within the microstructure of both coatings was measured, with the average diameter within the NiSF_HF and NiSF_LF

coatings being found to be 41±11μm and 37±7μm respectively. The Cr rich areas that were observed in Figure 6-1 can also be seen throughout the coating cross section within some of the splats originating from Ni alloy particles. The relative volume percentage of WC-Co splats within the microstructure was measured for each coating, with the NiSF_HF and NiSF_LF and 30.3±2.1% and 30.9±1.1% respectively, with the remaining percentage consisting of either Ni alloy phase or porosity. This indicates that the amount of WC-Co powder deposited within each coating is comparable.

Thin string like phases with a brighter contrast can be seen throughout the microstructure of both coatings and are marked on the SEM image in Figure 6-5 with red arrows.

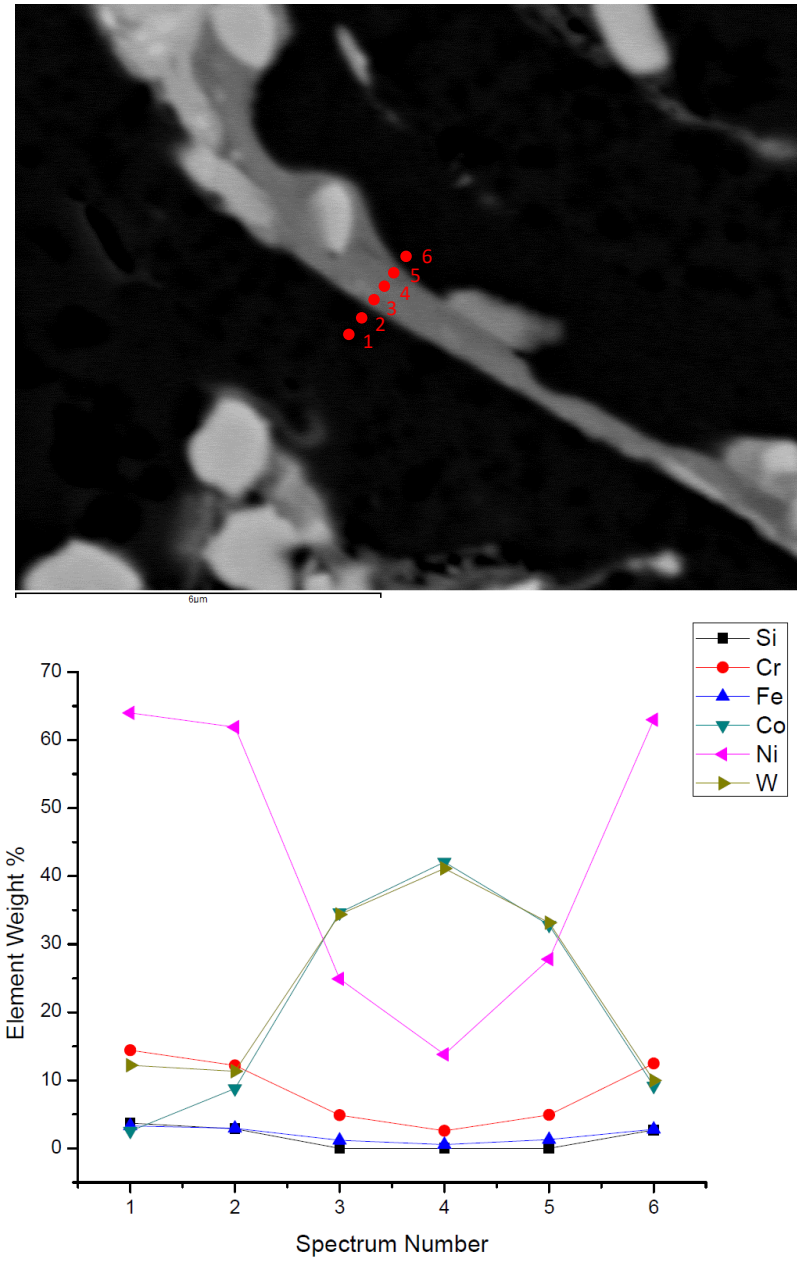


**Figure 6-6 - EDX line scan across the intersplat phase marked in Figure 65 seen in the cross section of the NiSF_HF coating**

The results from EDX point scans across one such area are shown in Figure 6-6. The surrounding darker area was found to contain a large weight

percentage of Ni (>60wt.%) with little W and Co (<15wt.%). The brighter contrast of the marked areas indicates a higher atomic density in these areas in comparison to the Ni alloy and EDX point scans across these features indeed reveal a large W content of up to 40wt%. The presence of Ni was still detected from the point scans carried out within the bright region, with a spot in the centre found to contain approximately 15%wt. Ni.

The microhardness, indentation fracture toughness and porosity of the two coatings are displayed below in Table 6-3.

| **Sample** | **Microhardness (HV0.3)** | **Fracture Toughness $K_{IC}$ ($MPa.m^{0.5}$)** | **Porosity (%)** |
|---|---|---|---|
| **NiSF_HF** | 926±83 | 4.5±0.2 | 0.3±0.1 |
| **NiSF_LF** | 762±112 | 4.8±0.5 | 1.3±0.2 |

**Table 6-3 - Mechanical properties of the two coatings**

NiSF_HF was found to have a higher microhardness than the NiSF_LF coating, while its fracture toughness was slightly lower. However, with the error from the measurements taken into account, it is likely that the fracture toughness of the two coatings is similar. A small degree of porosity can be observed in both coatings, however it was found to be more prominent in the NiSF_LF coating.

## 6.5 Sliding Wear testing

The coatings within this chapter were subjected to sliding wear testing using the microtribometer 10 N load setup described in Section 3.4.1, with a sliding distance and speed of 500m and 0.16m/s used. To assess the wear behaviour of the coatings when contacted against brittle ceramic materials and like on like cermet materials, spherical counterbodies of sintered WC-Co and $Al_2O_3$ were used as the counterface materials. Prior to the wear testing, the surface roughness ($R_a$) of the coatings was measured by profilometry to lie in the range of 0.02–0.05μm, with the $R_a$ of the counterbodies quoted by the manufacturer to be <0.02μm.

The specific wear rates of the two coatings tested against both counterbody materials and the specific wear rate of the respective counterbodies is displayed in Figure 6-7. It was determined that the NiSF_LF coating sprayed using the lower gas flowrate into the torch wore more against both counterbody materials than the NiSF_HF coating. The NiSF_HF coating wore at rate of $5.00x10^{-7}mm^3/Nm$ against the WC-Co counterbody and $1.10x10^{-6}mm^3/Nm$ against the $Al_2O_3$ ball; meanwhile the NiSF_LF coating wore at rates of $5.43x10^{-7}mm^3/Nm$ and $1.23x10^{-6}mm^3/Nm$ against these two counterbody materials. Both of the coatings were observed to suffer material loss at a faster rate when contacted against the ceramic $Al_2O_3$ counterbody in comparison to the sintered WC-Co ball, with the specific wear rate increasing by 120% and 127% for the NiSF_HF and NiSF_LF coatings against $Al_2O_3$ in comparison to WC-Co.

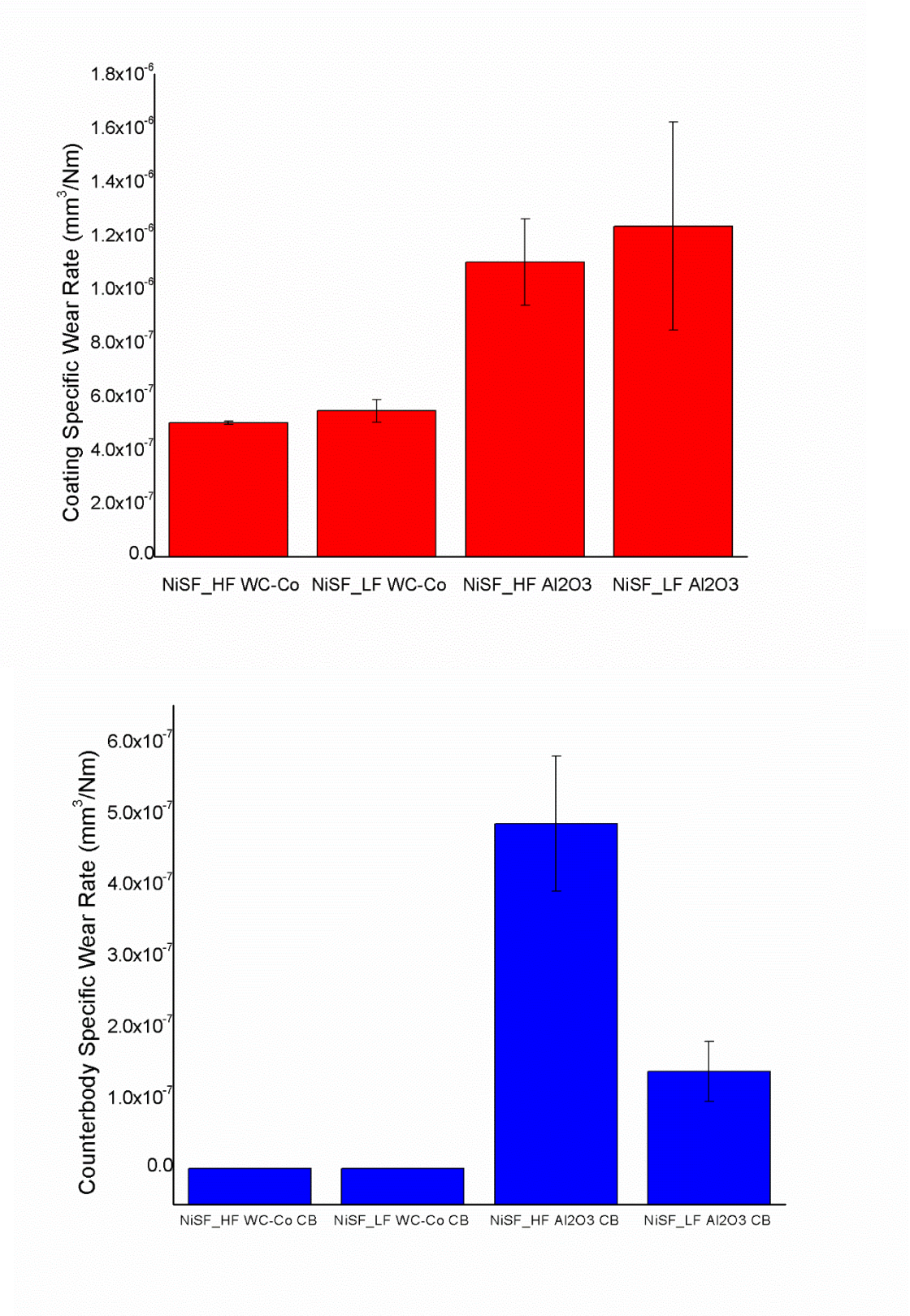


**Figure 6-7 - Top: Specific wear rates of the two coatings against both counterbody materials. Bottom: Counterbody specific wear rates**

The sintered WC-Co counterbody was observed to undergo no noticeable wear during the sliding wear testing against both coatings, with the contact surface of the ball retaining its spherical shape. In contrast, the contact surface of the $Al_2O_3$ ball was observed to suffer material loss with a flat surface forming on the balls, with higher specific wear rates measured when wearing against the NiSF_HF coating. The coefficient of friction μ was monitored throughout the wear tests, with the frictional response of the two coatings against both counterbodies presented below in Figure 6-8.

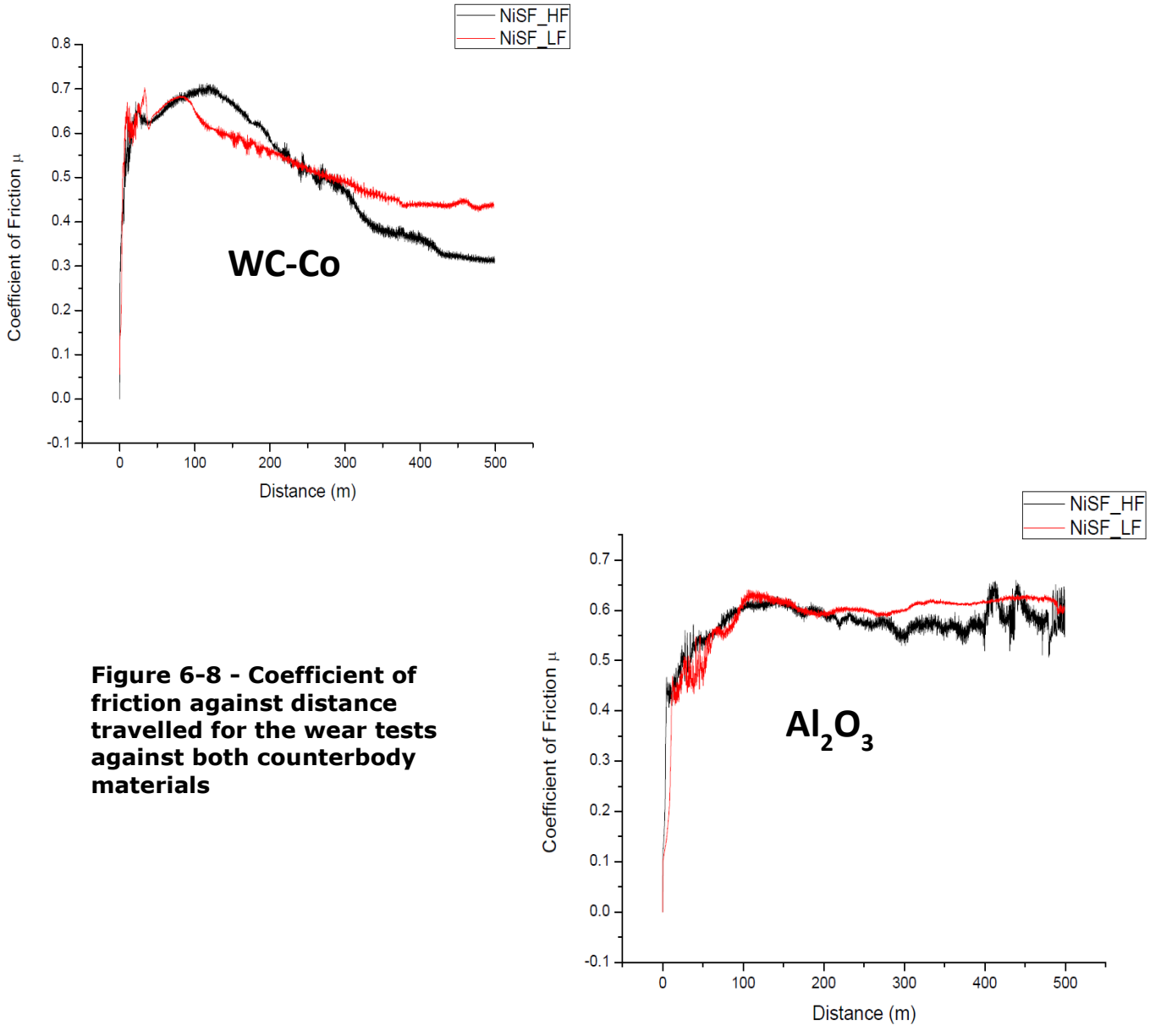


**Figure 6-8 - Coefficient of friction against distance travelled for the wear tests against both counterbody materials**

Against both counterbody materials, the break-in period lasts for approximately the first 100m of the test, with large fluctuations seen in the coefficient of friction. For the tests against the sintered WC-Co counterbody, the coefficient of friction was observed to decline during the test from a maximum of about 0.7 down to below 0.5. In contrast μ was observed to remain relatively constant following the break in period when contacting the coatings with the ceramic $Al_2O_3$ counterbody. The final value of μ was seen to be higher for both coatings tested against $Al_2O_3$ in comparison to WC-Co. As the frictional response of both coatings during the wear tests was found to be similar for each counterbody material, this suggests little to no difference in the wear mechanisms taking place for each coating.

Low magnification SEM images of the worn surfaces of both coatings are shown in Figure 6-9.

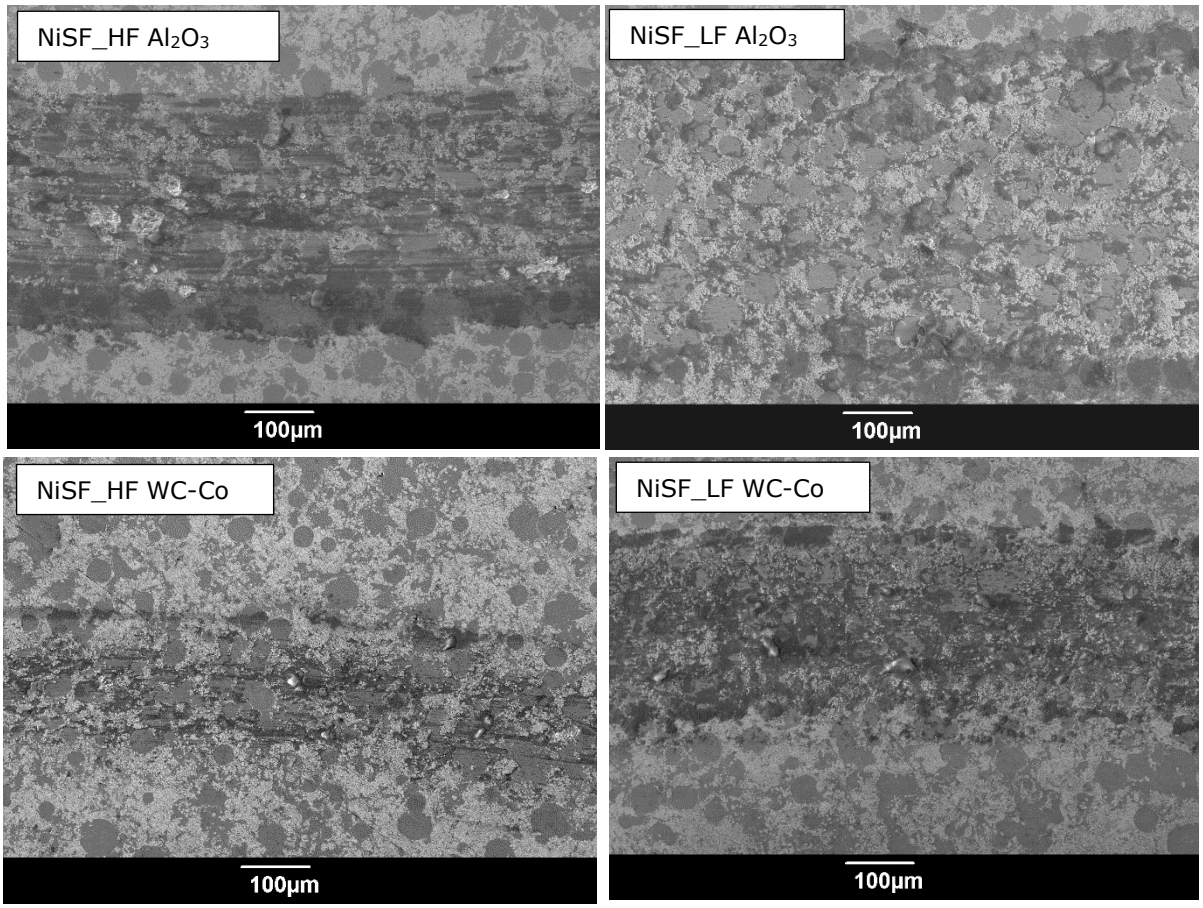


**Figure 6-9 - Low magnification SE SEM images showing the plan view of the worn surfaces of the coatings tested against both counterbody materials. Note the greater width of the tracks worn against the Al2O3 counterbody.**

The widths of the wear tracks were measured to be approximately 171±3µm and 276±9µm for the NiSF_HF and NiSF_LF coatings tested against WC-Co and 329±16µm and 456±7µm for these coatings against the $Al_2O_3$ counterbody. This is consistent with the coating specific wear rates presented in Figure 6-7, with the NiSF_LF coating having a wider track width and higher measured material loss.

SEM BSE and SE images of the worn surfaces of the coatings tested against the WC-Co counterbody are displayed in Figure 6-10. Some signs of small

cracks can be seen around areas of spherical shaped Ni alloy splats and these are marked on the image with an arrow.

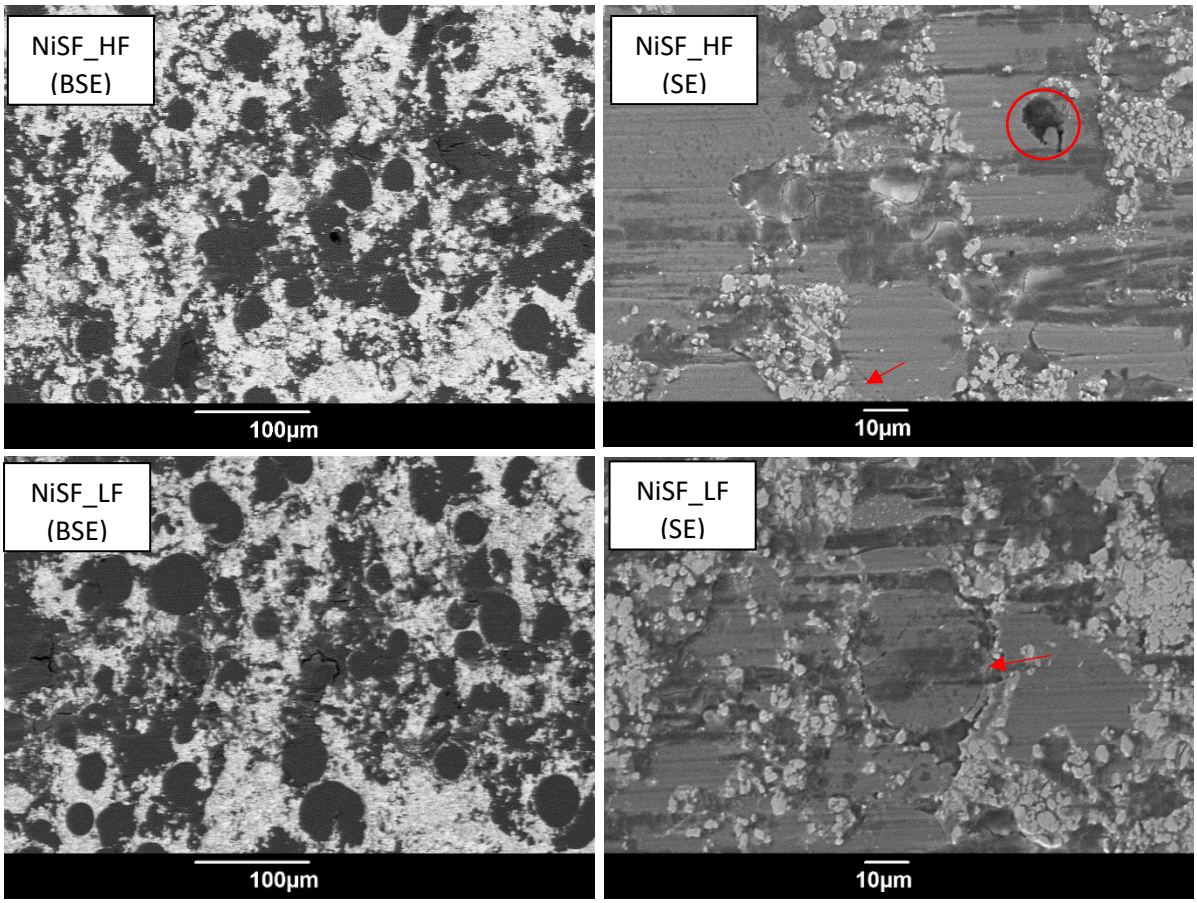


**Figure 6-10 - SEM BSE and SE images of the plan view of the worn surfaces of the coatings tested against the WC-Co counterbody. Cracking originating from the interphase between the cermet and Ni alloy splats and example areas of oxidised material are marked with arrows and dots respectively**

Some small pores can be observed on the worn surface, likely areas in which pull out of WC has occurred; an example is marked with a circle on the image. Scratches in the direction parallel to the movement of the counterbody can be seen on the worn surface, covering both WC-Co and Ni alloy rich areas. Areas with a darker contrast can be seen on the SEM images where cracks perpendicular to the direction in which the counterbody moved are present, with EDX point scans in these areas

detected a large concentration of oxygen meaning these are likely oxides. Small bright dots can be seen on surface in the SE images with a similar contrast in BSE to the WC grains but with a much smaller size. These are likely tungsten rich debris scattered across the worn surface originating from pulled out WC grains, or the abrasive wear of the WC phase.

SEM BSE and SE images of the worn surfaces of the coatings tested against the $Al_2O_3$ counterbody are displayed in Figure 6-11. Features similar to that seen on the samples worn against the WC-Co counterbody can be observed on the worn surfaces with scratches, small cracks between Ni alloy splats (marked with arrows on the image) and oxidised areas (marked with a dot on the image) all present. The tungsten rich debris can also again be observed scattered across the worn surface. Overall, when testing against both counterbody materials, little difference can be observed between the worn surfaces, implying the mechanism of wear is similar regardless of counterbody type with only the rate of wear changing.

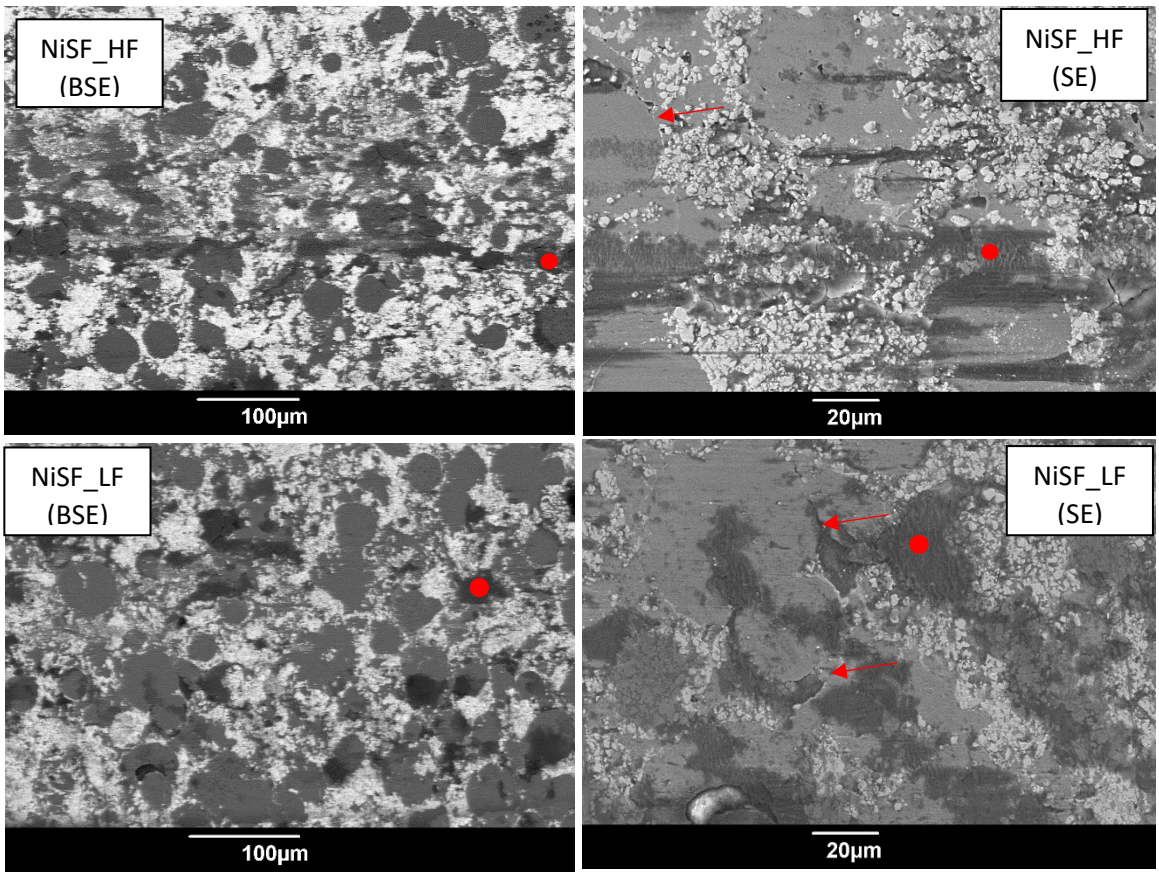


**Figure 6-11 - SEM BSE and SE images showing the plan view of the worn surfaces of the coatings tested against the $Al_2O_3$ counterbody. Cracking originating from the interphase between the cermet and Ni alloy splats and example areas of oxide are marked with an arrow and dot respectively.**

In order to analyse the oxide phases formed on the worn surface of the two coatings, Raman spectroscopy was employed with the resulting Raman spectra measured on the worn NiSF_HF coating presented in Figure 6-12. Little difference was observed in the wear mechanisms between the two coatings and as a result, presenting only the Raman spectra from this coating is required.

Raman spectroscopy reveals peaks attributed to $WO_3$, $CoWO_4$ and a Ni-W based oxide with the Raman spectra of the pure materials used as the reference from other studies [124,125]. Little difference was seen between the coatings tested against the sintered WC-Co and $Al_2O_3$ counterbodies

indicating the oxides forming on the surface are likely forming via a similar mechanism.

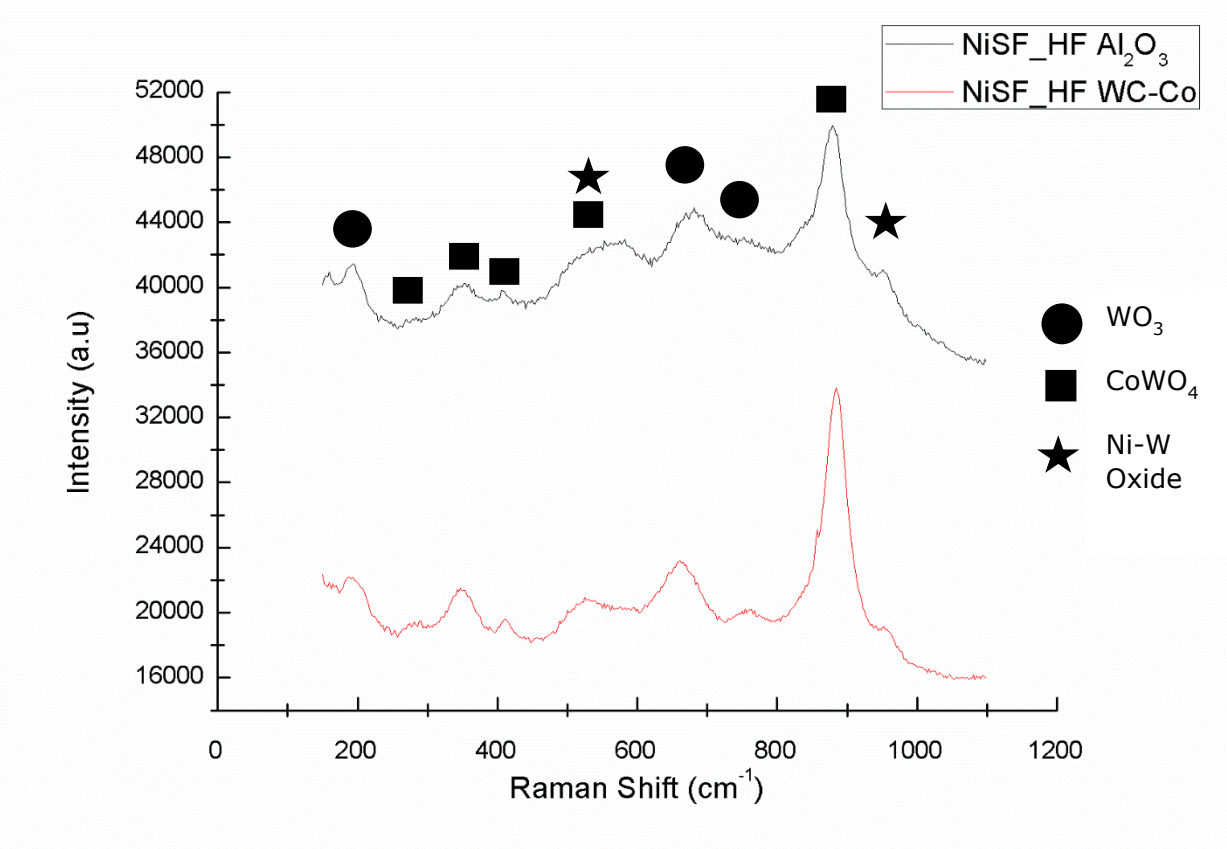


**Figure 6-12 - Raman spectra measured from the worn surface of the NiSF_HF coating worn vs. both counterbody materials**

SE and BSE SEM images of the worn surface of an $Al_2O_3$ ball used in the wear test against the NiSF_HF coating are displayed in Figure 6-13. Low magnification images show a "smoothed out area" which displays a brighter contrast than the bulk material in the BSE images. EDX point scans in this region detected a large concentration of elements present in the coating material such as Ni, W and Co implying material transfer between the coating and counterbody took place during the wear test. Cracking can be seen surrounding the circular worn cap implying brittle fracture of the ceramic counterbody took place during the test. Higher magnification

images in the region marked on the image with the red box expose a worn surface characteristic of an area in which brittle fracture mechanisms have occurred, similar to that seen in other work [126]. Small areas with a brighter contrast can also be seen in the higher magnification BSE images, with EDX again showing the presence of elements originating from the coating. Due to the negligible wear of the WC-Co counterbodies, these were imaged.

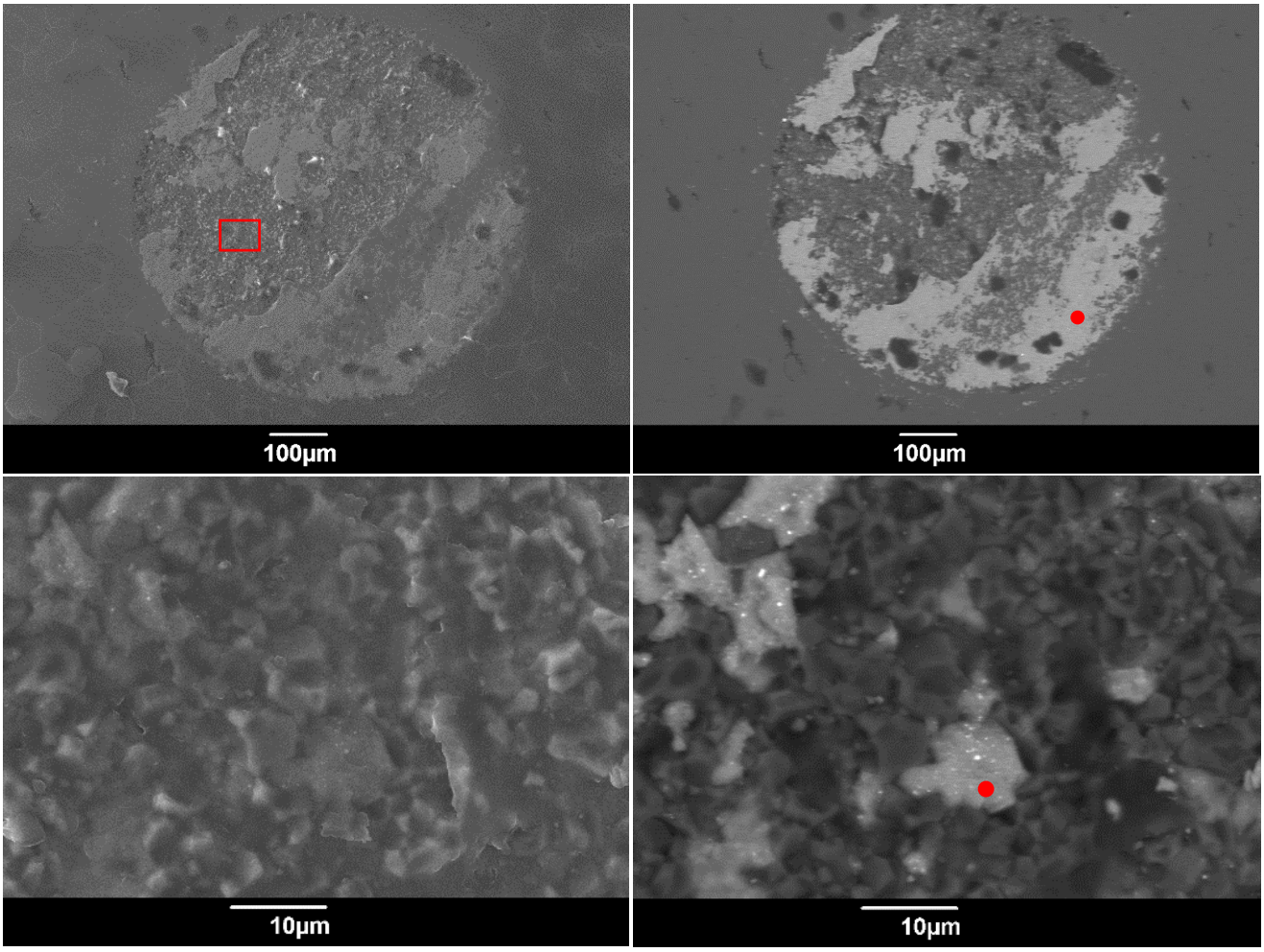


**Figure 6-13 - SE and BSE SEM images of the worn surface of the $Al_2O_3$ ball. Spots marked with a red circle indicate positions at which EDX point scans were performed and the red box shows the approximate location of the higher magnification images.**

## 6.6 Discussion

### 6.6.1 Powder and coating characterisation

Throughout the microstructure of both coatings, spherical shaped splats of Ni alloy retaining the morphology of the starting powder can be observed while in contrast, the WC-Co splats appear well flattened. From this observation, it may be that the spray parameters used when spraying both coatings lead to favourable in-flight characteristics for the WC-Co particles but less so for the larger Ni alloy particles. The SEM images of the composite powder feedstock in Figure 6-1 show that the Ni alloy particles are non-porous and vary in size, with the diameter of these particles shown to vary between 23 and 45μm. If a constant spherical morphology is assumed, the difference in volume between the smallest and largest alloy particles would vary by almost 750%. This would likely lead to large temperature variations of these particles in flight, with the larger heavier particles requiring a greater heat input to reach the optimum temperature at which the degree of particle melting required for HVOF thermal spray occurs. Furthermore, an increased amount of kinetic energy is required for the larger heavier Ni alloy particles to reach the high in-flight velocities needed to ensure sufficient flattening on impact with the substrate. This means that it is expected that the larger Ni alloy particles will not only be at lower temperatures in flight, but also have lower in-flight velocities too in comparison to smaller, lighter particles of the same material. Consequently, the under deformed spherical shaped splats throughout the coating were

determined to be in the size range above 37μm diameter, meaning this effect only occurs with the larger Ni alloy particles due to the reasons stated above. It has also been previously shown using in-flight particle diagnostic and CFD simulation methods that insufficient flattening of the sprayed particles on impact with the substrate results in coatings with a higher porosity [127,128].

When comparing the microstructure and mechanical properties of the two coatings NiSF_HF and NiSF_LF, evidence shows that it is likely that vulnerabilities within the coating originating from the under deformed splats are more prevalent in the coating sprayed at the lower input gas flowrate NiSF_LF. The undeformed particles throughout the microstructure were seen to be smaller in diameter compared to those within the NiSF_HF coating, implying that using the spray parameters utilised when spraying the NiSF_HF coating lead to increased acceleration of the in-flight particles, with larger particles reaching a sufficiently high velocity to deform on impact to create a more ideal lamellar microstructure. Furthermore the NiSF_HF coating was determined to have a lower porosity and higher microhardness than the other coating, which is likely linked as increased porosity has been shown to lead to a reduced coating microhardness in HVOF thermal spray coatings [11].

It was previously stated that the aim of increasing the gas flowrate into the torch when spraying the NiSF_HF coating was to reduce the temperature of the flame. However, due to the increased deformation of the Ni alloy

particles within the NiSF_HF coating and the effects this has such as a reduction of porosity and an increase in coating hardness, it appears raising input gas flowrate into the torch has a significant effect on the in-flight particle velocity. The coating sprayed at the lower gas flowrate and therefore supposedly hotter flame did not contain any phases associated with overheating of the particles in flight, such as $W_2C$ or W meaning that the flame temperature is not an issue when using either spray parameter set. However, assessing the effect of in-flight temperature without in flight particle diagnostic tools is not possible.

Increasing the input of oxidising and diluting gases and fuel into the torch may lead to an increase in the combustion chamber pressure, due to a greater mass of material entering the fixed combustion chamber volume per unit time [20]. Combustion chamber pressure has been shown to be directly linked to in-flight particle velocity in other work [23,129] and can be increased by raising the fuel flowrate into the torch [130]. Higher combustion chamber pressures will lead to greater in-flight particle velocities due to the larger pressure drop between occurring when the gas leaves the combustion chamber, resulting in increased gas acceleration.

### 6.6.2 Sliding wear behaviour

In the sliding wear tests against both counterbody materials, the NiSF_HF coating was found to wear at a lower rate in comparison to the NiSF_LF coating. The better resistance to sliding wear of the NiSF_HF can likely be attributed to the greater microhardness of this coating, with the increased

resistance to localised deformation on the coating surface provided by the greater hardness resulting in lower sliding wear, similar to results seen in other work with HVOF thermal spray coatings [131].

The change in the friction coefficient against distance travelling within the wear test can be seen to be similar for both coatings against each counterbody material. In addition, inspection of the worn surfaces revealed similar features present on the worn surfaces of both coatings, such as WC grain pull outs, scratch marks and cracking originating from the perimeter of spherical shaped splats of Ni alloy. SEM images of the coating cross section reveal that porosity is often present in these areas adjacent to the spherical Ni alloy splats and using principles of linear elastic fracture mechanics it is likely stresses concentrate in the coating at these pores, leading to cracks propagating from these regions. Consequently, it can be assumed that the mechanism of wear taking place in each coating is comparable.

A significant difference in specific wear rate can be observed when the coatings were worn against the two separate counterbody materials, with both coatings wearing at a higher rate against the $Al_2O_3$ counterbody.

Raman spectroscopy on the worn surfaces of both coatings reveal the presence of $WO_3$, $CoWO_4$ alongside Ni-W based oxides. The pull out of the WC grains evidenced by the small holes left on the worn surface results in loose WC particles scattered across the worn surface. These may get trapped between the coating surface and the moving counterbody leading

to wear via a three body abrasion mechanism, described in Section 2.1.2; this can be seen in form of the scratch marks present across the worn surfaces of both coatings. Furthermore, these trapped WC particles may begin to react with atmospheric oxygen due to the heat generated from the sliding contact resulting in the formation of $WO_3$. The abrasion of the coating surface results in the production of debris originating from WC-Co and Ni alloy splats and the oxidation of each of these debris types could explain the formation of the $CoWO_4$ and Ni-W oxides during the wear test.

When contacted against both coatings the WC-Co counterbody was found to suffer negligible wear; however, in comparison the $Al_2O_3$ balls were seen to undergo wear leading to the formation of a flat contact surface with features characteristic of brittle fracture observed. While it is said the two materials are comparable in terms of hardness, sintered WC-Co has a much higher fracture toughness with values such as 10.2MPa.$m^{1/2}$ quoted by others [132] in comparison to the fracture toughness of $Al_2O_3$ quoted at about 5MPa.$m^{1/2}$ [133]. The higher fracture toughness of the WC-Co ball meant the material could resist brittle fracture during the wear test, resulting in negligible wear.

Wear of the $Al_2O_3$ ball during test resulted in the formation of a flat surface due to the round edge of the ball being worn down, leading to an increase in the contact area between the coating and $Al_2O_3$ during the wear test. In some cases this should be expected to actually lead to less wear, due to the increase in the surface area of the contact surface leading to a reduction

in the contact pressure; however as seen in Figure 6-7 an increase in wear was observed for both coatings tested against $Al_2O_3$ in comparison to WC-Co. This can possibly be explained as follows: as the contact surface on the $Al_2O_3$ ball increases in size throughout the test, more abrasive particles can become trapped between the coating and counterbody leading to heightened wear by abrasion in the system [134]. Material originating from the coating can be observed embedded in the worn surface of the $Al_2O_3$ balls in Figure 6-13 providing evidence for this explanation.

The behaviour of the coefficient of friction throughout the test was observed to differ depending on the counterbody material used, with the coefficient of friction seen to reduce during the wear test with the WC-Co counterbody but not the $Al_2O_3$ counterbody. The formation of $CoWO_4$ and $WO_3$ has been stated in other work to act as a solid lubricant in the system, lowering the coefficient of friction [135,136]. The double oxide $CoWO_4$ is composed of both CoO and $WO_3$ which have significant ionic potential differences, which has been said to promote anti-friction properties [135,137].

The same oxides are present on the surface of the coatings worn against both counterbody materials, however the coefficient of friction only reduced in the coupling with the WC-Co ball. This difference in behaviour can be explained by considering both the wear of the ball and the coating as the wear of the $Al_2O_3$ ball was seen to occur by brittle fracture of the material while the WC-Co ball suffered negligible wear. The occurrence of brittle fracture results in increased frictional forces, due to the fractures providing

an additional mechanism for dissipation of energy in the area of the sliding contact [5]. This effect could counter lubricating effects provided by the formation of the $CoWO_4$ and $WO_3$ oxides during the wear test, resulting in a relatively stable coefficient of friction. However, in the wear coupling in which the counterbody material is seen not to undergo sever wear it appears the lubricating effect provided by the formation of oxides on the worn surface occurs, leading to a reduction in the coefficient of friction.

### 6.6.3 WC-Co/NiCrFeSiB coatings for future ID-HVOF thermal spray processes for wear resistance

Overall it appears while the operating costs of the spray process can be reduced by lowering the gas flowrate into the thermal spray torch, the quality of the coating is reduced in doing so with the NiSF_LF coating exhibiting inferior hardness and sliding wear resistance. However, performance was not affected significantly, meaning for some applications using the lower input gas flowrate may be acceptable for the required design.

The material loss of the best performing coating sprayed within this chapter NiSF_HF was measured at $4.99\pm0.06x10^{-7}mm^3/Nm$ against the WC-Co counterbody and $1.10\pm0.16x10^{-6}mm^3/Nm$ against the $Al_2O_3$ ball. For comparison, unlubricated sliding wear tests were carried out on WC-Co-Cr coatings sprayed by two widely known commercially used thermal spray systems, a liquid fuelled HVOF torch (JP-5000, Praxair, USA) and high velocity air fuel (HVAF) thermal spray (M3, UniqueCoat Technologies, USA). At a 10N load against a $Al_2O_3$ ball with a 6mm diameter, the specific wear

rates were determined to be approximately $6x10^{-8}mm^3/Nm$ for the liquid fuelled thermal spray coating and $3x10^{-8}mm^3/Nm$ for the HVAF thermal spray coating [49]. Both WC-Co-Cr coatings were determined to have a microhardness in excess of 1200 HV0.3 and it is likely that this difference in coating hardness can largely explain the difference in specific wear rate between the WC-Co-Cr coatings and the composite coatings studied within this chapter. While the WC-Co/NiCrFeSiB coatings studied within this work suffered material loss at an order of magnitude higher than a comparative WC-Co-Cr sprayed by a modern HVOF thermal spray torch, the composite coatings still suffered wear that can be described as mild [5], meaning they show decent potential as wear resistant coatings for low load applications.

It has been shown that many of the vulnerabilities within the composite coatings studied throughout this chapter originate from insufficient in-flight acceleration of larger Ni alloy particles during the spray process. Due to the smaller size and porous structure of the WC-Co particles in the composite feedstock, these particles likely possess a higher surface area to volume ratio meaning the efficiency of heat transfer between the hot gases and the in-flight particles. Meanwhile in contrast the larger, solid Ni alloy particles would likely have slower heating rates. The specific heat capacities of the two materials has been estimated using empirical relationships from other sources at a range of temperatures [138,139], and it was observed that the specific heat capacity of the Ni alloy is almost twice as large as that of WC-Co, meaning the effect of size on heating rate is even more pronounced when considering the Ni alloy particles in comparison to WC-Co, as a

greater energy input is required to increase the material's temperature per unit mass. This difference in particle heating rates means it is likely extremely challenging to optimise the spray parameters in order to achieve the best out of both materials in the composite feedstock, as raising the flame powder to sufficiently melt the NiCrFeSiB particles would result in increased heating of the WC-Co particles, likely leading to decarburisation of the WC phase.

When considering ID-HVOF thermal spray processes it is likely that the torch will have to operate at very short stand-off distances meaning this optimisation process may be even more difficult to achieve. When applying coatings on the inside of a cylindrical tube with a 70mm internal diameter as carried out in the previous chapter, particle acceleration is required to be higher than that of the particles deposited within this work at the 100mm stand-off distance.

For future applications of this composite coating for internal surfaces, one possible solution to improve the coating quality could be to use a composite powder feedstock with a narrower particle size range, including finer Ni alloy particles. This may reduce the differences between the rates of heating of the two materials, allowing for easier optimisation of the spray parameters. Furthermore, the use of smaller Ni alloy particles would also lead to greater rates of acceleration in the spray process which as discussed may improve the performance of the final coating, particularly when operating at shorter stand-off distances.

Increasing the overall gas flowrate into the torch was seen to improve the properties of the sprayed coatings but comes with the issue of higher operating costs for the coating manufacturer. The economics behind the application of thermal spray coatings is beyond the scope of this work, however in this case using this method to improve coating properties will result in greater operating costs due to the higher flowrates of gas required. Depending on the application of the sprayed coating, increasing the microhardness of the coating to high levels by increasing gas flowrate may not be needed; therefore it will come down to a case by case basis whether or not the extra operating costs are worth spending. The increased operating costs may be necessary when applying coatings at very low stand-off distances in future ID HVOF thermal spray processes however, as the greater combustion chamber pressure brought on by the higher overall gas flowrates into the torch will lead to more rapid acceleration of the in-flight particles helping to negate short stand-off distances.

## 6.7 Summary of chapter

In this chapter, a composite powder feedstock containing a 50/50 mixture of WC-Co/NiCrFeSiB was sprayed under two different spray conditions, with one condition having higher overall gas flowrates in order to investigate the effects on the coating microstructure, mechanical properties and sliding wear resistance.

It was observed that increasing gas flowrate resulted in coatings with lower porosity and higher microhardness, while fracture toughness remained

similar. The improved microhardness led to these coatings showing smaller rates of material loss during the sliding wear tests against both WC-Co and $Al_2O_3$ counterbodies, in comparison to coatings sprayed with the reduced gas flowrate. Both coatings suffered higher rates of material loss against $Al_2O_3$ compared to WC-Co, due to the wear of the ceramic ball increasing during the test, leading to increased wear from abrasion due to embedded coating material stuck in the worn counterbody surface.

Ni alloy splats that had retained their original spherical shape could be seen throughout the microstructure of both coatings; however, these features were measured on average to be larger in size within the coating sprayed at the higher gas flowrate. The presence of such features is likely related to insufficient in-flight particle velocity, with the average larger size of the undeformed splats when spraying using higher flowrates indicating a greater proportion of the particle feedstock is in the size range allowing sufficient acceleration during spraying. It is probable that the reduced microhardness, higher porosity and therefore worse sliding wear resistance of the coating sprayed using lower gas flowrates is also related to lower in-flight particle velocities.

For use in future ID-HVOF thermal spraying of composite powder feedstocks, it is recommended to use to a mixture of two materials with a similar particle size range to make the optimisation of spray parameters easier, with the finer the particle feedstock the better.

# Chapter 7. Conclusions and recommendations for future work

## 7.1 Overall Conclusions

The work throughout this thesis has been carried out to meet the main aims and objectives of this work listed in Section 1.1. From the results previously presented, the following conclusions can be made.

In Chapter 4, WC-Co-Cr powder feedstocks with differing WC grain sizes and particle size ranges were sprayed using an ID-HVOF thermal spray torch. It was determined that spraying a powder feedstock with a reduced WC grain size resulted in a coating with a reduced microhardness and fracture toughness. This nanostructured coating was seen to undergo the highest amount of wear under high load conditions, likely due to its inferior mechanical properties. Due to these results, this powder was not selected for the following ID thermal spray experiments. In comparison, the selection of a powder with a larger carbide grain size but reduced particle size range produced a coating with the highest microhardness of all coatings tested within this study. The results of this study show that utilising a particle feedstock with a reduced particle size range when spraying with this ID-HVOF thermal spray system comes with no significant disadvantages. Due to the inherent advantages for ID-HVOF thermal spraying of a reduced powder size discussed in Section 2.4, this powder feedstock was carried forward to be used in the internal diameter spraying experiments.

Chapter 5 presents a study in which the previously selected WC-Co-Cr powder was sprayed onto the internal surface of cylindrical parts using the ID-HVOF thermal spray torch. Different spray runs were conducted, applying coatings within parts with 3 separate internal diameters to provide insight into the effect of part diameter and therefore stand-off distance on the microstructure and sliding wear resistance of the sprayed coatings. It was found that the coatings sprayed within the 3 separate sized parts differed in phase composition, mechanical properties and sliding wear resistance. Coatings sprayed within the smallest 70mm part were found to have the lowest microhardness and highest porosity, likely due to the short stand-off distance resulting in insufficient in-flight particle acceleration. The coating sprayed within the 90mm part was found to have the best mechanical properties and lowest wear rates, meaning the spray parameters used were best optimised for this particular stand-off distance. The coating sprayed within the 110mm part was seen to suffer severe sub-surface cracks following the sliding wear testing. This was likely due to the increased amounts of η-phase carbide $Co_3W_3C$ found within the microstructure in comparison to the other coatings, whose presence has been shown to reduce fracture toughness. This phase has been shown to form when substrate cooling is insufficient, showing the importance of controlling the temperature of the substrate during ID spraying processes. Overall however, the results of Chapter 5 prove that wear resistant WC-Co-Cr coatings can be applied using HVOF thermal spraying on parts with an

internal diameter as low as 70mm, showing that this process could be potentially applied for commercial use in the future.

In Chapter 6 WC-Co/NiCrFeSiB coatings were sprayed using the ID-HVOF thermal spray torch at a stand-off distance of 100mm to simulate coating an internal surface. 2 different spray parameter sets were used, one with a higher overall gas flowrate into the torch. It was found that raising the gas flowrate resulted in coatings with a lower porosity and higher microhardness, while the fracture toughness remained similar. As a result of these improved properties, the coating sprayed at the greater gas flowrate suffered a reduced amount of material loss during sliding wear testing. This was likely due to the higher combustion chamber pressure caused by the higher gas flowrate leading to a greater rate of in-flight particle acceleration and therefore velocity at the time of impact with the substrate. The results of this chapter show that the use of such mixed powder feedstocks is viable when using this ID-HVOF thermal spray system, proving that their use could be potentially used in the future. However, it is likely that the coating properties could be improved by using a mixture of materials that are closer in particle size and therefore this is recommended for any future application.

## 7.2 Future work

The following section will outline any future work relevant to the main topic of this thesis that would further enhance the arguments and conclusions presented within this study.

Results in this work revealed that using nanostructured WC-Co-Cr powder did not result in an increase of the coating hardness, which was said to contradict statements by others. Spraying the same nanostructured WC-Co-Cr powder using different spray parameter sets with the ID-HVOF thermal spray torch would provide insight into whether the performance of nanostructured coatings could be further improved. The use of a nanostructured WC-Co-Cr powder with a reduced overall particle size could also be used as a powder feedstock for future work, as reduced particle sizes were shown to lead to improvements in the coating sliding wear resistance. If these powders are not commercially available, they could be prepared through intensive ball milling of the commercially available nanostructured WC-Co-Cr powder used within this study.

In-flight particle temperature and velocity measurements when spraying the same WC-Co-Cr powder with the ID-HVOF thermal spray torch at stand-off distances corresponding to the different sized cylinders in Chapter 5 would provide vital data regarding the state of the particles at the moment of impact with the substrate, confirming the arguments presented throughout this work. These measurements could be carried out alongside a spray parameter optimisation process, to help increase coating quality as far as possible. These in-flight measurements could also be carried out when spraying with the composite powder feedstock; however, it is unclear how successful this would be due to the likely difference in behaviour of the two in-flight materials affecting the outputted average particle measurements.

# References


[1] C. Lyphout, S. Bjorklund, Internal Diameter HVAF Spraying for Wear and Corrosion Applications, J. Therm. Spray Technol. 24 (2015) 235–243. https://doi.org/10.1007/s11666-014-0195-x.

[2] K. Jia, T.E. Fischer, Sliding wear of conventional and nanostructured cemented carbides, Wear. 203–204 (1997) 310–318. https://doi.org/10.1016/S0043-1648(96)07423-6.

[3] C.R. Gagg, P.R. Lewis, Wear as a product failure mechanism - Overview and case studies, Eng. Fail. Anal. 14 (2007) 1618–1640. https://doi.org/10.1016/j.engfailanal.2006.11.064.

[4] P. Menezes, S. Ingole, M. Nosonovsky, S. Kailas, M. Lovell, Tribology for scientists and engineers, Springer, 2013. https://doi.org/10.1007/978-1-4614-1945-7.

[5] I. Hutchings, P.. Shipway, Tribology: Friction and Wear of Engineering Materials, 2nd ed., Elsevier Science & Technology, 2017.

[6] J.F. Archard, Contact and rubbing of flat surfaces, J. Appl. Phys. 24 (1953) 981–988. https://doi.org/10.1063/1.1721448.

[7] W. Hirst, J.K. Lancaster, Surface film formation and metallic wear, J. Appl. Phys. 27 (1956) 1057–1065. https://doi.org/10.1063/1.1722541.

[8] T.. Eyre, The mechanisms of wear, Tribol. Int. 11 (1978) 91–96.

[9] C.M. Cotell, J.A. Sprague, Surface Engineering, Vol. 5, ASM International, 1994.

[10] F.. Hermanek, Thermal Spray Terminology and Company Origins, 2001.

[11] J.R. Davis, Handbook of Thermal Spray Technology, ASM International, 2004.

[12] S. Amin, H. Panchal, A Review on Thermal Spray Coating Processes, Int. J. Curr. Trends Eng. Res. 2 (2016) 556–563.

[13] P.L. Fauchais, J.V.R. Heberlein, M.I. Boulos, Thermal spray fundamentals: From powder to part, Springer US, 2014. https://doi.org/10.1007/978-0-387-68991-3.

[14] A.S.M. Ang, N. Sanpo, M.L. Sesso, S.Y. Kim, C.C. Berndt, Thermal spray maps: Material genomics of processing technologies, J. Therm. Spray Technol. 22 (2013) 1170–183. https://doi.org/10.1007/s11666-013-9970-3.

[15] P. Fauchais, Understanding plasma spraying, J. Phys. D. Appl. Phys. 37 (2004) 86–108. https://doi.org/10.1088/0022-3727/37/9/R02.

[16] A. Matthews, Advanced Surface Coatings A handbook of surface engineering, 1st ed., Springer Netherlands, 1991.

[17] J. a. Picas, E. Rupérez, M. Punset, A. Forn, Influence of HVOF spraying parameters on the corrosion resistance of WC-Co-Cr coatings in strong acidic environment, Surf. Coatings Technol. 225 (2013) 47–57. https://doi.org/10.1016/j.surfcoat.2013.03.015.

[18] T. Sudaprasert, P.H. Shipway, D.G. McCartney, Sliding wear behaviour of HVOF sprayed WC-Co coatings deposited with both gas-fuelled and liquid-fuelled systems, Wear. 255 (2003) 943–949. https://doi.org/10.1016/S0043-1648(03)00293-X.

[19] R. Schwetzke, H. Kreye, Microstructure and properties of tungsten carbide coatings sprayed with various high-velocity oxygen fuel spray systems, J. Therm. Spray Technol. 8 (1999) 433–439. https://doi.org/10.1361/105996399770350395.

[20] M. Li, P.D. Christofides, Modeling and Control of High-Velocity Oxygen-Fuel (HVOF) Thermal Spray: A Tutorial Review, J. Therm. Spray Technol. 18 (2009) 753–768. https://doi.org/10.1007/s11666-009-9309-2.

[21] P.D. Christofides, N. El-Farra, M. Li, P. Mhaskar, Model-based control of particulate processes, Chem. Eng. Sci. 63 (2008) 1156–1172. https://doi.org/10.1016/j.ces.2007.07.017.

[22] J.A. Picas, M. Punset, M.T. Baile, E. Martín, A. Forn, Effect of oxygen/fuel ratio on the in-flight particle parameters and properties of HVOF WC-Co-Cr coatings, Surf. Coatings Technol. 205 (2011) S364–S368. https://doi.org/10.1016/j.surfcoat.2011.03.129.

[23] T.C. Hanson, G.S. Settles, Particle temperature and velocity effects on the porosity and oxidation of an HVOF corrosion-control coating, J. Therm. Spray Technol. 12 (2003) 403–415. https://doi.org/10.1361/105996303770348276.

[24] C. Hackett, The Gas Dynamics of High-velocity-oxy-fuel Thermal Sprays, Pennsylvania State University, USA, 1996.

[25] C. Berndt, S. Sampath, Advances in thermal spray science and technology, in: Proc. 8th Natl. Therm. Spray Conf., 1995.

[26] K. Dobler, H. Kreye, R. Schwetzke, Oxidation of stainless steel in the high velocity oxy-fuel process, J. Therm. Spray Technol. 9 (2000) 407–413. https://doi.org/10.1361/105996300770349872.

[27] S. Deshpande, S. Sampath, H. Zhang, Mechanisms of oxidation and its role in microstructural evolution of metallic thermal spray coatings - Case study for Ni-Al, Surf. Coatings Technol. 200 (2006) 5395–5406. https://doi.org/10.1016/j.surfcoat.2005.07.072.

[28] N. Zeoli, S. Gu, S. Kamnis, Numerical simulation of in-flight particle

oxidation during thermal spraying, Comput. Chem. Eng. 32 (2008) 1661–1668. https://doi.org/10.1016/j.compchemeng.2007.08.008.

[29] M. Fukumoto, E. Nishioka, T. Matsubara, Flattening and solidification behavior of a metal droplet on a flat substrate surface held at various temperatures, Surf. Coatings Technol. 120–121 (1999) 131–137. https://doi.org/10.1016/S0257-8972(99)00349-7.

[30] V. V. Sobolev, J.M. Guilemany, Investigation of coating porosity formation during high velocity oxy-fuel (HVOF) spraying, Mater. Lett. 18 (1994) 304–308. https://doi.org/10.1016/0167-577X(94)90012-4.

[31] R. Ghafouri-Azar, J. Mostaghimi, S. Chandra, M. Charmchi, A stochastic model to simulate the formation of a thermal spray coating, J. Therm. Spray Technol. 12 (2003) 53–69. https://doi.org/10.1361/105996303770348500.

[32] W.C. Lih, S.H. Yang, C.Y. Su, S.C. Huang, I.C. Hsu, M.S. Leu, Effects of process parameters on molten particle speed and surface temperature and the properties of HVOF CrC/NiCr coatings, Surf. Coatings Technol. 133–134 (2000) 54–60. https://doi.org/10.1016/S0257-8972(00)00873-2.

[33] E. Lugscheider, C. Herbst, L. Zhao, Parameter studies on high-velocity oxy-fuel spraying of MCrAlY coatings, Surf. Coatings Technol. 108–109 (1998) 16–23. https://doi.org/10.1016/S0257-8972(98)00630-6.

[34] C.M. Hackett, G.S. Settles, Research on HVOF Gas Shrouding for Coating Oxidation Control, in: Proc. Eighth Natl. Therm. Spray Conf., Houston, USA, 1995: pp. 21–29.

[35] Š. Houdková, M. Kašparová, F. Zahálka, The influence of spraying angle on properties of HVOF sprayed hardmetal coatings, J. Therm. Spray Technol. 19 (2010) 893–901. https://doi.org/10.1007/s11666-010-9514-z.

[36] W. Tillmann, C. Schaak, L. Hagen, G. Mauer, G. Matthäus, Internal Diameter Coating Processes for Bond Coat (HVOF) and Thermal Barrier Coating (APS) Systems, J. Therm. Spray Technol. 28 (2019) 233–241. https://doi.org/10.1007/s11666-018-0781-4.

[37] V. Katranidis, S. Kamnis, B. Allcock, S. Gu, Effects and Interplays of Spray Angle and Stand-off Distance on the Sliding Wear Behavior of HVOF WC-17Co Coatings, J. Therm. Spray Technol. 28 (2019) 514–534. https://doi.org/10.1007/s11666-019-00831-x.

[38] E. Strock, P. Ruggiero, D. Reynolds, The Effect of Off-Angle Spraying on the Structure and Properties of HVOF WC/CoCr Coatings, in: Proc. Int. Therm. Spray Conf., ASM International, 2001: pp. 671–676.

[39] U. Selvadurai, P. Hollingsworth, I. Baumann, B. Hussong, W. Tillmann, S. Rausch, D. Biermann, Influence of the handling parameters on residual stresses of HVOF-sprayed WC-12Co coatings, Surf. Coatings Technol. 268 (2015) 30–35. https://doi.org/10.1016/j.surfcoat.2014.11.055.

[40] B. Allcock, S. Gu, S. Kamnis, Nozzle for a Thermal Spray Gun and Method of Thermal Spraying, EP2411554B1, 2013.

[41] J. Gutleber, R. Molz, J. He, C. Weber, J. Colmenares, New developments in HVOF spraying for internal diameter coatings, in: Proc. Int. Therm. Spray Conf., 2017: pp. 501–504.

[42] A. Burgess, Novel HVOF torch for spraying internal diameters, in: Proc. Int. Therm. Spray Conf., Dusseldorf, Germany, 2017: pp. 346–353.

[43] W. Tillmann, C. Schaak, L. Hagen, M. Dildrop, Investigation of HVOF-ID spraying with WC-Co-Cr-15+5 µm feedstock powder, in: IOP Conf. Ser. Mater. Sci. Eng., 2019. https://doi.org/10.1088/1757-899X/480/1/012008.

[44] C.J. Li, W.Y. Li, Effect of sprayed powder particle size on the oxidation behavior of MCrAlY materials during high velocity oxygen-fuel deposition, Surf. Coatings Technol. 162 (2003) 31–41. https://doi.org/10.1016/S0257-8972(02)00573-X.

[45] F.E. Marble, Dynamics of a gas containing small solid particles, in: 5th AGARDograph Colloq. Combust. Propuls., 1963: pp. 175–213.

[46] R.A. Neiser, M.F. Smith, R.C. Dykhuizen, Oxidation in Wire HVOF-Sprayed Steel, J. Therm. Spray Technol. 7 (1998) 537–545. https://doi.org/10.1361/105996398770350765.

[47] J. Kawakita, S. Kuroda, T. Fukushima, H. Katanoda, K. Matsuo, H. Fukanuma, Dense titanium coatings by modified HVOF spraying, Surf. Coatings Technol. 201 (2006) 1250–1255. https://doi.org/10.1016/j.surfcoat.2006.01.056.

[48] J.A. Picas, M. Punset, E. Rupérez, S. Menargues, E. Martin, M.T. Baile, Corrosion mechanism of HVOF thermal sprayed WC-Co-Cr coatings in acidic chloride media, Surf. Coatings Technol. 371 (2019) 378–388. https://doi.org/10.1016/j.surfcoat.2018.10.025.

[49] G. Bolelli, L.M. Berger, T. Börner, H. Koivuluoto, L. Lusvarghi, C. Lyphout, N. Markocsan, V. Matikainen, P. Nylén, P. Sassatelli, R. Trache, P. Vuoristo, Tribology of HVOF- and HVAF-sprayed WC-10Co4Cr hardmetal coatings: A comparative assessment, Surf. Coatings Technol. 265 (2015) 125–144. https://doi.org/10.1016/j.surfcoat.2015.01.048.

[50] V.A. de Souza, A. Neville, Corrosion and erosion damage

mechanisms during erosion - corrosion of WC-Co-Cr cermet coatings, Wear. 255 (2003) 146–156. https://doi.org/10.1016/S0043-1648(03)00210-2.

[51] L.M. Berger, P. Vuoristo, T. Mantyla, W. Kunert, W. Lengauer, P. Ettmayer, Microstructure and properties of WC-Co-Cr coatings, in: Proc. 9th Natl. Therm. Spray Conf., Cincinnati, USA, 1996: pp. 97–106.

[52] P.H. Shipway, D.G. McCartney, T. Sudaprasert, Sliding wear behaviour of conventional and nanostructured HVOF sprayed WC-Co coatings, Wear. 259 (2005) 820–827. https://doi.org/10.1016/j.wear.2005.02.059.

[53] T. Sudaprasert, An Investigation of Microstructure and Sliding Wear in Thermally Sprayed WC-Co Coatings., The University of Nottingham, 2002.

[54] M.E. Vinayo, F. Kassabji, J. Guyonnet, P. Fauchais, Plasma sprayed WC–Co coatings: Influence of spray conditions (atmospheric and low pressure plasma spraying) on the crystal structure, porosity, and hardness, J. Vac. Sci. Technol. A Vacuum, Surfaces, Film. 3 (1985) 2483–2489. https://doi.org/10.1116/1.572863.

[55] D.A. Stewart, P.H. Shipway, D.G. McCartney, Abrasive wear behaviour of conventional and nanocomposite HVOF-sprayed WC-Co coatings, Wear. 225–229 (1999) 789–798. https://doi.org/10.1016/S0043-1648(99)00032-0.

[56] C. Verdon, A. Karimi, J.L. Martin, A study of high velocity oxy-fuel thermally sprayed tungsten carbide based coatings. Part 1: Microstructures, Mater. Sci. Eng. A. 246 (1998) 11–24.

[57] B.H. Kear, G. Skandan, R.K. Sadangi, Factors controlling decarburization in HVOF sprayed nano-WC/Co hardcoatings, Scr. Mater. 44 (2001) 1703–1707. https://doi.org/10.1016/S1359-6462(01)00867-3.

[58] D. a. Stewart, P.H. Shipway, D.G. McCartney, Microstructural evolution in thermally sprayed WC-Co coatings: comparison between nanocomposite and conventional starting powders, Acta Mater. 48 (2000) 1593–1604. https://doi.org/10.1016/S1359-6454(99)00440-1.

[59] S.M. Nahvi, M. Jafari, Microstructural and mechanical properties of advanced HVOF-sprayed WC-based cermet coatings, Surf. Coatings Technol. 286 (2016) 95–102. https://doi.org/10.1016/j.surfcoat.2015.12.016.

[60] A.S. Kurlov, A.I. Gusev, Tungsten carbides and W-C phase diagram, Inorg. Mater. 42 (2006) 121–127. https://doi.org/10.1134/S0020168506020051.

[61] S. Hong, Y. Wu, B. Wang, Tribological behavior of cermet coatings deposited from submicron WC-10Co-4Cr powders using HVOF spraying, Mater. Sci. 25 (2019) 303–308. https://doi.org/10.5755/j01.ms.25.3.19507.

[62] L. Thakur, N. Arora, Sliding and abrasive wear behavior of WC-Co-Cr coatings with different carbide sizes, J. Mater. Eng. Perform. 22 (2013) 574–583. https://doi.org/10.1007/s11665-012-0265-5.

[63] J.K.N. Murthy, B. Venkataraman, Abrasive wear behaviour of WC-Co-Cr and Cr3C2 -20(NiCr) deposited by HVOF and detonation spray processes, Surf. Coatings Technol. 200 (2006) 2642–2652. https://doi.org/10.1016/j.surfcoat.2004.10.136.

[64] L.M. Berger, S. Saaro, T. Naumann, M. Wiener, V. Weihnacht, S. Thiele, J. Suchánek, Microstructure and properties of HVOF-sprayed chromium alloyed WC-Co and WC-Ni coatings, Surf. Coatings Technol. 202 (2008) 4417–4421. https://doi.org/10.1016/j.surfcoat.2008.04.019.

[65] P. Kulu, S. Zimakov, Wear resistance of thermal sprayed coatings on the base of recycled hardmetal, Surf. Coatings Technol. 130 (2000) 46–51. https://doi.org/10.1016/S0257-8972(00)00687-3.

[66] L. Zhao, M. Maurer, F. Fischer, E. Lugscheider, Study of HVOF spraying of WC-Co-Cr using on-line particle monitoring, Surf. Coatings Technol. 185 (2004) 160–165. https://doi.org/10.1016/j.surfcoat.2003.12.024.

[67] L. Jacobs, M.M. Hyland, M. De Bonte, Study of the influence of microstructural properties on the sliding-wear behavior of HVOF and HVAF sprayed WC-cermet coatings, J. Therm. Spray Technol. 8 (1999) 125–132. https://doi.org/10.1361/105996399770350656.

[68] G. Bolelli, L.M. Berger, T. Börner, H. Koivuluoto, L. Lusvarghi, C. Lyphout, N. Markocsan, V. Matikainen, P. Nylén, P. Sassatelli, R. Trache, P. Vuoristo, Tribology of HVOF- and HVAF-sprayed WC-10Co4Cr hardmetal coatings: A comparative assessment, Surf. Coatings Technol. 265 (2015) 125–144. https://doi.org/10.1016/j.surfcoat.2015.01.048.

[69] G. Bolelli, L.M. Berger, M. Bonetti, L. Lusvarghi, Comparative study of the dry sliding wear behaviour of HVOF-sprayed WC-(W,Cr)2C-Ni and WC-Co-Cr hardmetal coatings, Wear. 309 (2014) 96–111. https://doi.org/10.1016/j.wear.2013.11.001.

[70] L. Jacobs, M.M. Hyland, M. De Bonte, Comparative Study of WC-Cermet Coatings Sprayed via the HVOF and the HVAF Process, J. Therm. Spray Technol. 7 (1998) 213–218. https://doi.org/10.1361/105996398770350954.

[71] K. Farokhzadeh, R.M. Fillion, A. Edrisy, The Effect of Deposition Rate

on Microstructural Evolution in WC-Co-Cr Coatings Deposited by High-Velocity Oxy-Fuel Thermal Spray Process, J. Mater. Eng. Perform. 28 (2019). https://doi.org/10.1007/s11665-019-04502-4.

[72] J.M. Guilemany, J.M.. Sanchez, Influence of the Manufacture Process to obtain WC+Co Thermal Spraying Powders. Effects on the Powder Characteristics and Coating Properties, in: Proc. 1998 Powder Metall. World Congr. Exhib., Granada, Spain, 1998: pp. 63–68.

[73] C.. Fernandes, A.M.. Senos, Cemented carbide phase diagrams: A review, Int. J. Refract. Met. Hard Mater. 29 (2011) 405–418.

[74] G. Bolelli, V. Cannillo, L. Lusvarghi, S. Riccò, Mechanical and tribological properties of electrolytic hard chrome and HVOF-sprayed coatings, Surf. Coatings Technol. 200 (2006) 2995–3009. https://doi.org/10.1016/j.surfcoat.2005.04.057.

[75] A.S. Taha, F.H. Hammad, Application of the Hall-Petch Relation to Microhardness Measurements on Al, Cu, Al-MD 105, and Al-Cu Alloys, Phys. Status Solidi. 119 (1990) 455–462. https://doi.org/10.1002/pssa.2211190207.

[76] K. Jia, T.E. Fischer, Abrasion resistance of nanostructured and conventional cemented carbides, Wear. 200 (1996) 206–214. https://doi.org/10.1016/S0043-1648(96)07277-8.

[77] F.H. Chung, Quantitative interpretation of X-ray diffraction patterns of mixtures. II. Adiabatic principle of X-ray diffraction analysis of mixtures, J. Appl. Crystallogr. 7 (1974) 526–531. https://doi.org/10.1107/s0021889874010387.

[78] J.M. Guilemany, S. Dosta, J.R. Miguel, The enhancement of the properties of WC-Co HVOF coatings through the use of nanostructured and microstructured feedstock powders, Surf. Coatings Technol. 201 (2006) 1180–1190. https://doi.org/10.1016/j.surfcoat.2006.01.041.

[79] C. Verdon, A. Karimi, J.-L. Martin, Microstructural and analytical study of thermally sprayed WC-Co coatings in connection with their wear resistance, Mater. Sci. Eng. A. 234–236 (1997) 731–734. https://doi.org/10.1016/s0921-5093(97)00377-8.

[80] W. Tillmann, J. Nebel, W. Piotrowski, Influence of fine powder feedstock (-10 + 2 μm) on the HVOF spraying characteristics, coating morphology, and properties of WC-Co-Cr 86-10-4, J. Therm. Spray Technol. 22 (2013) 242–249. https://doi.org/10.1007/s11666-012-9832-4.

[81] Hutchings, I.M., Tribology : friction and wear of engineering materials, Edward Arnold, London, 1992.

[82] K.. Zum-Gahr, Microstructure and Wear of Materials, 1987.

[83] C.W. Lee, J.H. Han, J. Yoon, M.C. Shin, S.I. Kwun, A study on powder mixing for high fracture toughness and wear resistance of WC-Co-Cr coatings sprayed by HVOF, Surf. Coatings Technol. 204 (2010) 2223–2229. https://doi.org/10.1016/j.surfcoat.2009.12.014.

[84] E. López Cantera, B.G. Mellor, Fracture toughness and crack morphologies in eroded WC-Co-Cr thermally sprayed coatings, Mater. Lett. 37 (1998) 201–210. https://doi.org/10.1016/S0167-577X(98)00092-5.

[85] B.R. Lawn, E.R. Fuller, Equilibrium penny-like cracks in indentation fracture, J. Mater. Sci. 10 (1975) 2016–2024. https://doi.org/10.1007/BF00557479.

[86] A.G. Evans, T.R. Wilshaw, Quasi-static solid particle damage in brittle solids-I. Observations analysis and implications, Acta Metall. 24 (1976) 939–956. https://doi.org/10.1016/0001-6160(76)90042-0.

[87] A.C. Savarimuthu, H.F. Taber, I. Megat, J.R. Shadley, E.F. Rybicki, W.C. Cornell, W.A. Emery, D.A. Somerville, J.D. Nuse, Sliding wear behavior of tungsten carbide thermal spray coatings for replacement of chromium electroplate in aircraft applications, J. Therm. Spray Technol. 10 (2001) 502–510. https://doi.org/10.1361/105996301770349286.

[88] A.K. Das, Stereometric analysis and relation between the porosity of sprayed and sintered NiCrSiB plasma spray protective coating, J. Mater. Process. Technol. 101 (2000) 322–331. https://doi.org/10.1016/S0924-0136(99)00475-6.

[89] A.S. Praveen, J. Sarangan, S. Suresh, J. Siva Subramanian, Erosion wear behaviour of plasma sprayed NiCrSiB/Al2O3 composite coating, Int. J. Refract. Met. Hard Mater. 52 (2015) 209–218. https://doi.org/10.1016/j.ijrmhm.2015.06.005.

[90] P.R. Reinaldo, A.S.C.M. D'Oliveira, NiCrSiB coatings deposited by plasma transferred arc on different steel substrates, J. Mater. Eng. Perform. 22 (2013) 590–597. https://doi.org/10.1007/s11665-012-0271-7.

[91] A.S. Praveen, J. Sarangan, S. Suresh, B.H. Channabasappa, Optimization and erosion wear response of NiCrSiB/WC-Co HVOF coating using Taguchi method, Ceram. Int. 42 (2016) 1094–1104. https://doi.org/10.1016/j.ceramint.2015.09.036.

[92] L. Peng, Preparation and tribological properties of NiCrBSiC reinforced laser alloying layer, Tribol. Trans. 56 (2013) 697–702. https://doi.org/10.1080/10402004.2013.782619.

[93] M.R. Ramesh, S. Prakash, S.K. Nath, P.K. Sapra, B. Venkataraman, Solid particle erosion of HVOF sprayed WC-Co/NiCrFeSiB coatings,

Wear. 269 (2010) 197–205. https://doi.org/10.1016/j.wear.2010.03.019.

[94] K. Simunovic, L. Slokar, S. Havrlisan, SEM/EDS investigation of one-step flame sprayed and fused Ni-based self-fluxing alloy coatings on steel substrates, Philos. Mag. 97 (2017) 248–268. https://doi.org/10.1080/14786435.2016.1257167.

[95] K. Simunovic, T. Saric, G. Simunovic, Different Approaches to the Investigation and Testing of the Ni-Based Self-Fluxing Alloy Coatings—A Review. Part 1: General Facts, Wear and Corrosion Investigations, Tribol. Trans. 57 (2014) 955–979. https://doi.org/10.1080/10402004.2014.927547.

[96] P. Kulu, T. Pihl, Selection criteria for wear resistant powder coatings under extreme erosive wear conditions, J. Therm. Spray Technol. 11 (2002) 517–522. https://doi.org/10.1361/105996302770348646.

[97] I.. Conciatu, C.. Ciubotariu, E.. Secosan, D. Frunzaverde, C.. Campian, Microstructure and wear behaviour of self-fluxing alloy coatings reinforced by WC-Co, IOP Conf. Ser. Mater. Sci. Eng. 444 (2018).

[98] N. Serres, F. Hlawka, S. Costil, C. Langlade, F. MacHi, Microstructures and mechanical properties of metallic NiCrBSi and composite NiCrBSi-WC layers manufactured via hybrid plasma/laser process, Appl. Surf. Sci. 257 (2011) 5132–5137. https://doi.org/10.1016/j.apsusc.2010.11.062.

[99] M.. Richert, The wear resistance of thermal spray the tungsten and chromium carbides coatings, J. Achiev. Mater. Manufcacturing Eng. 47 (2011) 177–184.

[100] J.C. Miranda, A. Ramalho, Abrasion resistance of thermal sprayed composite coatings with a nickel alloy matrix and a WC hard phase. Effect of deposition technique and re-melting, Tribol. Lett. 11 (2001) 37–48. https://doi.org/10.1023/A:1016692304440.

[101] Z. Ma, H.G. Merkus, J.G.A.E. De Smet, C. Heffels, B. Scarlett, New developments in particle characterization by laser diffraction: Size and shape, Powder Technol. (2000). https://doi.org/10.1016/S0032-5910(00)00242-4.

[102] J.I. Goldstein, D.E. Newbury, P. Echlin, D.C. Joy, C.E. Lyman, E. Lifshin, L. Sawyer, J.R. Michael, J.I. Goldstein, D.E. Newbury, P. Echlin, D.C. Joy, C.E. Lyman, E. Lifshin, L. Sawyer, J.R. Michael, Electron Beam–Specimen Interactions, in: Scanning Electron Microsc. X-Ray Microanal., 2003. https://doi.org/10.1007/978-1-4615-0215-9_3.

[103] A. Ul-Hamid, A Beginners' Guide to Scanning Electron Microscopy, Springer, 2018.

[104] J. Schindelin, E.T. Arena, B.E. DeZonia, M.C. Hiner, K.W. Eliceiri, C.T. Rueden, A.E. Walter, ImageJ2: ImageJ for the next generation of scientific image data, BMC Bioinformatics. 18 (2017) 1–26. https://doi.org/10.1186/s12859-017-1934-z.

[105] Springer Handbook of Experimental Solid Mechanics, 2008. https://doi.org/10.1007/978-0-387-30877-7.

[106] T. Aleksandrov Fabijanić, D. Ćorić, M. Šnajdar Musa, M. Sakoman, Vickers indentation fracture toughness of near-nano and nanostructured WC-Co cemented carbides, Metals (Basel). 7 (2017). https://doi.org/10.3390/met7040143.

[107] D.K. Shetty, I.G. Wright, P.N. Mincer, A.H. Clauer, Indentation fracture of WC-Co cermets, J. Mater. Sci. 20 (1985) 1873–1882. https://doi.org/10.1007/BF00555296.

[108] W.C. Oliver, G.M. Pharr, An improved technique for determining hardness and elastic modulus using load and displacement sensing indentation experiments, J. Mater. Res. 7 (1992) 1564–1583.

[109] P.H. Shipway, The role of test conditions on the microabrasive wear behaviour of soda-lime glass, Wear. 233–235 (1999) 191–199. https://doi.org/10.1016/S0043-1648(99)00187-8.

[110] M.A. Hazle, M. Mehicic, D.J. Gardiner, P.R. Graves, Practic1. Hazle MA, Mehicic M, Gardiner DJ, Graves PR. Practical Raman Spectroscopy. Vib Spectrosc. 1990; al Raman Spectroscopy, Vib. Spectrosc. (1990). https://doi.org/10.1016/0924-2031(90)80015-v.

[111] X. Ding, X.D. Cheng, C. Li, X. Yu, Z.X. Ding, C.Q. Yuan, Microstructure and performance of multi-dimensional WC-Co-Cr coating sprayed by HVOF, Int. J. Adv. Manuf. Technol. 96 (2018) 1625–1633. https://doi.org/10.1007/s00170-017-0837-5.

[112] B. Kaplan, S. Norgren, M. Schwind, M. Selleby, Thermodynamic calculations and experimental verification in the WC-Co-Cr cemented carbide system, Int. J. Refract. Met. Hard Mater. 48 (2015) 257–262. https://doi.org/10.1016/j.ijrmhm.2014.09.016.

[113] E.S. Zakharova, I.Y. Markova, A.L. Maslov, N.I. Polushin, A.I. Laptev, Morphology of powders of tungsten carbide used in wear-resistant coatings and deposition on the PDC drill bits, in: J. Phys. Conf. Ser. 857, 2017. https://doi.org/10.1088/1742-6596/857/1/012058.

[114] S. Usmani, S. Sampath, D.L. Houck, D. Lee, Effect of carbide grain size on the sliding and abrasive wear behavior of thermally sprayed WC-Co coatings, Tribol. Trans. 40 (1997) 470–478. https://doi.org/10.1080/10402009708983682.

[115] V. Katranidis, S. Gu, B. Allcock, S. Kamnis, Experimental study of

high velocity oxy-fuel sprayed WC-17Co coatings applied on complex geometries. Part A: Influence of kinematic spray parameters on thickness, porosity, residual stresses and microhardness, Surf. Coatings Technol. 311 (2017) 206–215. https://doi.org/10.1016/j.surfcoat.2017.01.015.

[116] D.A. Stewart, P.H. Shipway, D.G. McCartney, Influence of heat treatment on the abrasive wear behaviour of HVOF sprayed WC-Co coatings, Surf. Coatings Technol. 105 (1998) 13–24. https://doi.org/10.1016/S0257-8972(98)00444-7.

[117] W. Tillmann, E. Vogli, I. Baumann, G. Matthaeus, T. Ostrowski, Influence of the HVOF gas composition on the thermal spraying of WC-Co submicron powders (-8 + 1μm) to produce superfine structured cermet coatings, in: J. Therm. Spray Technol., 2008. https://doi.org/10.1007/s11666-008-9234-9.

[118] G.H. Lee, S. Kang, Sintering of nano-sized WC-Co powders produced by a gas reduction-carburization process, J. Alloys Compd. 419 (2006) 281–289. https://doi.org/10.1016/j.jallcom.2005.09.060.

[119] T. Varis, T. Suhonen, A. Ghabchi, A. Valarezo, S. Sampath, X. Liu, S.P. Hannula, Formation mechanisms, structure, and properties of HVOF-sprayed WC-Co-Cr coatings: An approach toward process maps, J. Therm. Spray Technol. 23 (2014) 1009–1018. https://doi.org/10.1007/s11666-014-0110-5.

[120] M. Li, P.D. Christofides, Computational study of particle in-flight behavior in the HVOF thermal spray process, Chem. Eng. Sci. 61 (2006) 6540–6552. https://doi.org/10.1016/j.ces.2006.05.050.

[121] G. Bolelli, L. Lusvarghi, M. Barletta, HVOF-sprayed WC-Co-Cr coatings on Al alloy: Effect of the coating thickness on the tribological properties, Wear. 267 (2009) 944–953. https://doi.org/10.1016/j.wear.2008.12.066.

[122] S.J. Bull, Failure mode maps in the thin film scratch adhesion test, Tribol. Int. 30 (1997) 491–498. https://doi.org/10.1016/S0301-679X(97)00012-1.

[123] L. Gil, M.H. Staia, Microstructure and properties of HVOF thermal sprayed NiWCrBSi coatings, Surf. Coatings Technol. 120–121 (1999) 423–429. https://doi.org/10.1016/S0257-8972(99)00494-6.

[124] X. Xing, Y. Gui, G. Zhang, C. Song, CoWO4 nanoparticles prepared by two methods displaying different structures and supercapacitive performances, Electrochim. Acta. 157 (2015) 15–22. https://doi.org/10.1016/j.electacta.2015.01.055.

[125] S.H. Lee, H.M. Cheong, N.G. Park, C.E. Tracy, A. Mascarenhas, D.K. Benson, S.K. Deb, Raman spectroscopic studies of Ni-W oxide thin

films, Solid State Ionics. 140 (2001) 135–139. https://doi.org/10.1016/S0167-2738(01)00707-X.

[126] T.E. Fischer, Z. Zhu, H. Kim, D.S. Shin, Genesis and role of wear debris in sliding wear of ceramics, Wear. 245 (2000) 53–60. https://doi.org/10.1016/S0043-1648(00)00465-8.

[127] T.C. Hanson, C.M. Hackett, G.S. Settles, Independent control of HVOF particle velocity and temperature, J. Therm. Spray Technol. 11 (2002) 75–85. https://doi.org/10.1361/105996302770349005.

[128] M. Li, P.D. Christofides, Multi-scale modeling and analysis of an industrial HVOF thermal spray process, Chem. Eng. Sci. 60 (2005) 3649–3669. https://doi.org/10.1016/j.ces.2005.02.043.

[129] B. Sun, H. Fukanuma, N. Ohno, Study on stainless steel 316L coatings sprayed by a novel high pressure HVOF, Surf. Coatings Technol. 239 (2014) 58–64. https://doi.org/10.1016/j.surfcoat.2013.11.018.

[130] K. Murugan, A. Ragupathy, V. Balasubramanian, K. Sridhar, Optimizing HVOF spray process parameters to attain minimum porosity and maximum hardness in WC-10Co-4Cr coatings, Surf. Coatings Technol. 247 (2014) 90–102. https://doi.org/10.1016/j.surfcoat.2014.03.022.

[131] T. Sahraoui, N.E. Fenineche, G. Montavon, C. Coddet, Structure and wear behaviour of HVOF sprayed Cr3C2-NiCr and WC-Co coatings, Mater. Des. 24 (2003) 309–313. https://doi.org/10.1016/S0261-3069(03)00059-1.

[132] S.H. Chang, S.L. Chen, Characterization and properties of sintered WC-Co and WC-Ni-Fe hard metal alloys, J. Alloys Compd. 585 (2014) 407–413. https://doi.org/10.1016/j.jallcom.2013.09.188.

[133] N. Claussen, Fracture Toughness of Al2O3 with an Unstabilized ZrO2Dispersed Phase, J. Am. Ceram. Soc. 59 (1976) 49–51. https://doi.org/10.1111/j.1151-2916.1976.tb09386.x.

[134] N. Axén, S. Jacobson, S. Hogmark, Influence of hardness of the counterbody in three-body abrasive wear - an overlooked hardness effect, Tribol. Int. 27 (1994) 233–241. https://doi.org/10.1016/0301-679X(94)90003-5.

[135] A. Erdemir, A crystal-chemical approach to lubrication by solid oxides, Tribol. Lett. 8 (2000) 97–102. https://doi.org/10.1023/A:1019183101329.

[136] J.M. Guilemany, J.M. Miguel, S. Vizcaino, F. Climent, Role of three-body abrasion wear in the sliding wear behaviour of WC-Co coatings obtained by thermal spraying, Surf. Coatings Technol. 140 (2001) 141–146. https://doi.org/10.1016/S0257-8972(01)01033-7.

[137] Z. Geng, S. Li, D.L. Duan, Y. Liu, Wear behaviour of WC-Co HVOF coatings at different temperatures in air and argon, Wear. 330–331 (2015) 348–353. https://doi.org/10.1016/j.wear.2015.01.035.

[138] J.M. Perry, A. Neville, V.A. Wilson, T. Hodgkiess, Assessment of the corrosion rates and mechanisms of a WC-Co-Cr HVOF coating in static and liquid-solid impingement saline environments, Surf. Coatings Technol. (2001). https://doi.org/10.1016/S0257-8972(00)01062-8.

[139] K. Liu, X.P. Li, M. Rahman, X.D. Liu, CBM tool wear in ductile cutting of tungsten carbide, Wear. 255 (2003) 1344–1351.

[140] R.E. Smallman, A.H.W. Ngan, Modern Physical Metallurgy: Eighth Edition, 2013. https://doi.org/10.1016/C2011-0-05565-5.

# Appendix A – In-flight particle measurements of WC-Co-Cr using a liquid fuelled HVOF thermal spray system

To assess the relationship between the spray parameters and in-flight particle conditions and the coating microhardness and to validate the conclusions developed throughout this thesis, a WC-Co-Cr powder feedstock (AMPERIT® 558.074, H.C. Starck, Germany) was sprayed using a MetJet II HVOLF thermal spray torch using three separate sets of spray parameters, displayed below in Table 0-1. A stand-off distance of 200mm was used for all spray runs.

| **Parameter** | **MJ-1** | **MJ-2** | **MJ-3** |
|---|---|---|---|
| Oxygen (L/min) | 835 | 890 | 870 |
| Kerosene (mL/min) | 435 | 418 | 460 |

**Table 0-1 - Spray parameters used for in-flight particle measurements**

The Accuraspray G4 (Tecnar, Canada) was used to measure the in-flight particles, the relationship between in-flight particle temperature, velocity and coating microhardness measured from in-flight particle measurements is displayed below in Figure 0-1.

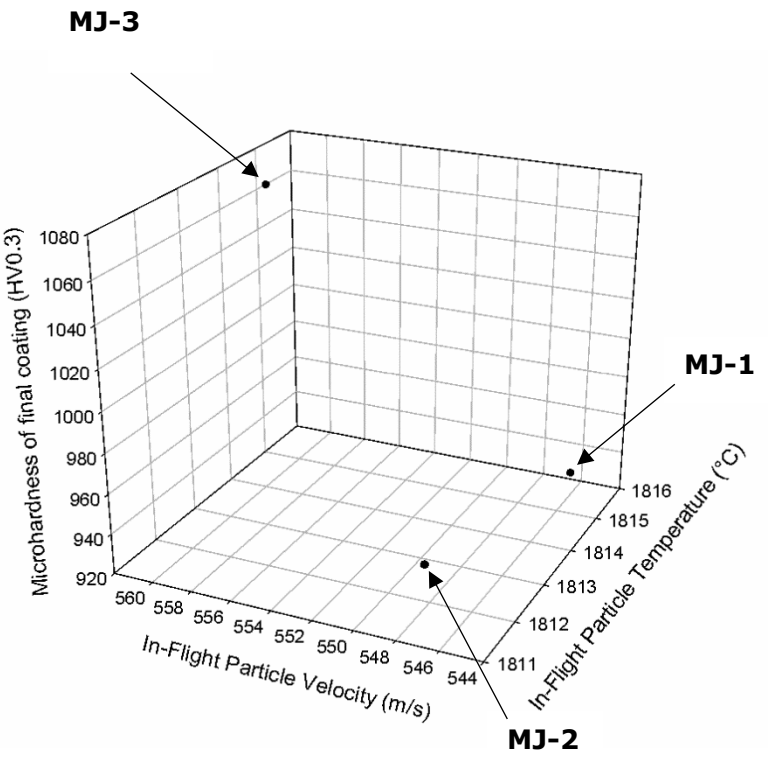


**Figure 0-1 - Relationship between coating hardness and in-flight temperature and velocity measurements when spraying a WC-CoCr powder**

From the data presented it can be observed that the temperature difference between the inflight particles when spraying using this spray parameters above is minimal, with the average temperature from all three runs being measured between 1811 – 1816°C. The in-flight particle velocity was seen to differ more significantly however, with the MJ-3 parameters giving rise to a much higher particle velocity than the other two parameter sets, with a measured in-flight particle velocity of just over 560m/s, in comparison to the other two parameter sets at 545m/s and 547m/s for the MJ-1 and MJ-2 parameter sets respectively. The MJ-3 parameter set produced a coating that also had a significantly higher hardness than the other two parameter sets with a hardness of 1069 HV0.3, while the MJ-1 and MJ-2 coatings had a similar microhardness of 938 and 948.

This data shows the clear link between in-flight particle velocity and coating microhardness, with the higher in-flight particle velocity of the MJ-3 parameters producing a coating that also has a higher microhardness. It was discussed in Chapter 4 that particle temperature may also play a role in the microhardness of WC-Co-Cr coatings, because of decarburisation. Excessive overheating of WC-Co-Cr particles in flight may lead to the dissolution of WC grains into a liquid or semi molten binder leading to the formation of other phases such as $W_2C$, which have a higher hardness but lower fracture toughness than WC. As a result, high particle temperatures in flight may possibly lead to increased coating hardness. However, the results presented in reveal that the particle temperature was very similar for each spray parameter set, meaning the coatings likely have a very similar phase composition. Taking the particle velocity into account, it could be argued that the hardest coating in this case may have undergone less decarburisation than the other two coatings, as the higher in-flight velocity would result in a shorter residence time in the flame. Therefore, it is most likely that the difference in coating hardness exhibited from the coatings above is a result of the increase in the in-flight particle velocity.

The MJ-3 parameter set that produced the coatings with the highest microhardness also required the greatest overall input into the torch, with higher oxygen and kerosene flowrates. This outcome mirrors the results gathered from the work carried out in Chapter 6, as the NiSF_HF coating sprayed using a greater amount of input gases than its counterpart also had the highest hardness. It was determined there was little difference in

the phase composition of the composite coatings sprayed by each parameter set, meaning this could not explain the difference in microhardness. The data above likely proves that the improved hardness and consequently better sliding wear resistance in the of the NiSF_HF coating was due to higher in-flight particle velocities provided by the higher gas input into the torch.

Increasing the input of oxidising and diluting gases and fuel into the torch may lead to an increase in the combustion chamber pressure, due to a greater mass of material entering the fixed combustion chamber volume per unit time [20]. Combustion chamber pressure has been shown to be directly linked to in-flight particle velocity in other work [23,129] and can be increased by raising the fuel flowrate into the torch [130]. Higher combustion chamber pressures will lead to greater in-flight particle velocities due to the larger pressure drop between occurring when the gas leaves the combustion chamber, resulting in increased gas acceleration.